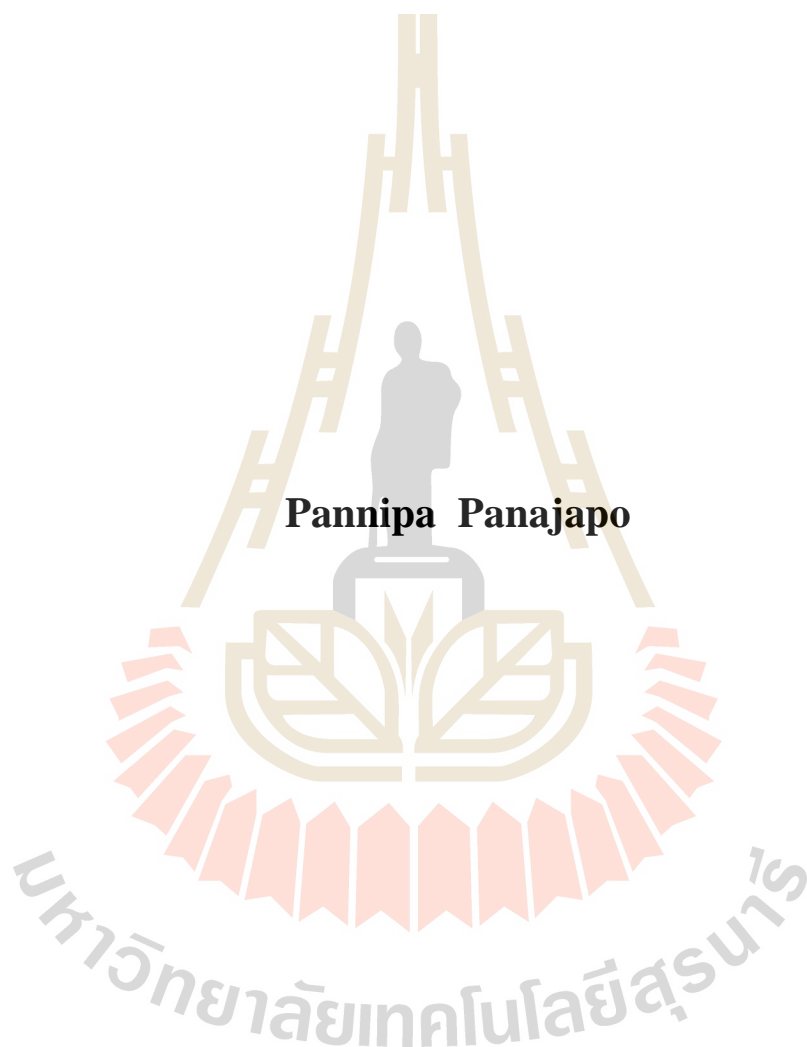


**MECHANISMS OF THE PHOTODISSOCIATIONS
OF METHANOL IN THE GAS PHASE**



**A Thesis Submitted in Partial Fulfillment of the Requirements for the
Degree of Doctor of Philosophy in Chemistry
Suranaree University of Technology
Academic Year 2019**

กลไกของการแตกตัวด้วยแสงของเมทานอลในสถานะแก๊ส



วิทยานิพนธ์นี้เป็นส่วนหนึ่งของการศึกษาตามหลักสูตรปริญญาวิทยาศาสตรดุษฎีบัณฑิต

สาขาวิชาเคมี


มหาวิทยาลัยเทคโนโลยีสุรนารี

ปีการศึกษา 2562


**MECHANISMS OF THE PHOTODISSOCIATIONS OF
METHANOL IN THE GAS PHASE**

Suranaree University of Technology has approved this thesis submitted in partial fulfillment of the requirements for the Degree of Doctor of Philosophy.


Thesis Examining Committee


(Prof. Dr. James R. Ketudat-Cairns)


Chairperson


(Prof. Dr. Kritsana Sagarik)


Member (Thesis Advisor)


(Assoc. Prof. Dr. Viwat Vchirawongkwin)

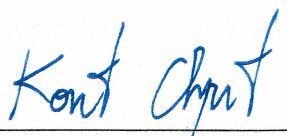
Member

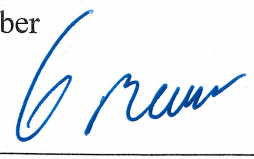

(Assoc. Prof. Dr. Anan Tongraar)

Member


(Dr. Suwit Suthirakun)

Member


(Assoc. Prof. Ft. Lt. Dr. Kontorn Chamniprasart)


(Assoc. Prof. Dr. Worawat Meevasana)

Vice Rector for Academic Affairs
and Internationalization

Dean of Institute of Science

พรรณา พะนะจะโปะ : กลไกของการแตกตัวด้วยแสงของเมทานอลในสถานะแก๊ส
(MECHANISMS OF THE PHOTODISSOCIATIONS OF METHANOL IN
THE GAS PHASE) อาจารย์ที่ปรึกษา : ศาสตราจารย์ ดร.กฤษณะ ศาคกริก, 109 หน้า

วิทยานิพนธ์เรื่องนี้ศึกษากลไกของการแตกตัวด้วยแสงของเมทานอลในสถานะแก๊ส ในสถานะถูกกระตุ้นซึ่งเกิดต่ำสุดอย่างเป็นระบบ โดยใช้ทฤษฎีการรบกวนอันดับสองปริภูมิกับมันต์บริบูรณ์ (complete active-space second-order perturbation theory, CASPT2) และ เซตมูลฐาน aug-cc-pVDZ โดยการศึกษาเชิงทฤษฎีนี้ เน้นกระบวนการการผ่อนคลายโครงสร้างชนิดไม่แผ่รังสี (nonradiative relaxation process) ที่ทำให้โมเลกุลที่ถูกกระตุ้นแนวตั้ง (vertically excited molecule) ในสถานะถูกกระตุ้นซึ่งเกิดต่ำสุด ($S_0 \rightarrow S_1$) เกิดเป็นสารผลิตภัณฑ์ในสถานะพื้นอิเล็กตรอนิกส์ เส้นโค้งพลังงานศักย์ผ่อนคลาย (relax-scan potential energy curve) ยืนยันว่าการแตกตัวของ O-H เป็นกระบวนการคายความร้อนที่โดดเด่นที่สุด และการเกิดฟอร์มัลดีไฮด์ (CH_2O) เป็นกระบวนการที่สำคัญรองลงมา ซึ่งเมื่อ O-H แตกตัวจะเกิดเป็นสารตั้งต้นสำหรับปฏิกิริยาอื่น ๆ ในสถานะพื้นได้อีกด้วย สำหรับการแตกตัวของ C-O เส้นโค้งพลังงานศักย์ผ่อนคลายแสดงว่า สารตั้งต้นต้องถูกกระตุ้นด้วยความร้อนในสถานะพื้นก่อน จากนั้นเกิดการกระตุ้นแนวตั้งด้วยแสงนำไปสู่โครงสร้างทรานซิชันในสถานะถูกกระตุ้นซึ่งเกิดต่ำสุด และการผ่อนคลายโครงสร้างชนิดไม่แผ่รังสี ทำให้เกิดเป็นเมทิลเรดิคัล ($[\text{CH}_3]^\cdot$) และ ไฮดรอกไซด์เรดิคัล ($[\text{OH}]^\cdot$) ในสถานะพื้นอิเล็กตรอนิกส์ในที่สุด ผลลัพธ์ที่ได้จากการคำนวณ CASPT2 แสดงความเป็นไปได้ในการแตกตัวไอโซเมอร์ไรเซชัน $[\text{CH}_3\text{OH}] \rightarrow [\text{CH}_2\text{OH}_2]$ (isomerization dissociation) ซึ่งเกิดจากสารตั้งต้นถูกกระตุ้นด้วยความร้อนก่อน ตามด้วยการกระตุ้นแนวตั้งด้วยแสง และการแตกตัวของ C-O เกิดพร้อมกับการถ่ายโอนโปรตอนระหว่างโมเลกุล เกิดเป็นสารเชิงซ้อนพันธะไฮโดรเจนในสถานะพื้นอิเล็กตรอนิกส์ซึ่งเกิดและทรูปเลต $[\text{CH}_2]^\cdot - [\text{H}_2\text{O}]$ ผลการวิเคราะห์สัมประสิทธิ์อันตรกิริยาสัมพันธ์ (correlation interaction (CI) coefficient) แสดงว่าการแตกตัวของ C-H เกิดเป็น $[\text{CH}_2\text{OH}]^\cdot$ และ $[\text{H}]^\cdot$ ไม่ควรเป็นกระบวนการหนึ่งโมเลกุล (unimolecular process) เนื่องจากไม่มีการผกผัน (inversion) และการตัดกัน (intersection) ของโครงแบบอิเล็กตรอนในสถานะพื้นและสถานะถูกกระตุ้นซึ่งเกิดต่ำสุด การศึกษาเชิงทฤษฎีสรุปว่า การแตกตัวของ O-H และการเกิดฟอร์มัลดีไฮด์และโมเลกุลไฮโดรเจน เป็นกระบวนการควบคุมเชิงจลนพลศาสตร์ (kinetically controlled process) ในขณะที่การแตกตัวของ C-O และการแตกตัวไอโซเมอร์ $[\text{CH}_3\text{OH}] \rightarrow [\text{CH}_2\text{OH}_2]$ เป็นกระบวนการควบคุมเชิงอุณหพลศาสตร์ (thermodynamically controlled process) โดยโฟตอนที่มีพลังงานเดียวกันโดยประมาณสามารถทำให้เกิดโมเลกุลทุกชนิดที่เป็นผลิตภัณฑ์ในสถานะพื้นอิเล็กตรอนิกส์ได้ ผลการค้นพบนี้

นำไปสู่ความเข้าใจอย่างลึกซึ้งถึงกระบวนการการคัดเลือกด้วยความร้อน (thermal selectivity) และบทบาทของลักษณะหลายโครงแบบ (multiconfigurational character) ในการแตกพันธะโคเวเลนต์ ซึ่งสามารถใช้เป็นแนวทางสำหรับการศึกษาทางทฤษฎีและทางการทดลองต่อไปในอนาคตได้



สาขาวิชาเคมี
ปีการศึกษา 2562

ลายมือชื่อนักศึกษา พรพนิต มนงจิระ
ลายมือชื่ออาจารย์ที่ปรึกษา Dr. Ph.D.

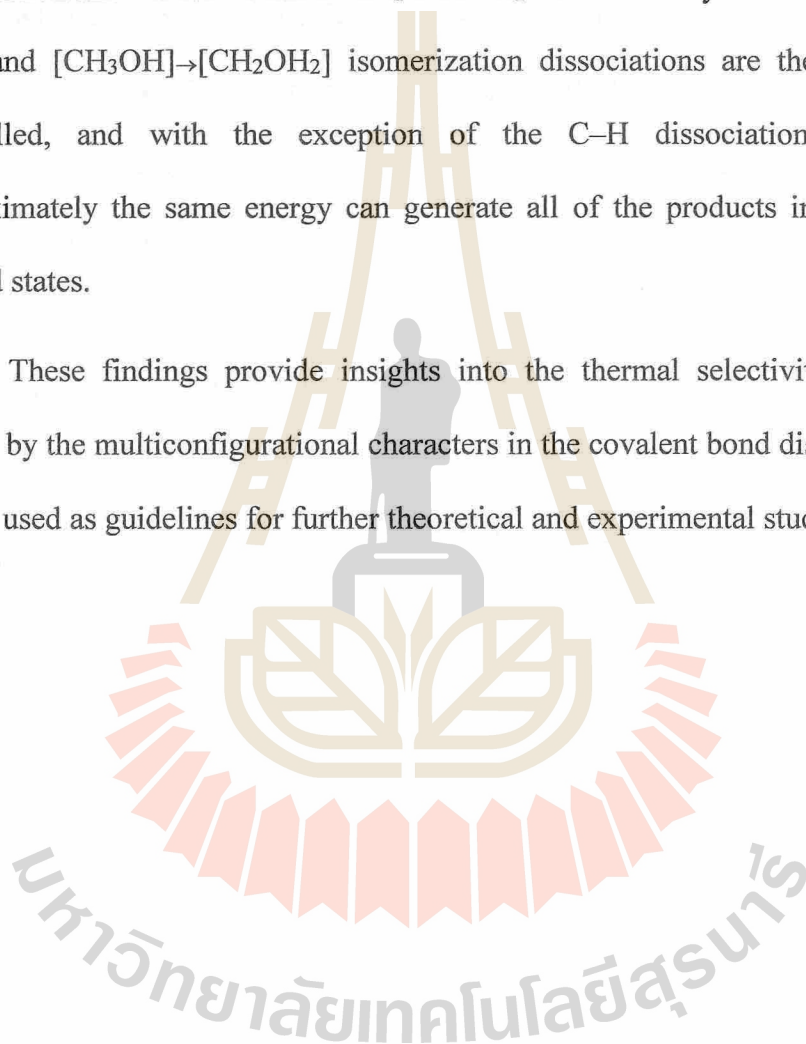
PANNIPA PANAJAPO : MECHANISMS OF THE
PHOTODISSOCIATIONS OF METHANOL IN THE GAS PHASE.
THESIS ADVISOR : PROF. KRITSANA SAGARIK, Ph.D. 109 PP.

SINGLE-ISOLATED METHANOL/ CASPT2/ PHOTODISSOCIATION
MECHANISMS/ LOWEST SINGLE-EXCITED STATE/ POTENTIAL ENERGY
SURFACES

The mechanisms of the photodissociations of single-isolated methanol (CH_3OH) in the lowest singlet-excited (S_1) state were systematically studied using the complete active-space second-order perturbation (CASPT2) theory with the aug-cc-pVDZ basis set. This theoretical study focused on nonradiative relaxation processes that bring the $S_0 \rightarrow S_1$ vertically excited molecule to the products in their respective electronic ground states. The relax-scan potential energy curves confirmed that the O–H dissociation is the predominant exothermic process and that the formation of formaldehyde (CH_2O) is the second preferential process, in which the O–H dissociated species are the precursors for the reaction in the S_0 state. For the C–O dissociation, the relax-scan potential energy curves suggested a thermally excited precursor in the S_0 state, from which the vertical excitation leads to a transition structure in the S_1 state, as well as the $[\text{CH}_3]^\cdot$ and $[\text{OH}]^\cdot$ products in their electronic ground states. The CASPT2 results also revealed a possibility for the $[\text{CH}_3\text{OH}] \rightarrow [\text{CH}_2\text{OH}_2]$ isomerization dissociation, in which another thermally excited precursor is vertically excited and the C–O dissociation and intermolecular proton transfer lead to the singlet and triplet $[\text{CH}_2] \cdots [\text{H}_2\text{O}]$ H-bond complexes in their showed

that the C–H dissociation, which generates $[\text{CH}_2\text{OH}]^*$ and $[\text{H}]^*$, is unlikely to be electronic ground states. Analysis of the correlation interaction (CI) coefficients unimolecular because of the lack of the electronic configuration inversion and intersection of the S_0 and S_1 states. The theoretical study concluded that the O–H dissociation and the formation of CH_2O and H_2 are kinetically controlled, whereas the C–O and $[\text{CH}_3\text{OH}] \rightarrow [\text{CH}_2\text{OH}_2]$ isomerization dissociations are thermodynamically controlled, and with the exception of the C–H dissociation, photons with approximately the same energy can generate all of the products in their electronic ground states.

These findings provide insights into the thermal selectivity and the roles played by the multiconfigurational characters in the covalent bond dissociation, which can be used as guidelines for further theoretical and experimental studies.



School of Chemistry

Academic Year 2019

Student's Signature

Darnipa

Advisor's Signature

H. Suan

ACKNOWLEDGMENTS

I would like to thank my thesis advisor, Prof. Dr. Kritsana Sagarik for his exceptional supervision, academic guidance, advice and encouragement in the course of my graduate. I would like to thank Prof. Dr. James R. Ketudat-Cairns, Assoc. Prof. Dr. Viwat Vchirawongkwin, Assoc. Prof. Dr. Anan Tongraar and Dr. Suwit Suthirakun, who are members of the thesis committee, for their time and useful suggestions. I would like to express my great gratitude to all lecturers at the School of Chemistry, Suranaree University of Technology (SUT) and the Department of Natural Product Chemistry, Faculty of Science, University of Quebec at Chicoutimi in Canada and Prof. Dr. Kuang-Sen Sung at National Cheng Kung University in Taiwan for their good attitude and advices.

I also would like to acknowledge the financial support provided by the Royal Golden Jubilee (RGJ) Ph.D. Program of the Thailand Research Fund (TRF) (Grant No. PHD/0139/2554). The high-performance computer facilities provided by the following organizations are gratefully acknowledged: the School of Mathematics and School of Chemistry, SUT and the National e-Science project of the National Electronics and Computer Technology Centre (NECTEC).

Finally, I would also like to thank my parents, sisters and all cousins for their support and encouragement throughout the course of my study at SUT.

Pannipa Panajapo

CONTENTS

| | Page |
|---|-------------|
| ABSTRACT IN THAI..... | I |
| ABSTRACT IN ENGLISH | III |
| ACKNOWLEDGEMENTS | V |
| CONTENTS | VI |
| LIST OF TABLES..... | VIII |
| LIST OF FIGURES | IX |
| LIST OF ABBREVIATIONS..... | XI |
| CHAPTER | |
| I INTRODUCTION..... | 1 |
| II COMPUTATIONAL METHODS..... | 9 |
| 2.1 <i>Ab initio</i> calculations..... | 9 |
| 2.2 Equilibrium geometries and potential energy curves..... | 12 |
| III RESULTS AND DISCUSSION | 15 |
| 3.1 Equilibrium structures..... | 22 |
| 3.2 The O–H dissociation | 23 |
| 3.3 The C–O dissociation..... | 29 |
| 3.4 The C–H dissociation..... | 35 |
| 3.5 Isomerization-mediated C–O dissociation..... | 40 |
| 3.6 Rotational-mediated C–H dissociation | 50 |

CONTENTS (Continued)

| | Page |
|--|-------------|
| 3.7 The interplay between the thermal excitation and photoexcitation | 56 |
| IV CONCLUSION | 61 |
| REFERENCES | 63 |
| APPENDICES | |
| APPENDIX A LIST OF POSTER AND PRESENTATION..... | 72 |
| APPENDIX B PUBLICATION..... | 73 |
| APPENDIX C MANUSCRIPT..... | 74 |
| CURRICULUM VITAE | 109 |

LIST OF TABLES

| Table | Page |
|--|------|
| 2.1 The number of configuration state function (CSFs) considered (N e-internal) and those generated by the CASPT2 methods (N-1 and N-2 e-internals) used in the calculations of CH ₃ OH..... | 11 |
| 3.1 Characteristic structures, structure parameters and energetics of CH ₃ OH, observed on the potential energy curves obtained from CASPT2(4,7) calculations..... | 17 |
| 3.2 Characteristic structures of CH ₃ OH on the S ₀ and S ₁ potential energy curves for the O–H dissociation..... | 28 |
| 3.3 Characteristic structures of CH ₃ OH on the S ₀ and S ₁ potential energy curves for the C–O dissociation..... | 33 |
| 3.4 Characteristic structures of CH ₃ OH on the S ₀ and S ₁ potential energy curves for the C–H dissociation | 39 |
| 3.5 Characteristic structures of CH ₃ OH on the S ₀ and S ₁ potential energy curves for intramolecular [CH ₃ OH]→[CH ₂ OH ₂] isomerization..... | 48 |
| 3.6 Characteristic structures of CH ₃ OH on the S ₁ relax-scan potential energy curves for the elimination of H ₂ | 55 |

LIST OF FIGURES

| Figure | Page |
|---|------|
| 1.1 Proposed dissociation channels for CH ₃ OH in the gas phase. ΔH^0 = standard enthalpy of dissociation | 3 |
| 2.1 Equilibrium structure of CH ₃ OH in the S ₀ state obtained from CASPT2(4,7) geometry optimizations..... | 14 |
| 3.1 The relax-scan potential energy curves with respect to the O–H coordinate obtained from CASPT2 calculations..... | 24 |
| 3.2 The relax-scan potential energy curves with respect to the C–O coordinate obtained from CASPT2 calculations..... | 30 |
| 3.3 The relax-scan potential energy curves with respect to the C–H coordinate obtained from CASPT2 calculations..... | 36 |
| 3.4 The relax-scan potential energy curves for the [CH ₃ OH]→[CH ₂ OH ₂] isomerization obtained from CASPT2(4,7) calculations by transferring the H ₍₄₎ atom from the CH ₃ group to the OH group..... | 42 |
| 3.5 Equilibrium structures of the [CH ₂] ₂ –[H ₂ O] H-bond complexes in the S ₀ and T ₀ states, obtained from CASPT2(4,7) calculations..... | 44 |
| 3.6 The relax-scan potential energy curves for the C–O rotation obtained from CASPT2(4,7) calculations..... | 52 |

LIST OF FIGURES (Continued)

| Figure | Page |
|---|-------------|
| 3.7 The relax-scan potential energy curves for formaldehyde formation from the O-H dissociated structure (structure E1-[4] [§]) obtained from CASPT2(4,7) calculations. | 54 |
| 3.8 Mechanisms of the unimolecular photodissociations of CH ₃ OH obtained from the analysis of the S ₀ and S ₁ potential energy curves obtained from the CASPT2(4,7) method. | 58 |
| 3.9 Mechanisms of the unimolecular photodissociations of CH ₃ OH obtained from the analysis of the S ₀ and S ₁ potential energy curves obtained from the CASPT2(4,7) method. | 59 |
| 3.10 Mechanisms of the unimolecular photodissociations of CH ₃ OH obtained from the analysis of the S ₀ and S ₁ potential energy curves obtained from the CASPT2(4,7) method. | 60 |

LIST OF ABBREVIATIONS

| | | |
|--------------------|---|---------------------------------------|
| Å | = | Ångström |
| CH ₃ OH | = | Methanol |
| H-bond | = | Hydrogen-bond |
| G | = | Structure in the S ₀ state |
| E | = | Structure in the S ₁ state |
| ω | = | Dihedral angle |
| R _{C-O} | = | C–O distance |
| R _{C-H} | = | C–H distance |
| R _{O-H} | = | O–H distance |
| au | = | Atomic unit |
| cm ⁻¹ | = | Wavenumber |
| K | = | Kelvin |
| eV | = | Electron Volt |
| nm | = | Nanometer |
| LUMO | = | Lowest unoccupied molecular orbital |
| HOMO | = | Highest occupied molecular orbital |
| ∠ | = | Bond angle |

LIST OF ABBREVIATIONS (Continued)

| | | |
|-----------------------|---|---|
| kJ/mol | = | kilo joule per mole |
| H_2O | = | Water |
| SCF | = | Self-consistent field |
| REMPI | = | Resonance-enhanced multiphoton ionization |
| CASPT2 | = | Complete active-space second-order perturbation theory |
| aug-cc-pVDZ | = | Augmented correlation-consistant polarized valence double-zeta basis set |
| CH_2O | = | Formaldehyde |
| S_0 | = | Electronic ground state |
| S_1 | = | Lowest singlet electronic excited state |
| ΔH° | = | Standard enthalpy of dissociation |
| IRMPD | = | Infrared multiple photon dissociation |
| CASSCF | = | Complete active-space self-consistent field |
| MRD-CI | = | Multireference single- and double-excitation correlation interaction |
| AO | = | Atomic orbital |
| CH_4 | = | Methane |

LIST OF ABBREVIATIONS (Continued)

| | | |
|-------------------|---|---|
| $^1[\text{CH}_2]$ | = | Singlet methylene |
| $^3[\text{CH}_2]$ | = | Triplet methylene |
| CCSD(T)-F12 | = | Explicitly-correlated coupled-cluster singles and doubles with perturbative triples method |
| MRCI+Q | = | Multireference configuration interaction with the Davidson correction |
| B3LYP-D3 | = | Semi-empirical dispersion correction in conjunction with Becke three-parameter hybrid functional combined with Lee-Yang-Parr correlation function |
| CI | = | Correlation interaction |
| CSF | = | Configuration state function |
| QSD | = | Quadratic steepest decent |
| CI(SD) | = | Configuration interaction with all single and double Excitations |
| k | = | Dissociation channel |
| l | = | Structure in the dissociation channel |
| C_0 | = | CI coefficient of the electronic ground state wavefunction |

LIST OF ABBREVIATIONS (Continued)

| | | |
|-------------------------|---|--|
| Ψ_0 | = | Electronic ground state wavefunction |
| Ψ_a^r | = | Singly excited state wavefunction (S-type) |
| $\Psi_{a,b}^{r,s}$ | = | Doubly excited state wavefunction (D-type) |
| * | = | Vertical excited state |
| ‡ | = | Transition state |
| § | = | Intersection of the S_0 and S_1 potential energy curve |
| E^{Ex} | = | Excitation energy |
| E^{Rel} | = | Relative energy |
| E^{Tot} | = | Total energy |
| ΔE^\ddagger | = | Energy barrier |
| ΔE^{Rel} | = | Energy release |
| ΔE^\S | = | Energy of structure at the intersection of the S_0 and S_1 potential energy curves |
| ΔE^{ST} | = | Singlet-triplet energy gap |
| ΔE^{HB} | = | Hydrogen bond energy |

CHAPTER I

INTRODUCTION

1.1 General introduction

The photochemistry of molecules in the gas and condensed phases has been extensively studied in the past decades, with the best topic being the photodissociation of small molecules in the Earth's atmosphere, which leads to serious environmental problems (Seinfeld and Pandis, 2016); solar radiation induces photochemical reactions through the formations of the reactive molecules; radicals, anions and cations. To study photodissociation reactions, modern spectroscopic techniques, such as fluorescence, resonance-enhanced multiphoton ionization (REMPI) and time-resolved vibrational spectroscopy, in combination with quantum chemical methods, such as TD-DFT, CASPT2, have proven to be powerful tools (Gonzalez, Escudero and Serrano-Andres, 2012) to describe the chemical structures and electronic properties of molecules in the ground state and, especially in the excited state.

The photodissociation of methanol (CH_3OH) has received special interest because the product radicals, e.g., the methoxy ($[\text{CH}_3\text{O}]^{\bullet}$), hydroxymethyl ($[\text{CH}_2\text{OH}]^{\bullet}$), methyl ($[\text{CH}_3]^{\bullet}$) and hydroxyl ($[\text{OH}]^{\bullet}$) radicals, are reactive intermediate in atmospheric, combustion and industrial processes (Seinfeld and Pandis, 2016; Gilbert, 2002); for example, in the Earth's atmosphere, $[\text{CH}_3\text{O}]^{\bullet}$ or $[\text{CH}_2\text{OH}]^{\bullet}$

can be generated through the oxidation of methane (CH_4) (Ravishankara, 1988). The experimental study of the reaction of $\text{O}(^1\text{D})$ with methane using a crossed molecular beam showed the formation of $[\text{CH}_3\text{O}]^\cdot$ or $[\text{CH}_2\text{OH}]^\cdot$ radicals by H elimination (Casavecchia, Buss, Sibener and Lee, 1980). The photolysis of CH_3OH in the gas phase has been extensively studied using various theoretical and experimental techniques (Sonntag and Schuchmann, 1977), among which the dissociation paths, radical intermediates and products, electronic states and associated absorption spectra have been of general interest. Theoretically, at least five unimolecular dissociation channels exist for CH_3OH in the gas phase (Saebo, Radom and Schaefer, 1983; Satyapal, Park, Bersohn and Katz, 1989). They are illustrated with their standard enthalpies of dissociation (ΔH°) in Figure 1.1 Channels (1), (2) and (3) occur through the homolytic cleavage of covalent bonds (O–H, C–H and C–O dissociations, respectively) and generate radical pair products, whereas molecules in their electronic ground states are the products of channels (4) and (5) (Satyapal, Park, Bersohn and Katz, 1989).

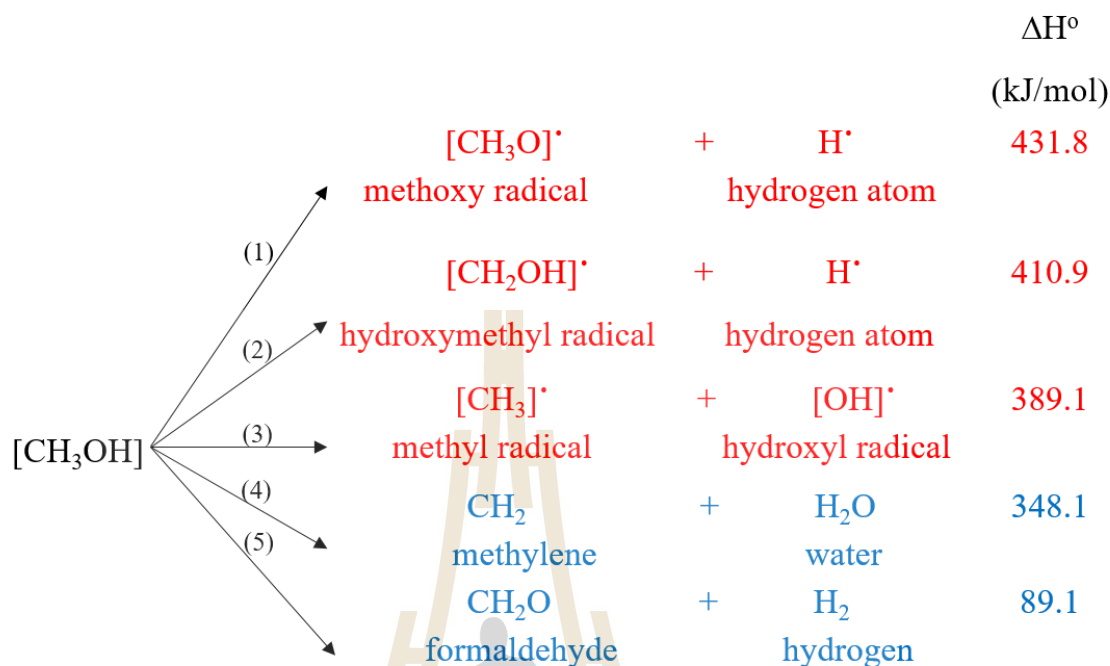


Figure 1.1 Proposed dissociation channels for CH₃OH in the gas phase (Saebo, Radom and Schaefer, 1983; Satyapal, Park, Bersohn and Katz, 1989). ΔH° = standard dissociation enthalpy.

The photofragmentation of CH₃OH in the lowest singlet-excited state (S₁) has received special attention due to the experimental observations; for example, a photoexcitation of CH₃OH at 193 nm method and the chemical activation method, involving the insertion of an O(¹D) atom into C-H bond of methane, showed the same results that the major channel of CH₃OH dissociation is to methoxy radical and hydrogen atom (channel (1)). Furthermore, the branching ratio of channel (1) is significantly higher than that of channel (3) (Satyapal, Park, Bersohn and Katz, 1989), although the standard enthalpy of dissociation of the former is higher than that of the

latter ($\Delta H^\circ = 432$ and 389 kJ/mol, respectively). For an alcohol in the electronic ground state, the average bond dissociation energy of C–O bond is generally weaker than the O–H bond (~ 109 kJ/mol) (Buenker, Olbrich, Schuchmann, Schuermann and Sonntag, 1984). In contrast, an infrared multiple photon dissociation (IRMPD) experiment of CH_3OH by CO_2 -laser light in a molecular beam configuration under collision-free condition (Schmiedl, Meier and Welge, 1981) and under collisional conditions in the bulk experiment (Bialkowski and Guillory, 1978). revealed that the dominant products of CH_3OH dissociation are the same as those found from thermal excitation (Sonntag and Schuchmann, 1977) regardless of the excitation energy, namely, $[\text{CH}_3]^\bullet$ and $[\text{OH}]^\bullet$ in channel (3). To study the branching ratio of channels (1) and (3), two-dimensional (2D) potential energy surfaces in the S_0 and S_1 states were constructed using the complete active-space self-consistent field (CASSCF) method (Marston, Weide, Schinke and Suter, 1993). This theoretical investigation emphasized on the influence of the initial vibrational excitation in the electronic ground state on the fragmentation process of methanol (CH_3OH) and the results showed that the dissociation in the vibrational ground state generates $[\text{CH}_3\text{O}]^\bullet$ and $[\text{H}]^\bullet$ exclusively (channel (1)), whereas exciting the CH_3O mode prior to $S_0 \rightarrow S_1$ excitation increases the quantum yield for hydroxyl radical ($[\text{OH}]^\bullet$), in which at least five or six quanta are required to obtain a reasonably large yield.

The photodissociation of CH_3OH through channel (3) was experimentally studied at 157 nm using the velocity map imaging technique with the detection of methyl radical ($[\text{CH}_3]^\bullet$) by resonance-enhanced multiphoton ionization (REMPI) (Chen, Eppink, Jiang, Groenenboom, Yang and Parker, 2011). The experimental

results suggested a two-step dissociation process, in which the generation of $[\text{CH}_3\text{O}]^{\bullet}$ *via* O–H bond cleavage in CH_3OH is the primary process and the photodissociation of the nascent $[\text{CH}_3\text{O}]^{\bullet}$ by the probe laser into $[\text{CH}_3]^{\bullet}$ is the secondary process. The proposed dissociation steps were supported by the potential energy surfaces in the S_0 and S_1 states obtained from *ab initio* multireference single- and double-excitation correlation interaction (MRD-CI) calculations with a freeze-scan method and a photolysis experiment of CH_3OH at 185 nm (Buenker, Olbrich, Schuchmann, Schuermann and Sonntag, 1984), which suggested that the homolytic cleavage of the O–H bond is found to be a dominant process for photolysis of saturated alcohols as proposed by Kassab, Gleghorn and Evleth (Kassab, Gleghorn and Evleth, 1983) which occurs along a purely repulsive potential energy curve and is associated with the conversion of the 3s Rydberg orbital into a 1s atomic orbital (AO) of the dissociating hydrogen atom.

In contrast, the C–O bond cleavage occurs along a low energy barrier pathway, which results from “a sharply avoided crossing between the respective Rydberg and valence electronic configurations” (Buenker, Olbrich, Schuchmann, Schuermann and Sonntag, 1984). The freeze-scan potential energy surfaces (Buenker, Olbrich, Schuchmann, Schuermann and Sonntag, 1984) also suggested that the C–H dissociation in channel (2), which leads to $[\text{CH}_2\text{OH}]^{\bullet}$ and $[\text{H}]^{\bullet}$, is not preferential in the S_1 state, whereas in the second preferential process, i.e., the formation of formaldehyde (CH_2O) in channel (5), the elimination of H_2 occurs on a low barrier surface. Since the S_0 and S_1 potential energy curves for the formation of CH_2O and H_2

do not intersect at separated distances ($R \geq 3 \text{ \AA}$), the authors attributed the generation of these two molecules to “surface-hopping effects” between the S_0 and S_1 states.

The photodissociation of CH_3OH vapor through channels (1)-(3) and (5) was studied at wavelengths below 200 nm using scavengers and deuterated methanol (CD_3OH) (Porter and Noyes, 1959). The experimental results showed that the main products of the photolysis were hydrogen (H_2), formaldehyde (CH_2O), and ethylene glycol ($\text{C}_2\text{H}_6\text{O}_2$) as well as small amounts of CO and CH_4 . In the presence of scavengers and CD_3OH , there are at least two primary processes; the formation of CH_2O and H_2 in channel (5) was concluded to be one of these primary processes. Additionally, CH_2O could also be formed by the thermal decomposition of $[\text{CH}_3\text{O}]^*$ or $[\text{CH}_2\text{OH}]^*$, whereas a dissociation into $[\text{CH}_3]^*$ and $[\text{OH}]^*$ in channel (3) could be neglected due to the small amount of methane (CH_4) detected, although such a dissociation could be predominantly found for short wavelengths (Terenin and Neujmin, 1935). In addition, although the dissociations through channels (1) and (2) cannot easily be distinguished in experiments, the authors anticipated that $[\text{CH}_2\text{OH}]^*$ could be formed from CH_3OH through the hydrogen abstraction of $[\text{CH}_3\text{O}]^*$ (Porter and Noyes, 1959). The predominance of channel (5) is in accordance with the results in Patat and Koch work (Patat and Koch, 1935) in which CH_2O and H_2 were observed in equal amounts, whereas $[\text{CH}_2\text{OH}]^*$ and $[\text{H}]^*$ were detected only in the initial stage of the mercury-sensitized reaction.

The photodissociation in channel (4) has been of interest because methylene (CH_2) can be formed in the atmosphere by the direct photolysis of CH_4 and because the singlet and triplet methylene (abbreviated $^1[\text{CH}_2]$ and $^3[\text{CH}_2]$, respectively) are the

smallest prototypical carbenes, which play important roles in various radical reactions (Kirmse, 1971; Shainyan, Kuzmin and Moskalik, 2013) such as alkene insertion in which carbenes react with alkenes to form cyclopropanes (De Frémont, Marion and Nolan, 2009). Experiments have shown that in the gas phase, $^1[\text{CH}_2]$ can be obtained from ketene by laser flash photolysis at 308 nm (Blitz, Pilling and Seakins, 2001), whereas $^3[\text{CH}_2]$ can be produced by collision-induced intersystem crossing with He or H_2 . The intersystem crossing between $^1[\text{CH}_2]$ and $^3[\text{CH}_2]$ through a collision is likely possible due to the small energy gap of approximately 38 kJ/mol between the singlet and triplet states (Leopold, Murray, Miller and Lineberger, 1985; McKellar, Bunker, Sears, Evenson, Saykally and Langhoff, 1983). Although *ab initio* calculations, at the CI(SD) level with a DZ and a DZP basis set (Bauschlicher and Shavitt, 1978), and experiments suggested that $^3[\text{CH}_2]$ is stable in the electronic ground (T_0) state and $^1[\text{CH}_2]$ is stable in the lowest singlet-excited (S_1) state, the hydrogen-bond (H-bond) complex formed from $^1[\text{CH}_2]$ and $[\text{H}_2\text{O}]$ is 10-13 kJ/mol more stable than that formed from $^3[\text{CH}_2]$ and $[\text{H}_2\text{O}]$ (Standard, 2016); the H-bond interaction energies were obtained based on single-point CCSD(T)-F12 and MRCI+Q calculations using the equilibrium structure obtained from the B3LYP-D3/aug-cc-pVTZ geometry optimizations.

In this work, the mechanisms of the photodissociations of single isolated CH_3OH in the S_1 state were studied using *ab initio* calculations at the complete active-space second-order perturbation theory (CASPT2) level. Our investigation considered single-photon photodissociation with the emphasis on nonradiative relaxation processes that bring the $S_0 \rightarrow S_1$ vertically excited molecule to the products in their

respective electronic ground states. To study the interplay between the structures and energetics in the S_0 and S_1 states, the potential energy curves for the photodissociations in channels (1)-(5) were constructed using a relax-scan method. The information on the electronic configurations in the dissociation processes was obtained from the analyses of the correlation interaction (CI) coefficients of the characteristic structures on the S_0 and S_1 potential energy curves. The theoretical results are discussed in comparison with available theoretical and experimental data.



CHAPTER II

COMPUTATIONAL METHODS

2.1 *Ab initio* calculations

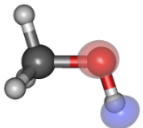
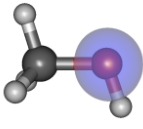
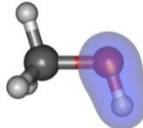
Since the photodissociation of CH₃OH involves the breaking and formation of covalent bonds, closed-shell and open-shell configurations must be considered in *ab initio* calculations (Gonzalez, Escudero and Serrano-Andres, 2012). To account for the multiconfigurational characteristics of the photolysis of CH₃OH, *ab initio* calculations were performed using the CASPT2 method, which has been accepted to be one of the standard methods used in excited-state calculations (Schreiber, Silva-Junior, Sauer and Thiel, 2008). Since the large-scale *ab initio* CI calculations suggested that the S₁ state of CH₃OH is represented by a Rydberg-like character (Kassab, Gleghorn and Evleth, 1983), which results from an adiabatic S₀→S₁ (n→3s) excitation, all of the S₁ state calculations were conducted adiabatically and restricted to C₁ symmetry. The use of C₁ symmetry is supported by the results of quantum chemical calculations, which showed that [CH₃O]^{*} possesses a Jahn-Teller distorted structure (Carter and Cook, 1991).

In this study, since the energy gradients with respect to the degrees of freedom had to be computed extensively, to optimize the computational resources, the aug-cc-pVDZ basis set was used. The augmented basis sets with diffuse functions were proven to be suitable for singlet-state calculations (Schreiber, Silva-Junior, Sauer and

Thiel, 2008); CASPT2 calculations with the aug-cc-pVDZ basis set were shown in our previous study to yield reasonable potential energy curves and $S_0 \rightarrow S_1$ vertical excitation energies for small water clusters (Suwannakham, Chaiwongwattana and Sagarik, 2018). As previous *ab initio* calculations (Wadt and Goddard, 1976) and our preliminary CASPT2 calculations showed that a single photon only excites an oxygen lone-pair of CH_3OH , CASPT2 calculations were performed by assigning four electrons ($n = 4$) in seven active orbitals ($m = 7$), whereas the rest were assigned in seven doubly occupied orbitals (close = 7), abbreviated CASPT2(4,7). To confirm that the complete active space chosen did not lead to serious errors in the excitation energies and shapes of the potential energy curves, some CASPT2 calculations were performed with an extended complete active space (CASPT2(16,12); $n = 16$, $m = 12$ and close = 2). For the CH_3OH molecule, CASPT2(4,7) and CASPT2(16,12) calculations involved 196 and 169,884 configuration state functions (CSFs), respectively.

To characterize the $S_0 \rightarrow S_1$ excited species, spatial distributions of the natural orbitals were computed and displayed with the same value of the isosurface (0.11) using GABEDIT software (Allouche, 2011). The information on the electronic configurations of structures in the S_0 and S_1 states was obtained from the analyses of the CI coefficients. All of the CASPT2 calculations were performed using the MOLPRO software package (MOLPRO, V.2015.1, 2015) with a state-specific method. The Werner-Meyer-Knowles nonlinear optimization method (Knowles and Werner, 1985; Werner and Knowles, 1985; Werner and Meyer, 1980) was used in the orbital/state optimizations. The details of the CASPT2 methods employed in this work are summarized in Table 2.1.

Table 2.1 The number of configuration state functions (CSFs) considered (N e-internal) and those generated by the CASPT2 methods (N-1 and N-2 e-internals) used in the calculations of CH₃OH. The values of the HOMO-1, HOMO and LUMO isosurfaces are 0.11.

| Structure | CASPT2 (n,m) | Number of CSFs | | | E ^{Ex} | S ₁ | | S ₀ | |
|---|------------------|------------------|------------------|-----------------|-----------------|---------------------------------|--------------|--------------------------|--------------|
| | | N e-internal | N-1 e-internal | N-2 e-internal | | Conf. | CI Coeff. | Conf. | CI coeff. |
|  LUMO | (4,7) [16,12] | 196 [169,884] | 112 [339,768] | 49 [608,751] | 6.74 [6.48] | $\Psi_9^{\overline{10}}$ | 0.9850 | Ψ_0 | 0.9829 |
|  HOMO | | | | | | $\Psi_{9,9}^{10,\overline{12}}$ | 0.0909 | $\Psi_9^{\overline{12}}$ | 0.0730 |
|  HOMO-1 | | | | | | | | | |

n = number of active electrons; m = number of active orbitals; [..] = value obtained from CASPT2(16,12) calculations.

2.2 Equilibrium geometries and potential energy curves

To obtain fundamental information on the photodissociation processes, equilibrium geometries of CH₃OH in the S₀ and S₁ states were optimized using CASPT2(4,7) calculations with the quadratic steepest decent (QSD) method (Sun and Ruedenberg, 1994) included in the MOLPRO software package. Due to strong fluctuation in the electronic-excitation energy, the transition structure at the saddle point on the potential energy surface cannot be optimized within reasonable convergence criteria, e.g., the total energy fluctuation within 1.0×10^{-6} au and the maximum norm of the Cartesian gradient smaller than 1.0×10^{-4} au (TURBOMOLE V7.2, 2018). To search for the transition structures in dissociation channels (1)–(3), the S₁ potential energy curves with respect to the O–H, C–H and C–O coordinates were constructed. In contrast to previous studies, which employed freeze-scan methods (Buenker, Olbrich, Schuchmann, Schuermann and Sonntag, 1984; Marston, Weide, Schinke and Suter, 1993; Cheng, Bahou, Chen, Yui, Lee and Lee, 2002; Wen, Segall, Dulligan and Wittig, 1994), the present work used a relax-scan method, in which all of the important structural parameters on the S₁ potential energy curves were optimized using CASPT2(4,7) calculations.

Since preliminary CASPT2(4,7) calculations showed that the C–H bond lengths did not significantly change on the S₁ potential energy curves, to reduce the computational efforts, the C–H bond distances were constrained at the equilibrium value in the S₀ state ($R_{\text{C-H}} = 1.10 \text{ \AA}$). In addition, because the O–H dissociation is the most preferential process in the S₁ state, the S₁ potential energy curves for the C–H and C–O dissociations were tentatively constructed by constraining the O–H distance at the equilibrium value in the S₀ state ($R_{\text{O-H}} = 0.97 \text{ \AA}$). The S₁ potential energy

curves with a constrained O–H distance were calculated to search for the precursors in the S_0 state, from which the $S_0 \rightarrow S_1$ vertical excitations lead to the transition structures for the C–H and C–O dissociations in the S_1 state.

Since isomerization-mediated dissociation is one of the most common radical reactions, unimolecular $[\text{CH}_3\text{OH}] \rightarrow [\text{CH}_2\text{OH}_2]$ isomerization, which leads to the $[\text{CH}_2]$ and $[\text{H}_2\text{O}]$ products in channel (4), was constructed. While constraining the O–H distance at 0.97 Å, the intramolecular isomerization was simulated by transferring one of the hydrogen atoms from the CH_3 group to the OH group. Since previous theoretical and experimental studies confirmed that in the electronic ground state $^3[\text{CH}_2]$ is more stable than $^1[\text{CH}_2]$ and because the single-point single-reference CCSD(T)-F12 method predicted that the $^1[\text{CH}_2]\text{--}[\text{H}_2\text{O}]$ H-bond complex is more associated than the $^3[\text{CH}_2]\text{--}[\text{H}_2\text{O}]$ H-bond complex, the singlet-triplet intersystem crossing and the H-bond formation were taken into account in channel (4) by performing CASPT2(4,7) geometry optimizations on the $[\text{CH}_2]\text{--}[\text{H}_2\text{O}]$ H-bond complex in the S_0 and T_0 states. In addition, because formaldehyde formation was suggested to involve a nonconcerted process, in which the dehydrogenation proceeds after the O–H dissociation (Buenker, Olbrich, Schuchmann, Schuermann and Sonntag, 1984), to discuss the mechanism in channel (5), the S_1 potential energy curve for the H_2 elimination was constructed using the O–H dissociated products in channel (1) ($[\text{CH}_3\text{O}]^\bullet$ and $[\text{H}]^\bullet$) as the precursors. All of the constrained structural parameters and degrees of freedom used in the calculations of the S_1 potential energy curves are summarized in Figure 2.1.

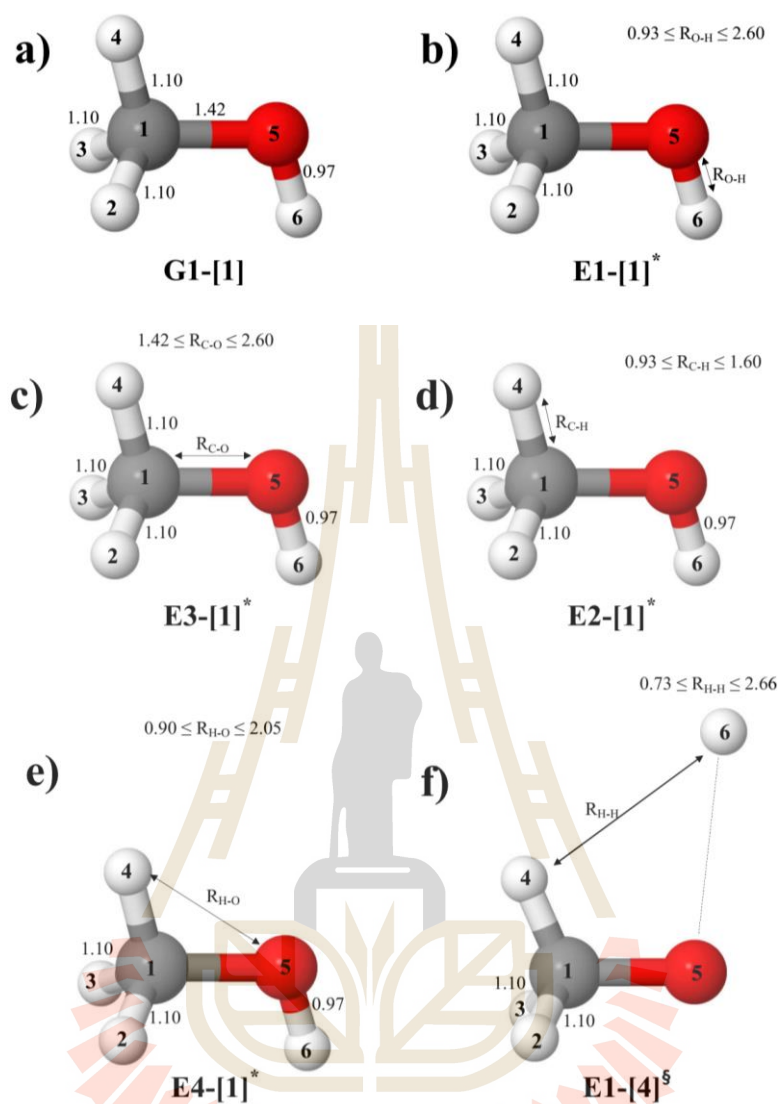


Figure 2.1 a) Equilibrium structure of CH_3OH in the S_0 state obtained from CASPT2(4,7) geometry optimizations. b)-f) Constrained structural parameters used in the calculations of the S_1 relax-scan potential energy curves for dissociation channels (1)–(5), respectively. Double sided arrows represent the degrees of freedom used in the calculations of the S_1 relax-scan potential energy curves. Distances are in Å.

CHAPTER III

RESULTS AND DISCUSSION

To facilitate the discussion, characteristic structures of CH₃OH in the S₀ and S₁ states are labeled with a three-character code, e.g., Gk-[l] and Ek-[l][‡] or Ek-[l]^{*}, where G = structure in the S₀ state; E = structure in the S₁ state; and k = dissociation channels (1)-(5). Different CH₃OH structures in the same dissociation channel are distinguished by [l]. * and ‡ denote the vertically excited structures and structures at the intersection of the S₀ and S₁ potential energy curves, respectively, whereas † labels transition structures. For example, based on this three-character code, structures G1-[1]^{*} and E1-[1]^{*} are the same structures (l = 1) computed in the S₀ and S₁ states, G and E, respectively. They are involved in the O–H dissociation in channel (1) (k = 1). Structures E4-[1]^{*} and E4-[2][‡] are different structures (l = 1 and 2) on the S₁ potential energy curve for the [CH₃OH]→[CH₂OH₂] isomerization (k = 4). They are vertically excited (*) and transition structures (‡), respectively.

The characteristic structures and energies for the O–H dissociation as well as the three leading electronic configurations and CI coefficients (cut-off = 0.05) obtained from CASPT2(4,7) calculations are given as examples in Table 2.1, where Ψ_0 and C_0 = electronic ground state; Ψ_a^r and C_a^r = a→r singly excited state (S-type); and $\Psi_{a,b}^{r,s}$ and $C_{a,b}^{r,s}$ = a→r and b→s doubly excited state (D-type). The indices a and b along with r and s label occupied and virtual or unoccupied spin orbitals, respectively;

a bar or lack of a bar is to denote beta (β) and alpha (α) spin orbitals, respectively. The potential energy curves with respect to the O–H, C–O and C–H coordinates as well as variations of selected structural parameters are shown in Figures 3.1-3.3 respectively. The potential energy curves for the $[\text{CH}_3\text{OH}] \rightarrow [\text{CH}_2\text{OH}_2]$ isomerization and formaldehyde formation are shown in Figure 3.4 and Figure 3.7 respectively. The energies and structural parameters of the characteristic structures of CH_3OH on the potential energy curves are summarized in Table 3.1. The three leading electronic configurations and CI coefficients of the characteristic structures are included in Tables 3.3-3.6.

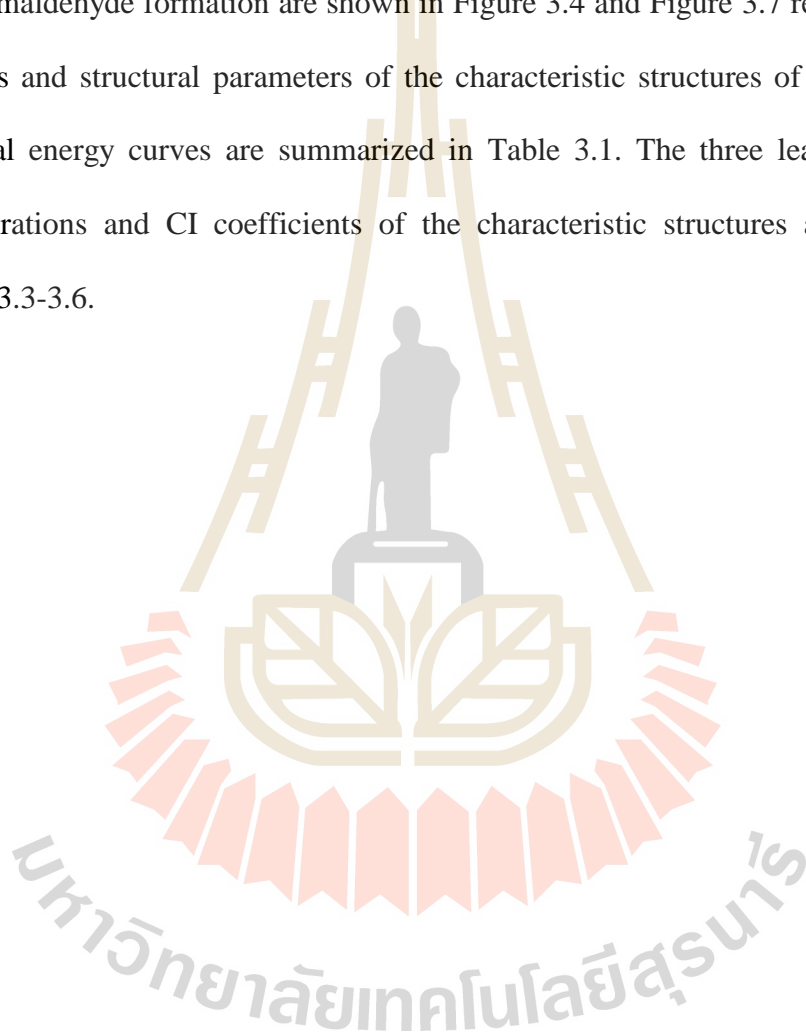


Table 3.1 Characteristic structures, structure parameters and energetics of CH₃OH, observed on the potential energy curves obtained from CASPT2(4,7) calculations.

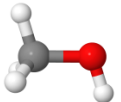
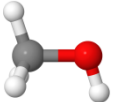
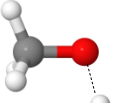
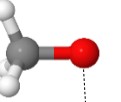
| | E^{Tot} | E^{Ex} | C-H | | $R_{\text{C}(1)\text{O}(5)}$ | $R_{\text{O}(5)\text{H}(6)}$ | $\angle\text{H}(2)\text{C}(1)\text{O}(5)$ | $\angle\text{H}(4)\text{C}(1)\text{O}(5)$ | $\angle\text{H}(2)\text{C}(1)\text{H}(3)$ | $\angle\text{H}(2)\text{C}(1)\text{H}(4)$ | $\angle\text{H}(6)\text{O}(5)\text{C}(1)$ |
|---|--------------------------|--|------------------------------|------------------------------|------------------------------|------------------------------|---|---|---|---|---|
| | | | $R_{\text{C}(1)\text{H}(2)}$ | $R_{\text{C}(1)\text{H}(4)}$ | | | | | | | |
|  G1-11 | -115.1694 [-115.1890] | 0.2477 (6.74) [0.2382] [(6.48)] | 1.10 [1.10] | 1.10 [1.10] | 1.42 [1.44] | 0.97 [0.97] | 112 [112] | 107 [107] | 109 [109] | 108 [108] | 108 [107] |
|  E1-11* | -115.1749 | 0.2353 (6.40) | 1.10 | 1.10 | 1.42 | 0.97 | 105 | 108 | 106 | 116 | 108 |
|  E1-21 [†] | -115.2061 | 0.1389 (3.67) | 1.10 | 1.10 | 1.39 | 1.40* | 107 | 113 | 106 | 112 | 105 |
|  E1-31 [§] | -115.2472 | 0.0008 (0.02) | 1.10 | 1.10 | 1.39 | 2.60 | 108 | 114 | 106 | 110 | 93 |

Table 3.1 (Continued) Characteristic structures, structure parameters and energetics of CH₃OH, observed on the potential energy curves obtained from CASPT2(4,7) calculations.

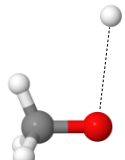
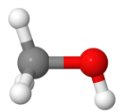
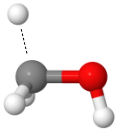
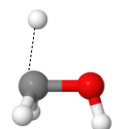
| | E ^{Tot} | E ^{Ex} | C-H | | R _{C(1)O(5)} | R _{O(5)H(6)} | ∠H _{(2)C(1)O(5)} | ∠H _{(4)C(1)O(5)} | ∠H _{(2)C(1)H(3)} | ∠H _{(2)C(1)H(4)} | ∠H _{(6)O(5)C(1)} |
|--|------------------|------------------|-----------------------|-----------------------|-----------------------|-----------------------|---------------------------|---------------------------|---------------------------|---------------------------|---------------------------|
| | | | R _{C(1)H(2)} | R _{C(1)H(4)} | | | | | | | |
|  E1-[4] [§] | -115.2471 | 0.0003 (0.01) | 1.10 | 1.10 | 1.39 | 2.60 | 108 | 113 | 106 | 110 | 97 |
|  E2-[1] [*] | -115.1749 | 0.2352 (6.40) | 1.10 | 1.10 | 1.42 | 0.97 | 105 | 108 | 106 | 116 | 108 |
|  E2-[2] [†] | -115.1190 | 0.2465 (6.71) | 1.10 | 1.50 [*] | 1.44 | 0.97 | 105 | 102 | 111 | 116 | 105 |
|  E2-[3] [§] | -115.1191 | 0.2290 (6.23) | 1.10 | 1.70 | 1.44 | 0.97 | 99 | 87 | 99 | 130 | 106 |

Table 3.1 (Continued) Characteristic structures, structure parameters and energetics of CH₃OH, observed on the potential energy curves obtained from CASPT2(4,7) calculations.

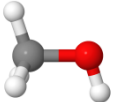
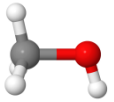
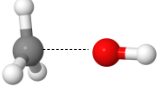
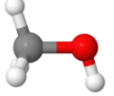
| | E ^{Tot} | E ^{Ex} | C-H | | R _{C(1)O(5)} | R _{O(5)H(6)} | ∠H _{(2)C(1)O(5)} | ∠H _{(4)C(1)O(5)} | ∠H _{(2)C(1)H(3)} | ∠H _{(2)C(1)H(4)} | ∠H _{(6)O(5)C(1)} |
|---|------------------|------------------|-----------------------|-----------------------|-----------------------|-----------------------|---------------------------|---------------------------|---------------------------|---------------------------|---------------------------|
| | | | R _{C(1)H(2)} | R _{C(1)H(4)} | | | | | | | |
|  E3-[1] [*] | -115.1749 | 0.2354 (6.41) | 1.10 | 1.10 | 1.42 | 0.97 | 105 | 108 | 106 | 116 | 108 |
|  E3-[2] [†] | -115.1692 | 0.2319 (6.31) | 1.10 | 1.10 | 1.60 [*] | 0.97 | 102 | 102 | 112 | 118 | 107 |
|  E3-[3] [§] | -115.2309 | 0.0495 (1.35) | 1.10 | 1.10 | 2.30 | 0.97 | 100 | 99 | 118 | 119 | 178 |
|  E4-[11] [*] | -115.1747 | 0.2353 (6.40) | 1.10 | 1.08 | 1.41 | 0.97 | 105 | 106 | 106 | 117 | 108 |

Table 3.1 (Continued) Characteristic structures, structure parameters and energetics of CH₃OH, observed on the potential energy curves obtained from CASPT2(4,7) calculations.

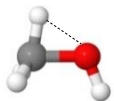
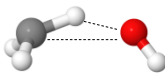
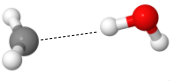
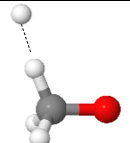
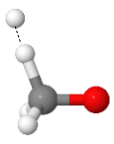
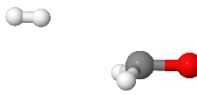
| | E^{Tot} | E^{Ex} | C-H | | $R_{\text{C}(1)\text{O}(5)}$ | $R_{\text{O}(5)\text{H}(6)}$ | $\angle\text{H}(2)\text{C}(1)\text{O}(5)$ | $\angle\text{H}(4)\text{C}(1)\text{O}(5)$ | $\angle\text{H}(2)\text{C}(1)\text{H}(3)$ | $\angle\text{H}(2)\text{C}(1)\text{H}(4)$ | $\angle\text{H}(6)\text{O}(5)\text{C}(1)$ |
|--|------------------|------------------|------------------------------|------------------------------|------------------------------|------------------------------|---|---|---|---|---|
| | | | $R_{\text{C}(1)\text{H}(2)}$ | $R_{\text{C}(1)\text{H}(4)}$ | | | | | | | |
|  E4-[2] [†] | -115.1396 | 0.2381 (6.48) | 1.10 | 1.05 | 1.40* | 0.97 | 108 | 80 | 111 | 122 | 111 |
|  E4-[3] | -115.2390 | 0.0237 (0.64) | 1.10 | 1.20 | 2.64 | 0.97 | 105 | 21 | 110 | 116 | 123 |
|  E4-[4] | -115.2434 | 0.0101 (0.27) | 1.09 | 2.30 | 3.26 | 0.97 | 106 | - | 143 | 106 | 108 |

Table 3.1 (Continued) Characteristic structures, structure parameters and energetics of CH₃OH, observed on the potential energy curves obtained from CASPT2(4,7) calculations.

| | E^{Tot} | E^{Ex} | C-H | | $R_{\text{C}(1)\text{O}(5)}$ | $R_{\text{O}(5)\text{H}(6)}$ | $\angle\text{H}(2)\text{C}(1)\text{O}(5)$ | $\angle\text{H}(4)\text{C}(1)\text{O}(5)$ | $\angle\text{H}(2)\text{C}(1)\text{H}(3)$ | $\angle\text{H}(2)\text{C}(1)\text{H}(4)$ | $\angle\text{H}(6)\text{O}(5)\text{C}(1)$ |
|---|------------------|------------------|------------------------------|------------------------------|------------------------------|------------------------------|---|---|---|---|---|
| | | | $R_{\text{C}(1)\text{H}(2)}$ | $R_{\text{C}(1)\text{H}(4)}$ | | | | | | | |
|  E5-[1] | -115.2427 | 0.0024 (0.06) | 1.10 | 1.11 | 1.39 | 3.26 | 108 | 108 | 107 | 110 | 52 |
|  E5-[2] [†] | -115.2270 | 0.0557 (1.52) | 1.10 | 1.31 | 1.37 | 2.93 | 111 | 111 | 111 | 112 | 46 |
|  E5-[3] | -115.2445 | 0.0964 (2.62) | 1.10 | 2.93 | 1.35 | - | 114 | 114 | 120 | - | - |

3.1 Equilibrium structures

The equilibrium structure of CH₃OH in the electronic ground state obtained from CASPT2(4,7) calculations is shown in Figure 2.1a (structure G1-[1] with $R_{O(5)-H(6)} = 0.97 \text{ \AA}$, $R_{C(1)-H(2)} = 1.10 \text{ \AA}$, $R_{C(1)-O(5)} = 1.42 \text{ \AA}$, $\angle H(2)C(1)H(3) = 109^\circ$, and $\angle H(6)O(5)C(1) = 108^\circ$). The values are comparable with those obtained from the microwave and millimeter wave spectrum ($R_{O(5)-H(6)} = 0.95 \text{ \AA}$, $R_{C(1)-H(2)} = 1.09 \text{ \AA}$, $R_{C(1)-O(5)} = 1.42 \text{ \AA}$, $\angle H(2)C(1)H(3) = 108^\circ$ and $\angle H(6)O(5)C(1) = 108^\circ$) (Gerry, Lees and Winnewisser, 1976). The structural parameters obtained from CASPT2(16,12) geometry optimizations are approximately the same ($R_{O(5)-H(6)} = 0.97 \text{ \AA}$, $R_{C(1)-H(2)} = 1.10 \text{ \AA}$, $R_{C(1)-O(5)} = 1.44 \text{ \AA}$, $\angle H(2)C(1)H(3) = 109^\circ$, and $\angle H(6)O(5)C(1) = 107^\circ$). The $S_0 \rightarrow S_1$ vertical excitation energies obtained from CASPT2(4,7) and (16,12) calculations are 6.74 eV (184 nm) and 6.48 eV (191 nm), respectively. These values are in excellent agreement with *ab initio* MRD-CI calculations (Buenker, Olbrich, Schuchmann, Schuermann and Sonntag, 1984) and the experiments (Cheng, Bahou, Chen, Yui, Lee and Lee, 2002) at 6.94 eV (179 nm) and 6.75 eV (183 nm), respectively.

For the structure G1-[1], the shapes of the HOMO-1 ($n_{\text{orb}} = 8$), HOMO ($n_{\text{orb}} = 9$) and LUMO ($n_{\text{orb}} = 10$) in Table 2.1 show the electron density distributions for the O–H bonding, lone-pair and O–H anti-bonding natural orbitals, respectively. The CI coefficients obtained from CASPT2(4,7) calculations reveal that in the S_0 state, the ground state configuration Ψ_0 dominates with a small contribution from the singly excited configuration $\Psi_9^{\overline{12}}$ ($C_0 = 0.9829$ and $C_9^{\overline{12}} = 0.0730$), whereas in the S_1 state, the singly excited configuration $\Psi_9^{\overline{10}}$ is dominant with a small contribution from the doubly excited configuration $\Psi_{9,9}^{10,\overline{12}}$ ($C_9^{\overline{10}} = 0.9850$ and $C_{9,9}^{10,\overline{12}} = 0.0909$).

3.2 The O–H dissociation

The S_1 potential energy curves with respect to the O–H coordinates obtained from the CASPT2(4,7) and (16,12) methods are illustrated in Figure 3.1. The total energies of the CASPT2(16,12) method were calculated at the CASPT2(4,7) geometries. It appears that the shapes of the S_1 potential energy curves obtained from both methods are approximately the same; the S_0 and S_1 potential energy curves obtained from CASPT2(16,12) calculations are systematically lower than those obtained from CASPT2(4,7) calculations. These findings confirm the applicability of the CASPT2(4,7) method in the calculations of the potential energy curves of CH_3OH , and only the CASPT2(4,7) results were discussed in this study.

The S_1 potential energy curves in Figure 3.1 reveal that the $S_0 \rightarrow S_1$ vertical excitation of structure G1-[1] leads to structure E1-[1]*. Structure E1-[1]* is transformed into structure E1-[2][‡], in which the O–H dissociation occurs at $R_{\text{O}(5)\text{-H}(6)} = 1.40 \text{ \AA}$. The shape of the LUMO in Figure 3.1 suggests that structure E1-[2][‡] is a $[\text{CH}_3\text{O}]^\cdot \cdots [\text{H}]^\cdot$ radical pair (diradical), which is dissociated into the $[\text{CH}_3\text{O}]^\cdot$ and $[\text{H}]^\cdot$ products in their respective electronic ground states at the intersection of the S_0 and S_1 states at $R_{\text{O}(5)\text{-H}(6)} = 2.60 \text{ \AA}$ (structure G1-[3][§] with $E^{\text{Ex}} \approx 0 \text{ eV}$). Figure 3.1 also shows that the extension of the O–H bond in the S_1 state is accompanied by a shortening of the C–O bond from $R_{\text{C}(1)\text{-O}(5)} = 1.42 \text{ \AA}$ in structure E1-[1]* to $R_{\text{C}(1)\text{-O}(5)} = 1.39 \text{ \AA}$ in structures E1-[2][‡] and E1-[3][§].

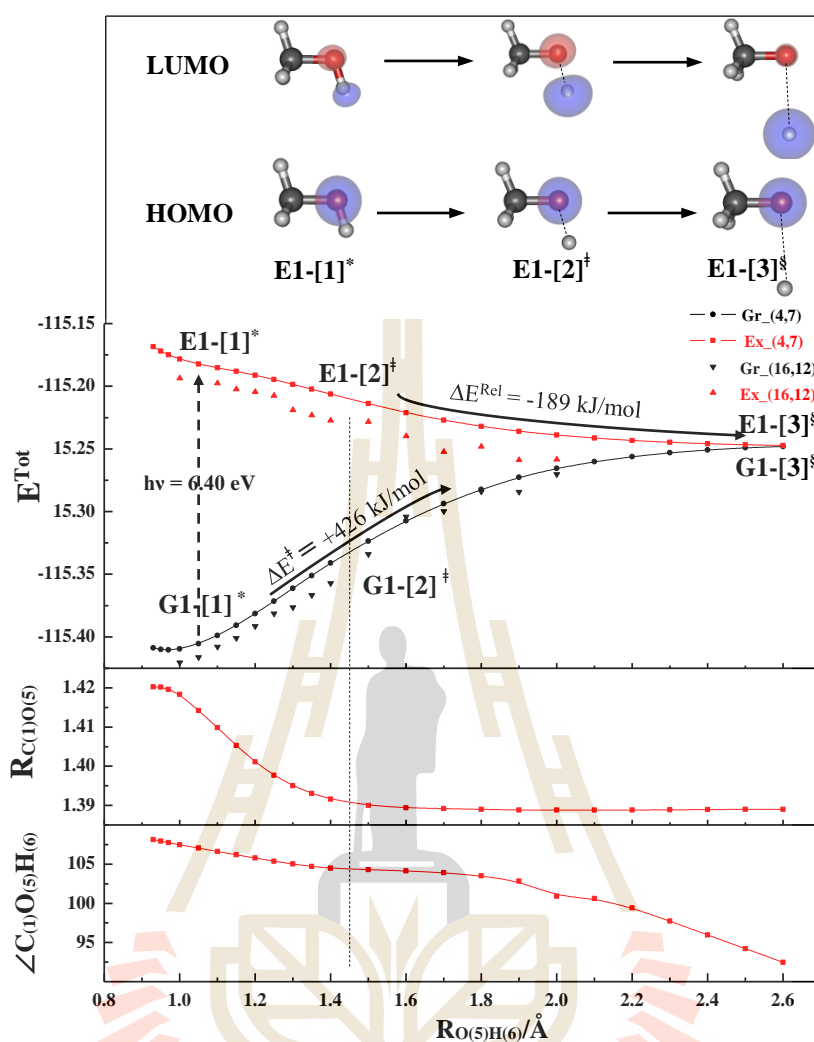


Figure 3.1 The relax-scan potential energy curves with respect to the O-H coordinate obtained from CASPT2 calculations. The energies, distances and angles are in au, Å and degrees, respectively. The values of the HOMO and LUMO isosurfaces are 0.11. ΔE^{Rel} = energy release; ΔE^{\ddagger} = energy barrier; \ddagger = transition structure; \S = structure at the intersection of the S_0 and S_1 potential energy curves; Gr_(4,7) and Ex_(4,7) = total energies obtained from CASPT2(4,7) calculations in the S_0 and S_1 states, respectively; and Gr_(16,12) and Ex_(16,12) = total energies obtained from CASPT2(16,12) calculations in the S_0 and S_1 states, respectively.

Since the transformation of structure E1-[1]^{*} into E1-[3][‡] in the S₁ state occurs through homolytic cleavage of the O–H bond along a purely repulsive potential energy curve, based on the approximation that structure E1-[1]^{*} is dissociated into the [CH₃O]· and [H]· products in their respective electronic ground states at R_{O(5)–H(6)} = 2.60 Å, the energy release due to the exothermic process could be approximated as $\Delta E^{\text{Rel}} = -189$ kJ/mol. This value is in excellent agreement with the available energy (188 kJ/mol) following the production of [CH₃O]· and [H]· in the experiment via the absorption of a 193 nm photon (Satyapal, Park, Bersohn and Katz, 1989). Since the experiment showed that 82% of the energy release (ΔE^{Rel}) is the translational energy (Satyapal, Park, Bersohn and Katz, 1989), the maximum kinetic energy of 155 kJ/mol (equivalent to 18,640 K) could be transferred to another CH₃OH molecule.

In the electronic ground (S₀) state, the energy barrier (ΔE^\ddagger) for the O–H dissociation amounts to 426 kJ/mol, which is also in excellent agreement with the experimental value of 422 kJ/mol (Harding, Schlegel, Krishnan and Pople, 1980); in the S₀ state, *ab initio* MRD-CI calculations based on a freeze-scan method yielded a slightly smaller energy barrier of $\Delta E^\ddagger = 418$ kJ/mol (Buenker, Olbrich, Schuchmann, Schuermann and Sonntag, 1984). Therefore, the O–H dissociation in channel (1) is confirmed to be the most favorable in the S₁ state, which is in accordance with all of the previous theoretical and experimental studies (Satyapal, Park, Bersohn and Katz, 1989; Marston, Weide, Schinke and Suter, 1993; Chen, Eppink, Jiang, Groenenboom, Yang and Parker, 2011; Baker, Butcher, Dyke and Morris, 1990).

The values of the CI coefficients in Table 3.2 show the dependence of the electronic configurations on the O–H distance. Especially in the S₀ state, while the CI

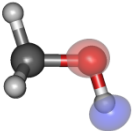
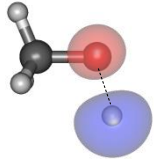
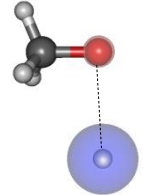
coefficient of Ψ_0 gradually decreases from $C_0 = 0.9830$ for structure G1-[1]^{*} to $C_0 = 0.9511$ for structure G1-[2][†] and to $C_0 = 0.4241$ for structure G1-[3][§], the contribution of the singly excited configuration $\Psi_8^{\overline{10}}$ is increased in the transition structure and becomes dominant at the intersection of the S_0 and S_1 states, where $C_8^{\overline{10}} = 0.1997$ and 0.8581 for structures G1-[2][†] and G1-[3][§], respectively. The situation seems to be different in the S_1 state, in which only the CI coefficient of the singly excited configuration $\Psi_9^{\overline{10}}$ dominates and varies only in a narrow range on the S_1 potential energy curve; the contribution of $\Psi_9^{\overline{10}}$ varies from $C_9^{\overline{10}} = 0.9850$ for structure E1-[1]^{*} to $C_9^{\overline{10}} = 0.9639$ for structure E1-[2][†] and to $C_9^{\overline{10}} = 0.9746$ for structure E1-[3][§]. It should be noted that at the intersection of the S_0 and S_1 states (at long O–H distances), the lone-pair natural orbitals of the oxygen atom are degenerate; the energies and shapes of the HOMO-1 ($n_{\text{orb}} = 8$) and HOMO ($n_{\text{orb}} = 9$) are approximately the same. Therefore, the singly excited states $\Psi_8^{\overline{10}}$ and $\Psi_9^{\overline{10}}$ of structures G1-[3][§] and E1-[3][§] are equivalent.

Analysis of the CI coefficients in Table 3.2 also shows that in the S_0 state, the electronic configuration inversion, in which the singly excited state $\Psi_8^{\overline{10}}$ with a higher energy becomes more important than the electronic ground state Ψ_0 with a lower energy, results in an increase in the total energy and leads to the convergence of the S_0 and S_1 potential energy curves at long O–H distances. Therefore, the electronic configuration inversion $\Psi_0 \rightarrow \Psi_8^{\overline{10}}$ can be considered as characteristic of the O–H dissociation, with $R_{\text{O}(5)\text{-H}(6)} = 1.40 \text{ \AA}$ (structure E1-[2][†]) being the “threshold structural parameter” for the inversion. The electronic configuration inversion explains why the

O–H dissociation is a strong endothermic process (with a high ΔE^\ddagger) in the S_0 state, whereas the lack of electronic configuration inversion in the S_1 state results in a purely repulsive potential energy curve.



Table 3.2 Characteristic structures of CH₃OH on the S₀ and S₁ potential energy curves for the O–H dissociation. The electronic configurations and CI coefficients were obtained from CASPT2(4,7) calculations in the S₀ and S₁ states. The values of the LUMO isosurfaces are 0.11.

| Structure | S ₁ | | Structure | S ₀ | |
|---|--|-----------|-----------|--|-----------|
| | Conf. | CI Coeff. | | Conf. | CI Coeff. |
| E1-[1]*  | $\Psi_9^{\overline{10}}$ | 0.9850 | G1-[1]* | Ψ_0 | 0.9830 |
| | $\Psi_{9,9}^{\overline{10},\overline{12}}$ | 0.0890 | | $\Psi_9^{\overline{12}}$ | 0.0723 |
| | $\Psi_{9,8,8}^{\overline{10},\overline{11},\overline{11}}$ | 0.0715 | | $\Psi_{8,8}^{\overline{11},\overline{11}}$ | 0.0698 |
| E1-[2]†  | $\Psi_9^{\overline{10}}$ | 0.9639 | G1-[2]† | Ψ_0 | 0.9511 |
| | $\Psi_{9,8}^{\overline{10},\overline{10}}$ | 0.2262 | | $\Psi_8^{\overline{10}}$ | 0.1997 |
| | $\Psi_9^{\overline{11}}$ | 0.0496 | | $\Psi_{8,8}^{\overline{10},\overline{10}}$ | 0.1719 |
| E1-[3]§  | $\Psi_9^{\overline{10}}$ | 0.9746 | G1-[3]§ | $\Psi_8^{\overline{10}}$ | 0.8581 |
| | $\Psi_{9,8}^{\overline{10},\overline{10}}$ | 0.1973 | | Ψ_0 | 0.4241 |
| | $\Psi_{9,8,8}^{\overline{10},\overline{12},\overline{12}}$ | 0.0604 | | $\Psi_{8,8}^{\overline{10},\overline{10}}$ | 0.2688 |

3.3 The C–O dissociation

Due to the predominance of the O–H dissociation in the S_1 state, to study the C–O dissociation (channel (3)), the O–H dissociation must be temporarily suppressed. The S_1 potential energy curve with respect to the C–O coordinate was constructed by constraining the O–H distance at the ground-state equilibrium distance ($R_{O(5)-H(6)} = 0.97 \text{ \AA}$). The S_1 potential energy curve in Figure 3.2 shows that starting from the $S_0 \rightarrow S_1$ vertically excited structure E3-[1]^{*} with $R_{C(1)-O(5)} = 1.42 \text{ \AA}$, the C–O dissociation occurs through a transformation of the CH₃ structure from a pyramidal (structure E3-[1]^{*}) to planar structure (structure E3-[3][§]), with the C–O bond cleavage at approximately $R_{C(1)-O(5)} = 1.60 \text{ \AA}$ (structure E3-[2][†]) and the energy barrier $\Delta E^\ddagger = 15.0 \text{ kJ/mol}$. The relaxation of structure E3-[2][†] to structure E3-[3][§] at $R_{C(1)-O(5)} = 2.30 \text{ \AA}$ is an exothermic process with $\Delta E^{\text{Rel}} = -227 \text{ kJ/mol}$ and is accompanied by a decrease in $\angle H(4)C(1)O(5)$ from 109° in structure E3-[1]^{*} to 97° in structure E3-[3][§].

It should be noted that the S_1 potential energy curve for the C–O dissociation was calculated by constraining the O–H distance at $R_{O(5)-H(6)} = 0.97 \text{ \AA}$, and without this constraint, the reaction will preferentially proceed on the O–H dissociation path. To confirm that the transition structure for the C–O dissociation is structure E3-[2][†] with $R_{C(1)-O(5)} = 1.60 \text{ \AA}$, CASPT2(4,7) geometrical optimizations without any geometrical constraints were performed on structure E3-[2][†], starting from the $R_{C(1)-O(5)}$ distances slightly shifted, where $R_{C(1)-O(5)} = 1.55$ and 1.65 \AA . The results show that for $R_{C(1)-O(5)} = 1.55 \text{ \AA}$, structure E3-[2][†] relaxes to structure E1-[3][§] (the O–H dissociated structure), whereas for $R_{C(1)-O(5)} = 1.65 \text{ \AA}$, the C–O dissociation occurs, leading to the [CH₃][·] and [OH][·] products (structure E3-[3][§]) in their respective

electronic ground states. Therefore, $R_{C(1)-O(5)} = 1.60 \text{ \AA}$ can be regarded as the threshold structural parameter for the C–O dissociation.

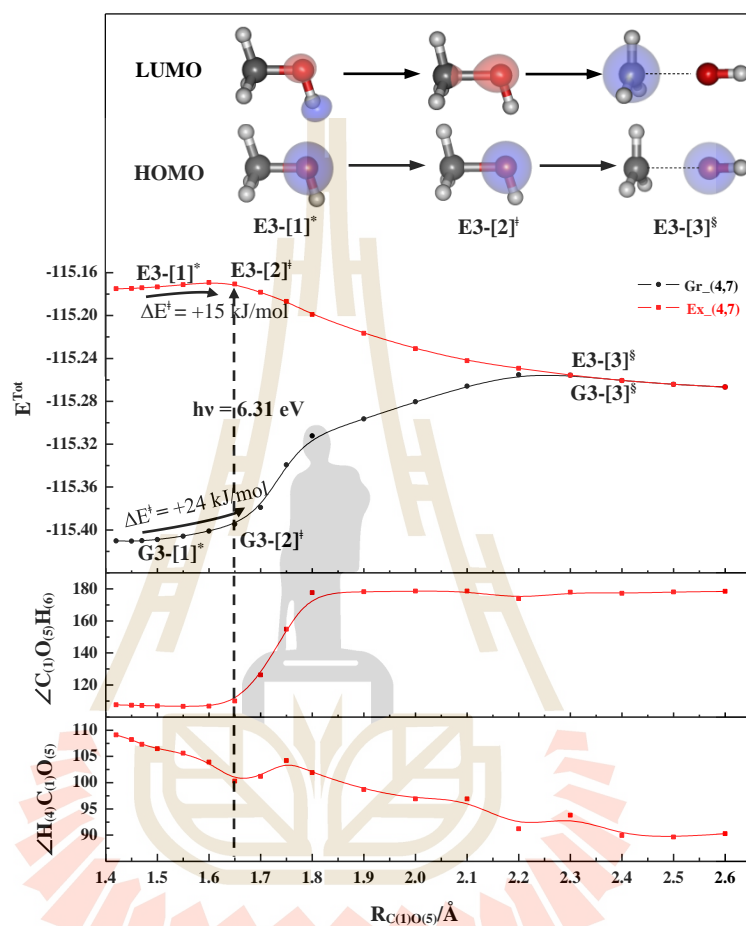


Figure 3.2 The relax-scan potential energy curves with respect to the C–O coordinate obtained from CASPT2 calculations. The energies, distances and angles are in au, \AA and degrees, respectively. The values of the HOMO and LUMO isosurfaces are 0.11. ΔE^{Rel} = energy release; ΔE^{\ddagger} = energy barrier; \ddagger = transition structure; \S = structure at the intersection of the S_0 and S_1 potential energy curves; Gr_(4,7) and Ex_(4,7) = total energies obtained from CASPT2(4,7) calculations in the S_0 and S_1 states, respectively; and Gr_(16,12) and Ex_(16,12) = total energies obtained from CASPT2(16,12) calculations in the S_0 and S_1 states, respectively.

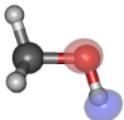
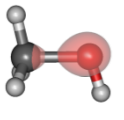
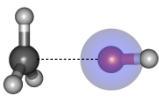
These pieces of information suggest that the photodissociation of the C–O bond cannot proceed through the $S_0 \rightarrow S_1$ vertical excitation of the ground-state equilibrium structure (structure G1-[1]). However, the S_0 and S_1 potential energy curves in Figure 3.2 reveal an alternative path, namely, before the $S_0 \rightarrow S_1$ vertical excitation, a precursor for the C–O dissociation can be generated by thermal excitation in the S_0 state, structure G3-[2][‡] with $R_{C(1)-O(5)} = 1.60 \text{ \AA}$ (at the threshold distance) and an energy barrier of $\Delta E^\ddagger = 24 \text{ kJ/mol}$. As the precursor, structure G3-[2][‡] is $S_0 \rightarrow S_1$ vertically excited ($E^{\text{Ex}} = 6.31 \text{ eV}$ (196 nm)) to the transition structure E3-[2][‡], which is then dissociated on the barrier-less S_1 potential energy curve into the $[\text{CH}_3]^\cdot$ and $[\text{OH}]^\cdot$ products at the intersection of the S_0 and S_1 states, structure E3-[3][§]. Based on the Boltzmann distribution and the approximation that all of the kinetic energy release in channel (1) (-155 kJ/mol, 18,640 K), is transferred to structure G1-[1], 46% of structure G1-[1] can be thermally excited to structure G3-[2][‡].

The proposed mechanism supports the laser-induced fluorescence experiment at 193 nm (Satyapal, Park, Bersohn and Katz, 1989), which showed that the C–O dissociation in channel (3) is a minor process and the thermal excitation of the CH_3O mode prior to the $S_0 \rightarrow S_1$ excitation increases the quantum yield for the C–O dissociation into $[\text{CH}_3]^\cdot$ and $[\text{OH}]^\cdot$ (Marston, Weide, Schinke and Suter, 1993). Our theoretical results suggest that the branching ratio for channel (3) is increased because the population of the precursor in the electronic ground state (structure G3-[2][‡]) is growing upon thermal (vibrational) excitation prior to the photoexcitation. The suggestion that the thermal excitation leads to an increase in the $[\text{CH}_3]^\cdot$ and $[\text{OH}]^\cdot$ products is also in accordance with the state-selective laser photofragment

spectroscopic results in Schmiedl, Meier and Welge work (Schmiedl, Meier and Welge, 1981).



Table 3.3 Characteristic structures of CH₃OH on the S₀ and S₁ potential energy curves for the C–O dissociation. The electronic configurations and CI coefficients were obtained from CASPT2(4,7) calculations in the S₀ and S₁ states. The values of the LUMO isosurfaces are 0.11.

| Structure | S ₁ | | Structure | S ₀ | |
|---|---|-----------|---------------------|---|-----------|
| | Conf. | CI Coeff. | | Conf. | CI Coeff. |
| E3-[1]*  | $\Psi_{9}^{\overline{10}}$ | 0.9849 | G3-[1]* | Ψ_0 | 0.9830 |
| | $\Psi_{9,9}^{10,\overline{12}}$ | 0.0902 | | $\Psi_{9}^{\overline{12}}$ | 0.0724 |
| | $\Psi_{9,8}^{\overline{10},10}$ | 0.0686 | | $\Psi_{8,8}^{\overline{11},11}$ | 0.0699 |
| E3-[2] [†]  | $\Psi_{9}^{\overline{10}}$ | 0.9803 | G3-[2] [†] | Ψ_0 | 0.9781 |
| | $\Psi_{9,8,8}^{\overline{10},\overline{11},11}$ | 0.1064 | | $\Psi_{8}^{\overline{11}}$ | 0.0865 |
| | $\Psi_{9,9}^{10,\overline{12}}$ | 0.0937 | | $\Psi_{9}^{\overline{12}}$ | 0.0763 |
| E3-[3] [§]  | $\Psi_{8}^{\overline{10}}$ | 0.9877 | G3-[3] [§] | $\Psi_{9}^{\overline{10}}$ | 0.9929 |
| | Ψ_0 | 0.0916 | | $\Psi_{9,8,8}^{\overline{10},\overline{11},11}$ | 0.0661 |
| | $\Psi_{9,8,9}^{\overline{10},\overline{12},12}$ | 0.0657 | | $\Psi_{9,8,9}^{10,\overline{11},\overline{12}}$ | 0.0502 |

The values of the CI coefficients in the S_0 and S_1 states in Table 3.3 show the dependence of the electronic configurations on the C–O distance. As in the case of the O–H dissociation, the electronic configuration inversion occurs in the S_0 state when structure G3-[1]^{*} is transformed into structures G3-[2][†] and G3-[3][§] (the [CH₃][·] and [OH][·] products). On the S_0 potential energy curve, the contribution of the electronic ground state Ψ_0 is gradually decreased from $C_0 = 0.9830$ for structure G3-[1]^{*} to $C_0 = 0.9781$ for structure G3-[2][†]. Meanwhile, the contributions of the singly excited states associated with the excitation of an electron out of the lone-pair natural orbital ($\Psi_9^{\overline{12}}$ and $\Psi_9^{\overline{10}}$) are increased from $C_9^{\overline{12}} = 0.0724$ for structure G3-[1]^{*} to $C_9^{\overline{12}} = 0.0763$ for structure G3-[2][†] and to $C_9^{\overline{10}} = 0.9929$ for the C–O dissociated structure G3-[3][§]. The electronic configuration inversion $\Psi_0 \rightarrow \Psi_9^{\overline{10}}$ in the S_0 state leads to a substantial increase in the total energy and eventually to the intersection of the S_0 and S_1 states at long C–O distances. This finding explains why the C–O dissociation in the S_0 state requires rather high energy ($\Delta E^\ddagger = 405$ kJ/mol).

In the S_1 state, while the singly excited configuration $\Psi_9^{\overline{10}}$ dominates for the vertically excited and transition structures, structures E3-[1]^{*} and E3-[2][†] with $C_9^{\overline{10}} = 0.9849$ and 0.9803 , respectively, the contribution of the electronic configuration associated with the excitation of an electron out of the HOMO-1 natural orbital ($\Psi_8^{\overline{10}}$) is outstanding for the C–O dissociated structure, structure E3-[3][§] with $C_8^{\overline{10}} = 0.9877$. Although in the S_1 state the electronic configuration inversion occurs between the singly excited configurations $\Psi_9^{\overline{10}} \rightarrow \Psi_8^{\overline{10}}$, the relaxation of structure E3-[2][†] into structure E3-[3][§] is with barrierless energy. This is because the lone-pair natural

orbitals of the oxygen atom ($n_{\text{orb}} = 8$ and 9) in the dissociated structure E3-[3][§] are approximately degenerate. Therefore, the electronic configuration inversion in this case does not lead to an increase in the total energy on the S_1 potential energy curve.

3.4 The C–H dissociation

Although previous theoretical and experimental studies suggested that channel (2) is not important (Buenker, Olbrich, Schuchmann, Schuermann and Sonntag, 1984; Kassab, Gleghorn and Evleth, 1983), to search for a possibility for the unimolecular C–H dissociation, the S_1 potential energy curve with respect to the C–H distance was tentatively constructed by suppressing the O–H dissociation ($R_{\text{O}(5)\text{--H}(6)} = 0.97 \text{ \AA}$). The outstanding features of the S_1 potential energy curve in Figure 3.3 are the existence of a minimum at $R_{\text{C}(1)\text{--H}(4)} = 1.10 \text{ \AA}$ (structure E2-[1]^{*}) and a transition structure, in which the C–H bond breaks at $R_{\text{C}(1)\text{--H}(4)} = 1.50 \text{ \AA}$ (structure E2-[2][†]) with an energy barrier of $\Delta E^\ddagger = 146 \text{ kJ/mol}$; the value of ΔE^\ddagger is the same as that obtained from *ab initio* MRD-CI calculations (Buenker, Olbrich, Schuchmann, Schuermann and Sonntag, 1984).

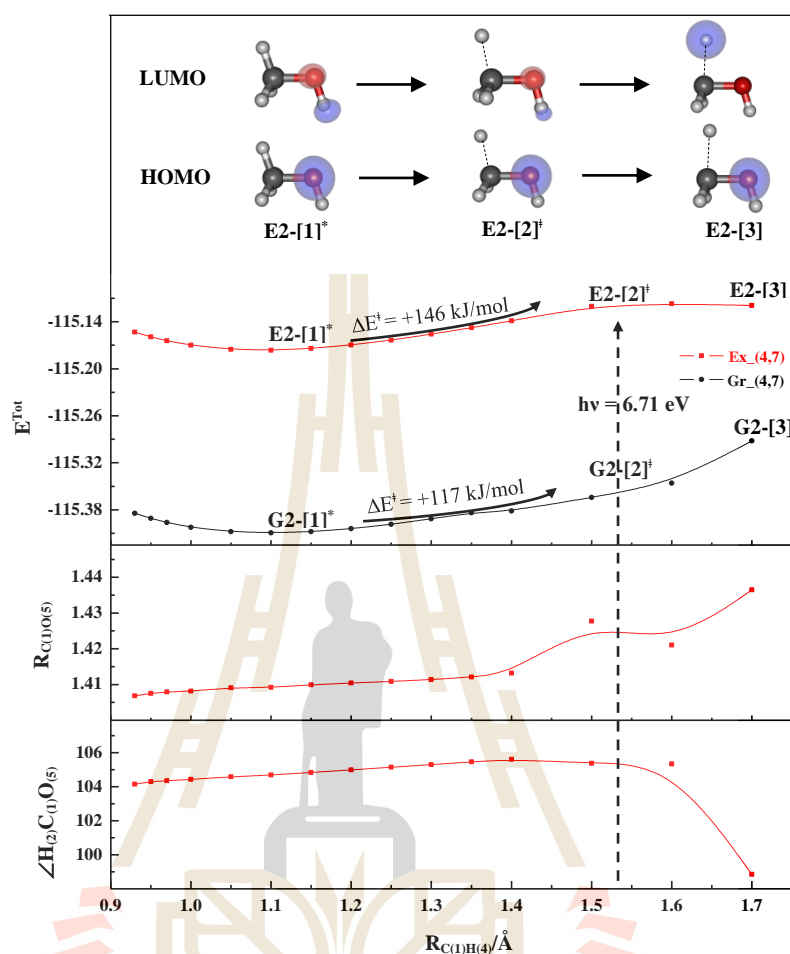


Figure 3.3 The relax-scan potential energy curves with respect to the C–H coordinates obtained from CASPT2 calculations. The energies, distances and angles are in au, Å and degrees, respectively. The values of the HOMO and LUMO isosurfaces are 0.11. ΔE^{Rel} = energy release; ΔE^{\ddagger} = energy barrier; \ddagger = transition structure; \S = structure at the intersection of the S_0 and S_1 potential energy curves; Gr_(4,7) and Ex_(4,7) = total energies obtained from CASPT2(4,7) calculations in the S_0 and S_1 states, respectively; and Gr_(16,12) and Ex_(16,12) = total energies obtained from CASPT2(16,12) calculations in the S_0 and S_1 states, respectively.

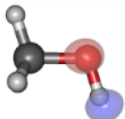
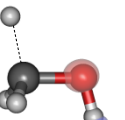
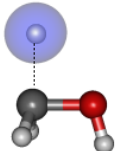
Although in the S_0 state the Boltzmann distribution and the kinetic energy release in channel (1) (-155 kJ/mol) suggest that 32% of structure G1-[1] could be thermally excited to structure G2-[2][‡] ($\Delta E^\ddagger = 117$ kJ/mol), the unimolecular C–H dissociation into the $[\text{CH}_2\text{OH}]^\cdot$ and $[\text{H}]^\cdot$ products in their respective ground states via the $S_0 \rightarrow S_1$ vertical excitation of structure G2-[2][‡] seems to not be feasible due to the lack of the intersection of the S_0 and S_1 potential energy curves at long C–H distances. To confirm this, CASPT2(4,7) geometry optimizations without geometry constraints were performed on structure E2-[2][‡] starting from $R_{\text{C}(1)\text{-H}(4)} = 1.55$ Å. It appeared that structure E2-[2][‡] relaxed on the O–H dissociation path resulting in structure E1-[3][§]. This finding is in line with the reported experimental and theoretical studies (Buenker, Olbrich, Schuchmann, Schuermann and Sonntag, 1984; Kassab, Gleghorn and Evleth, 1983), which suggested that $[\text{CH}_2\text{OH}]^\cdot$ is preferentially formed from a bimolecular reaction, e.g., $[\text{CH}_3\text{O}]^\cdot$ and CH_3OH (Takezaki and Takeuch, 1954), or the isomerization of $[\text{CH}_3\text{O}]^\cdot$ in the presence of catalysts (Sarkar, Mallick, Deepak, Kumar and Bandyopadhyay, 2017).

The analysis of the electronic configurations in Table 3.4 shows different trends of the CI coefficients as a function of the C–H coordinate compared with those of the O–H and C–O dissociations. In this case, the leading CI coefficients do not significantly change upon the C–H dissociation in the S_0 and S_1 states characterized by Ψ_0 and $\Psi_9^{\overline{10}}$, respectively. In the S_0 state, C_0 decreases gradually from 0.9830 for structure G2-[1] to 0.9753 for structure G2-[2][‡] and to 0.9553 for the C–H dissociated structure G2-[3], and in the S_1 state, $C_9^{\overline{10}}$ decreases from 0.9850 for structure E2-[1]^{*}

to 0.9758 for structure E2-[2][‡] and to 0.9669 for the C–H dissociated structure E2-[3]. The lack of electronic configuration inversion, especially in the S_0 state, makes the intersection of the S_0 and S_1 potential energy curves at long C–H distances unlikely and confirms that the unimolecular photodissociation of the C–H bond of CH_3OH into $[\text{CH}_2\text{OH}]^\cdot$ and $[\text{H}]^\cdot$ in their respective ground states is not feasible in the S_1 state.



Table 3.4 Characteristic structures of CH₃OH on the S₀ and S₁ potential energy curves for the C–H dissociation. The electronic configurations and CI coefficients were obtained from CASPT2(4,7) calculations in the S₀ and S₁ states. The values of the LUMO isosurfaces are 0.11.

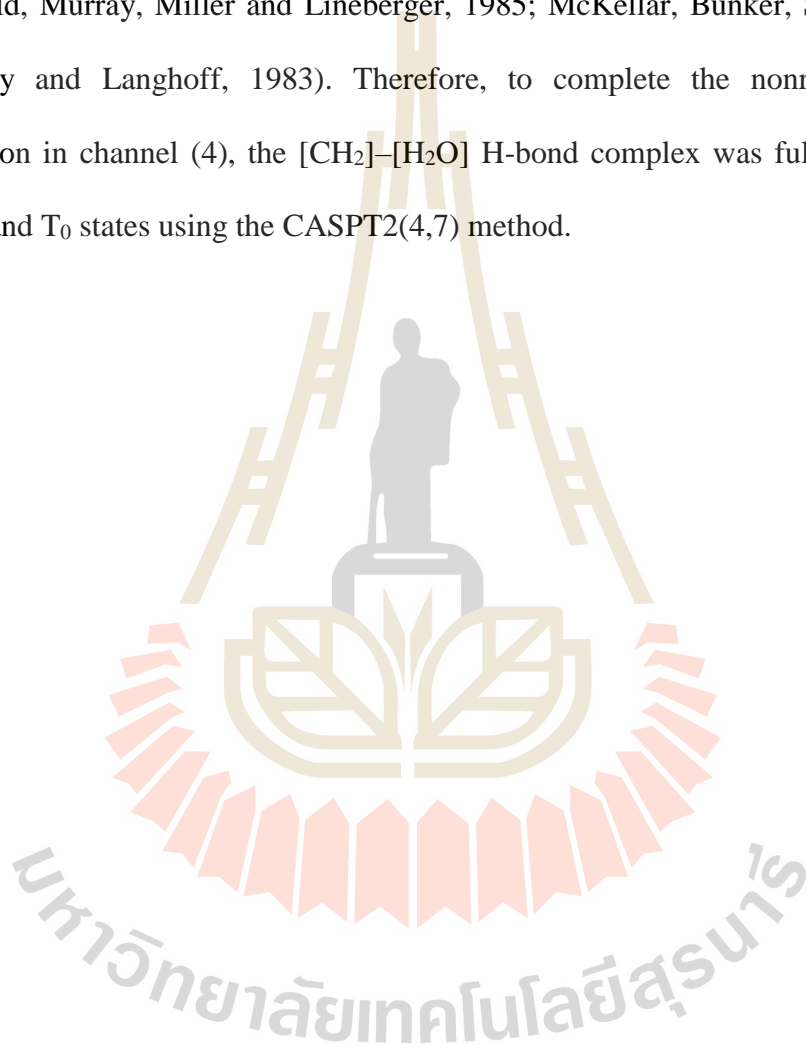
| Structure | S ₁ | | Structure | S ₀ | |
|--|--|-----------|---------------------|--|-----------|
| | Conf. | CI Coeff. | | Conf. | CI Coeff. |
| E2-[1] [*]  | $\Psi_9^{\overline{10}}$ | 0.9850 | G2-[1] [*] | Ψ_0 | 0.9830 |
| | $\Psi_{9,9}^{\overline{10},\overline{12}}$ | 0.0899 | | $\Psi_9^{\overline{12}}$ | 0.0722 |
| | $\Psi_{9,8,8}^{\overline{10},\overline{11},\overline{11}}$ | 0.0715 | | $\Psi_{8,8}^{\overline{11},\overline{11}}$ | 0.0698 |
| E2-[2] [†]  | $\Psi_9^{\overline{10}}$ | 0.9758 | G2-[2] [†] | Ψ_0 | 0.9753 |
| | $\Psi_{9,8,8}^{\overline{10},\overline{11},\overline{11}}$ | 0.1691 | | $\Psi_{8,8}^{\overline{11},\overline{11}}$ | 0.1682 |
| | $\Psi_{9,9}^{\overline{12},\overline{12}}$ | 0.1196 | | $\Psi_9^{\overline{12}}$ | 0.0917 |
| E2-[3]  | $\Psi_9^{\overline{10}}$ | 0.9669 | G2-[3] | Ψ_0 | 0.9553 |
| | $\Psi_{9,9}^{\overline{10},\overline{12}}$ | 0.1160 | | $\Psi_{8,8}^{\overline{10},\overline{10}}$ | 0.1919 |
| | $\Psi_{9,8,8}^{\overline{10},\overline{11},\overline{11}}$ | 0.0936 | | $\Psi_{8,8}^{\overline{11},\overline{10}}$ | 0.1445 |

3.5 Isomerization-mediated C–O dissociation

Although previous studies (Sarkar, Mallick, Deepak, Kumar and Bandyopadhyay, 2017; Buszek, Sinha and Francisco, 2011) anticipated that the formation of $[\text{CH}_2]$ and $[\text{H}_2\text{O}]$ in the S_1 state occurs through bimolecular reactions and the intramolecular isomerization in $[\text{CH}_3\text{O}]^\cdot$ is enhanced by catalysts, a possibility for $[\text{CH}_3\text{OH}] \rightarrow [\text{CH}_2\text{OH}_2]$ isomerization in a single isolated molecule is of interest in this work. To study the formation of $[\text{CH}_2]$ and $[\text{H}_2\text{O}]$ in channel (4), an isomerization-mediated C–O dissociation potential energy curve was constructed by constraining the O–H distance at $R_{\text{O-H}} = 0.97 \text{ \AA}$. The $[\text{CH}_3\text{OH}] \rightarrow [\text{CH}_2\text{OH}_2]$ isomerization was simulated by transferring one of the H atoms ($\text{H}_{(4)}$) from the CH_3 group to the OH group. The S_1 potential energy curve with respect to the $\text{H}_{(4)}\text{--O}_{(5)}$ coordinate in Figure 3.4 reveals that the intramolecular isomerization initially leads to the transition structure E4-[2][‡] with $R_{\text{H}_{(4)}\text{--O}_{(5)}} = 1.60 \text{ \AA}$ and $\Delta E^\ddagger = 92 \text{ kJ/mol}$, and it is followed by the homolytic cleavage of the C–O bond and formation of the $[\text{CH}_3]^\cdot\text{--}[\text{OH}]^\cdot$ H-bond structure, structure E4-[3] with $R_{\text{H}_{(4)}\text{--O}_{(5)}} = 1.58 \text{ \AA}$, $R_{\text{C}_{(1)}\text{--O}_{(5)}} = 2.64 \text{ \AA}$, and $E^{\text{Ex}} = 0.64 \text{ eV}$ (62 kJ/mol).

As in the case of the C–O dissociation in channel (3), to confirm that structure E4-[2][‡] is the transition structure for the $[\text{CH}_3\text{OH}] \rightarrow [\text{CH}_2\text{OH}_2]$ isomerization, CASPT2(4,7) geometry optimizations without geometry constraints were performed on structure E4-[2][‡] with $R_{\text{H}_{(4)}\text{--O}_{(5)}}$ slightly shifted. Similar results were observed, namely, starting from structure E4-[2][‡] with $R_{\text{H}_{(4)}\text{--O}_{(5)}} = 1.65 \text{ \AA}$, CASPT2(4,7) geometrical optimizations yielded structure E1-[3][§] (the O–H dissociated structure), whereas starting from structure E4-[2][‡] with $R_{\text{H}_{(4)}\text{--O}_{(5)}} = 1.58 \text{ \AA}$, the C–O dissociation

and intermolecular proton transfer from $[\text{CH}_3]'$ to $[\text{OH}]'$ generate the $[\text{CH}_2]\text{--}[\text{H}_2\text{O}]$ H-bond complex in the S_1 state, structure E4-[4] in Figure 3.5 with $E^{\text{Ex}} = 0.28$ eV (26 kJ/mol), $R_{\text{C}(1)\text{--}\text{O}(5)} = 3.26$ and $R_{\text{C}(1)\text{--}\text{H}(4)} = 2.30$ Å. It should be noted that in the electronic ground state, $^3[\text{CH}_2]$ (the T_0 state) is more stable than $^1[\text{CH}_2]$ (the S_0 state) (Leopold, Murray, Miller and Lineberger, 1985; McKellar, Bunker, Sears, Evenson, Saykally and Langhoff, 1983). Therefore, to complete the nonradiative $S_1 \rightarrow T_0$ relaxation in channel (4), the $[\text{CH}_2]\text{--}[\text{H}_2\text{O}]$ H-bond complex was fully optimized in the S_0 and T_0 states using the CASPT2(4,7) method.



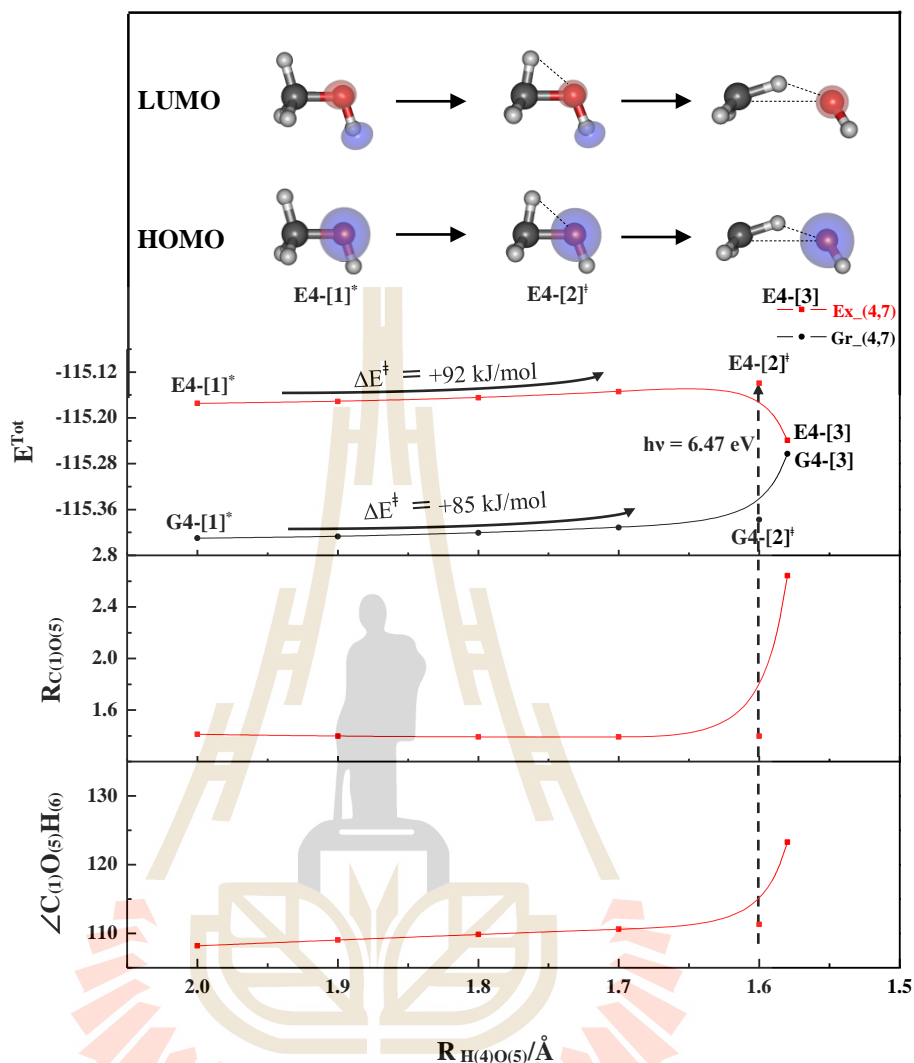


Figure 3.4 The relax-scan potential energy curves for the $[\text{CH}_3\text{OH}] \rightarrow [\text{CH}_2\text{OH}_2]$ isomerization obtained from CASPT2(4,7) calculations by transferring the $\text{H}_{(4)}$ atom from the CH_3 group to the OH group.

The results in Figure 3.5 reveal that the C–H distances and the $\angle\text{HCH}$ angles in the optimized structures $\text{G4-}[5]$ and ${}^3\text{G4-}[5]$ are in excellent agreement with the experimental values (Bunker and Jensen, 1983; Jensen, Bunker and Hoy, 1982), but the H-bond distances are systematically shorter than those obtained from the

CCSD(T)-F12/aug-cc-pVDZ//B3LYP-D3/aug-cc-pVTZ method (Standard, 2016), especially in the S_0 state, where $\Delta R_{C(1)-O(5)} = 0.16 \text{ \AA}$ (Standard, 2016). The H-bond interaction energies (ΔE^{HB}) of structures G4-[5] and ${}^3\text{G4}$ -[5] are -33.0 and -5.5 kJ/mol, respectively, with a singlet-triplet energy gap of $\Delta E^{\text{ST}} = 30 \text{ kJ/mol}$. The values of ΔE^{HB} are lower, whereas ΔE^{ST} is higher than those obtained from CCSD(T)-F12/aug-cc-pVDZ//B3LYP-D3/aug-cc-pVTZ calculations (Standard, 2016). E^{HB} values in the S_0 and T_0 states are -13.9 and -2.3 kJ/mol, respectively and $\Delta E^{\text{ST}} = 27.4 \text{ kJ/mol}$. The discrepancies are partly because the reported ΔE^{HB} and ΔE^{ST} (Standard, 2016) were obtained based on single-point single-reference CCSD(T)-F12 calculations using the equilibrium structures obtained from the B3LYP-D3/aug-cc-pVTZ geometry optimizations. In addition, the analysis of the CI coefficients in Figure 3.5 suggests that the neglect of the multiconfigurational character of the wave functions could also lead to the discrepancies in ΔE^{HB} and ΔE^{ST} , especially in the S_0 state (Standard, 2016). For structure G4-[5], the doubly excited configuration ($\Psi_{9,9}^{\overline{10},10}$), which is characteristic of the singlet carbene (${}^1[\text{CH}_2]$), contributes approximately 15% of the closed-shell electronic ground-state configuration Ψ_0 .

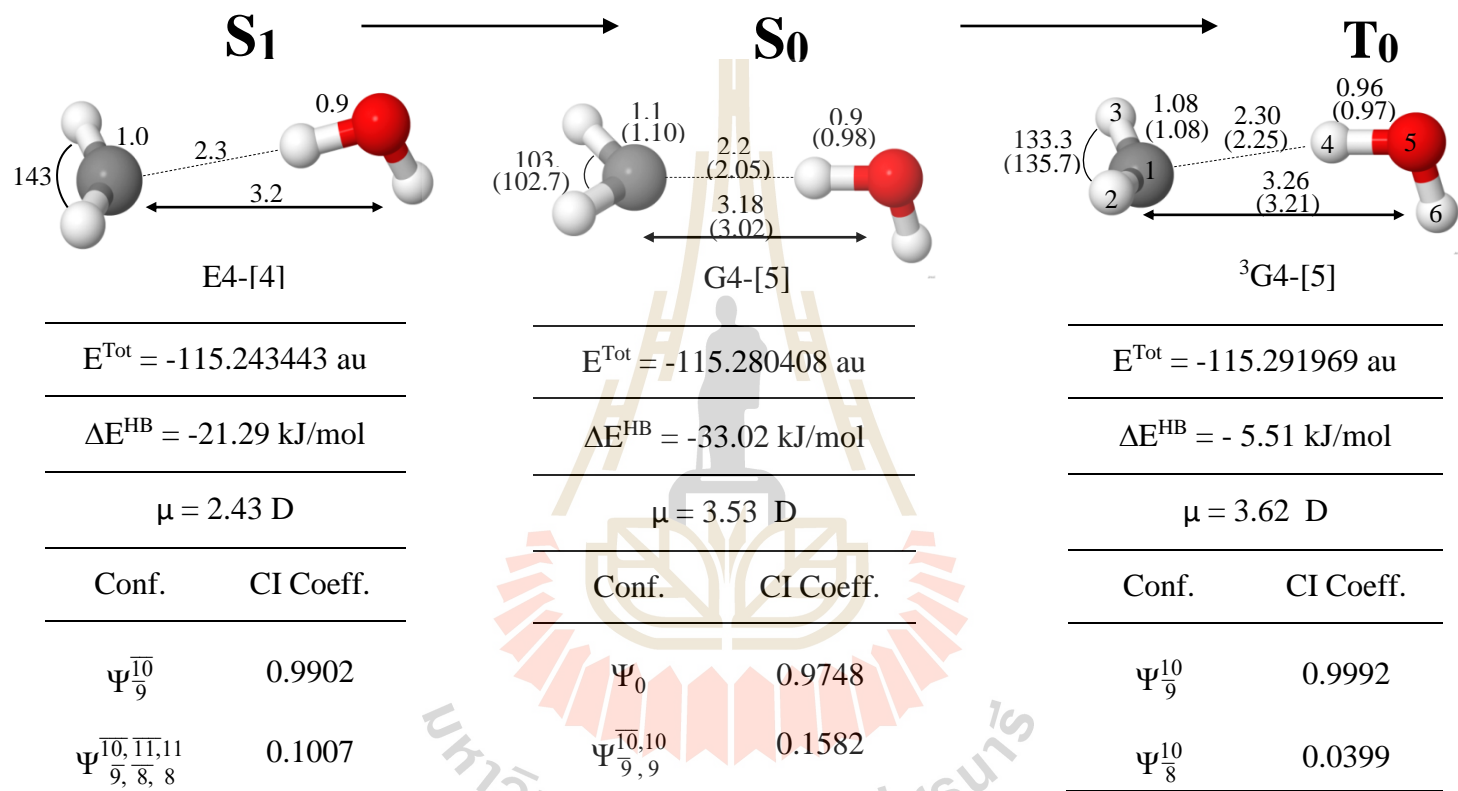


Figure 3.5 Equilibrium structures of the [CH₂]-[H₂O] H-bond complexes in the S₀ and T₀ states, obtained from CASPT2(4,7) calculations. The values in parentheses are the results reported by Standard (Standard, 2016). The energies, distances and angles

are in au, Å and degrees, respectively. The values of the HOMO and LUMO isosurfaces are 0.11. ΔE^{Rel} = energy release; ΔE^\ddagger = energy barrier; ‡ = transition structure; and $\text{Gr}_{(4,7)}$ and $\text{Ex}_{(4,7)}$ = total energies obtained from CASPT2(4,7) calculations in the S_0 and S_1 states, respectively.



These results and the fact that the S_1 potential energy curve in Figure 3.4 was computed by constraining the O–H distance at $R_{O-H} = 0.97 \text{ \AA}$ lead to the conclusion that the intramolecular isomerization-mediated C–O dissociation in channel (4) can occur when the equilibrium structure in the electronic ground state (structure G1-[1]) is thermally excited to structure G4-[2][‡] ($\Delta E^\ddagger = 85 \text{ kJ/mol}$); the kinetic energy release in channel (1) could initiate the $[\text{CH}_3\text{OH}] \rightarrow [\text{CH}_2\text{OH}_2]$ isomerization by exciting 37% of structure G1-[1] to structure G4-[2][‡]. Then, structure G4-[2][‡] is $S_0 \rightarrow S_1$ vertically excited ($E^{\text{Ex}} = 6.47 \text{ eV}$ or 192 nm) to the transition structure E4-[2][‡], which is transformed into the $[\text{CH}_2]\text{--}[\text{H}_2\text{O}]$ H-bond complex in the S_1 state (structure E4-[4] in Figure 3.5). Due to that the energy gap of the total energies of structures E4-[4] and G4-[4] is only 26.0 kJ/mol and that between structures G4-[4] and ${}^3\text{G4-[5]}$ is -101 kJ/mol , the nonradiative relaxation of structure E4-[4] to structure ${}^3\text{G4-[5]}$, which includes the $S_0 \rightarrow T_0$ intersystem crossing between structures G4-[5] and ${}^3\text{G4-[5]}$ through a collision ($\Delta E^{\text{ST}} = 30 \text{ kJ/mol}$), is an exothermic process with $\Delta E^{\text{Rel}} \approx -127 \text{ kJ/mol}$. The trends of the CI coefficients in Table 3.5 confirm the role played by the electronic configuration inversion. In the S_0 state, the electronic configuration inversion $\Psi_0 \rightarrow \Psi_8^{\text{T0}}$ increases the total energy on the $[\text{CH}_3\text{OH}] \rightarrow [\text{CH}_2\text{OH}_2]$ isomerization potential energy curve, structure G4-[2][‡] to G4-[3], leading to a decrease in the energy gap between the S_0 and S_1 states. The energy gap between structures E4-[3] and G4-[3] is 62 kJ/mol , and the threshold distance for the electronic configuration inversion $R_{\text{H(4)-O(5)}} = 1.60 \text{ \AA}$.

Although both channels (3) and (4) involve C–O bond cleavage, the CI coefficients in Table 3.3 and Figure 3.5 reveal different characteristic electronic states of the products. In channel (3), structure G3-[3][§] is dominated by the singly excited state $\Psi_9^{\overline{10}}$ with $C_9^{\overline{10}} = 0.9929$, confirming that the homolytic cleavage of the C–O bond leads to the $[\text{CH}_3]'$ and $[\text{OH}]'$ radicals, represented by one outstanding S-type configuration with two open shells ($\Psi_9^{\overline{10}}$). In channel (4), the $^1[\text{CH}_2]\text{--}[\text{H}_2\text{O}]$ H-bond complex (structure G4-[5]) is characterized by the electronic ground state Ψ_0 with $C_0 = 0.9748$ and a small contribution of the electronic configuration of the singlet methylene, the doubly excited state $\Psi_{9,9}^{\overline{10},10}$ with $C_{9,9}^{\overline{10},10} = 0.1582$, whereas the $^3[\text{CH}_2]\text{--}[\text{H}_2\text{O}]$ H-bond complex (structure $^3\text{G4-[5]}$) is characterized by the open-shell configuration Ψ_9^{10} with $C_9^{10} = 0.9992$, which is characteristic of the triplet methylene.

Table 3.5 Characteristic structures of CH₃OH on the S₀ and S₁ potential energy curves for the intramolecular [CH₃OH]→[CH₂OH₂] isomerization. The main electronic configurations and CI coefficients were obtained from CASPT2(4,7) calculations in the S₀ and S₁ states.

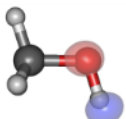

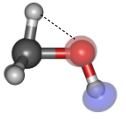

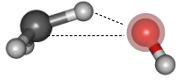

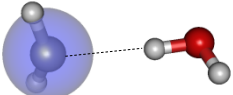
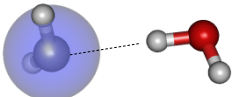
| Structure | S ₁ | | Structure | S ₀ | |
|--|---|-----------|---|---------------------------------|-----------|
| | Conf. | CI Coeff. | | Conf. | CI Coeff. |
| E4-[1]*  | $\Psi_9^{\overline{10}}$ | 0.9850 | G4-[1]*  | Ψ_0 | 0.9830 |
| | $\Psi_{9,9}^{10,\overline{12}}$ | 0.0898 | | $\Psi_9^{\overline{12}}$ | 0.0721 |
| | $\Psi_{9,8,8}^{\overline{10},\overline{11},11}$ | 0.0716 | | $\Psi_{8,8}^{\overline{11},11}$ | 0.0699 |
| E4-[2]†  | $\Psi_9^{\overline{10}}$ | 0.9858 | G4-[2]†  | Ψ_0 | 0.9859 |
| | $\Psi_{9,9}^{10,\overline{11}}$ | 0.1220 | | $\Psi_9^{\overline{11}}$ | 0.0936 |
| | $\Psi_{9,8,8}^{\overline{10},\overline{12},12}$ | 0.0878 | | $\Psi_{8,8}^{\overline{12},12}$ | 0.0878 |
| E4-[3]  | $\Psi_9^{\overline{10}}$ | 0.9494 | G4-[3]  | $\Psi_8^{\overline{10}}$ | 0.6630 |
| | $\Psi_{9,8}^{\overline{10},10}$ | 0.2928 | | Ψ_0 | 0.6473 |
| | $\Psi_{9,8,8}^{\overline{10},\overline{12},12}$ | 0.0583 | | $\Psi_{8,8}^{\overline{10},10}$ | 0.3564 |

Table 3.5 (Continued) Characteristic structures of CH₃OH on the S₀ and S₁ potential energy curves for the intramolecular [CH₃OH]→[CH₂OH₂] isomerization. The main electronic configurations and CI coefficients were obtained from CASPT2(4,7) calculations in the S₀ and S₁ states.

| Structure | S ₁ | | Structure | S ₀ | |
|--|--|-----------|---------------------|--|-----------|
| | Conf. | CI Coeff. | | Conf. | CI Coeff. |
| E4-[4]  | $\Psi_{9}^{\overline{10}}$ | 0.9902 | G4-[4] | Ψ_0 | 0.9452 |
| | $\Psi_{9,8,8}^{\overline{10},\overline{11},\overline{11}}$ | 0.1007 | | $\Psi_{9,9}^{\overline{10},\overline{10}}$ | 0.2912 |
| | - | - | | $\Psi_{8,8}^{\overline{11},\overline{11}}$ | 0.0962 |
| ³ E4-[5]  | Ψ_{8}^{10} | 0.9992 | ³ G4-[5] | Ψ_{9}^{10} | 0.9992 |
| | Ψ_{9}^{10} | 0.0399 | | Ψ_{8}^{10} | 0.0399 |
| | - | - | | - | - |

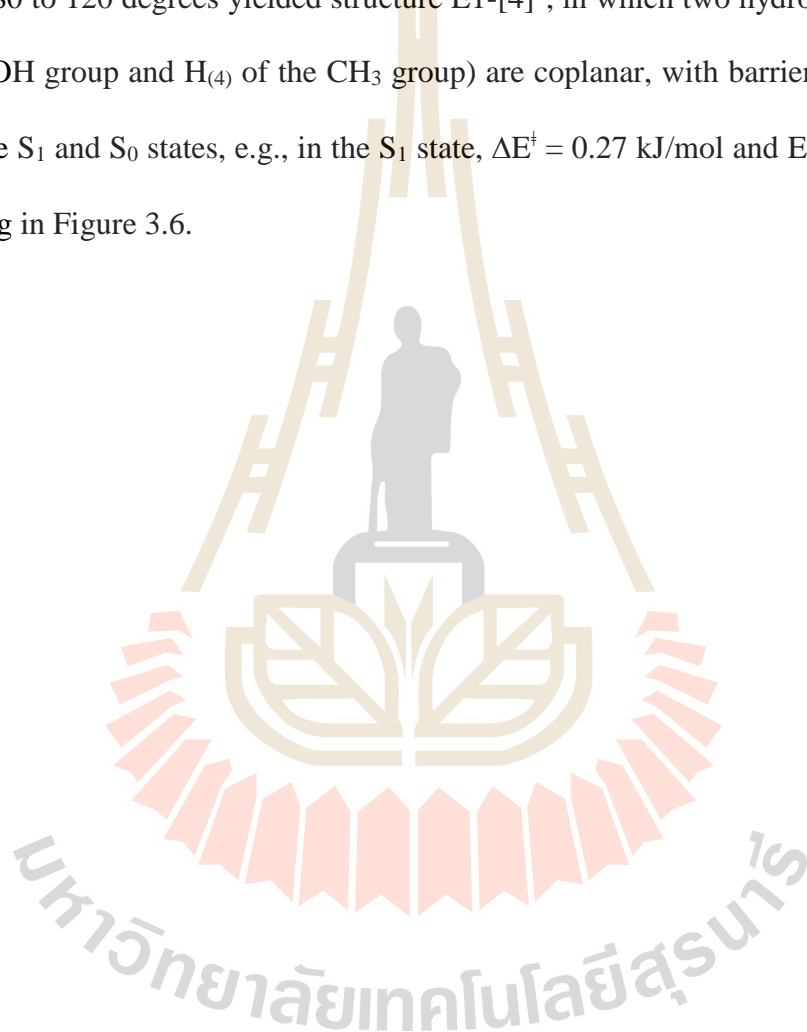
มหาวิทยาลัยเทคโนโลยีสุรนารี

3.6 Rotational-mediated C–H dissociation

Formaldehyde could be formed from various radical reactions, e.g., the bimolecular reaction between $[\text{CH}_2\text{OH}]^\cdot$ or $[\text{CH}_3\text{O}]^\cdot$ and O_2 (Ravishankara, 1988), as well as the C–H dissociation of $[\text{CH}_3\text{O}]^\cdot$ (Porter and Noyes, 1959). In this work, we are interested in the possibility of generating formaldehyde directly from single-isolated CH_3OH . Although the freeze-scan potential energy curve in the lowest singlet-excited state obtained from *ab initio* MRD-CI calculations (Buenker, Olbrich, Schuchmann, Schuermann and Sonntag, 1984) showed a low energy barrier for the H_2 elimination (approximately 52 kJ/mol), the S_0 and S_1 potential energy curves for the dehydrogenation do not intersect at large CH_2O and H_2 separations, and thus, the high percentage of CH_2O and H_2 in their respective electronic ground states observed in the experiment cannot be explained. The energy gap between the S_0 and S_1 states at $R = 3 \text{ \AA}$ amounts to 262 kJ/mol (Buenker, Olbrich, Schuchmann, Schuermann and Sonntag, 1984). The lack of the intersection of the S_0 and S_1 states implies that the CH_2O and H_2 products are still in the electronic excited state. This could be due to the freeze-scan method and the degrees of freedom chosen in the calculations of the S_0 and S_1 potential energy curves. The dehydrogenation was hypothesized by Buenker *et al.* (Buenker, Olbrich, Schuchmann, Schuermann and Sonntag, 1984) to occur through a concerted reaction, in which the hydrogen atom of the OH group and one hydrogen atom of the CH_3 group are coplanar and leave the CH_2O moiety at the same rate.

Based on the observation that the O–H dissociation is the most preferential process in the S_1 state and the anticipation that the H_2 elimination involves a two-step nonconcerted mechanism (Buenker, Olbrich, Schuchmann, Schuermann and Sonntag,

1984), formaldehyde was hypothesized in this work to form from the O–H dissociated structure E1-[3][‡]. To search for an appropriate precursor, the S₁ and S₀ potential energy curves with respect to the C–O rotation were constructed for structure E1-[3][‡]. Starting from structure E1-[3][‡], the variation of the dihedral angle ∠H₍₄₎C₍₁₎O₍₅₎H₍₆₎ from 180 to 120 degrees yielded structure E1-[4][‡], in which two hydrogen atoms (H₍₆₎ of the OH group and H₍₄₎ of the CH₃ group) are coplanar, with barrierless energies in both the S₁ and S₀ states, e.g., in the S₁ state, ΔE[‡] = 0.27 kJ/mol and E^{Ex} = 0.01 eV, as showing in Figure 3.6.



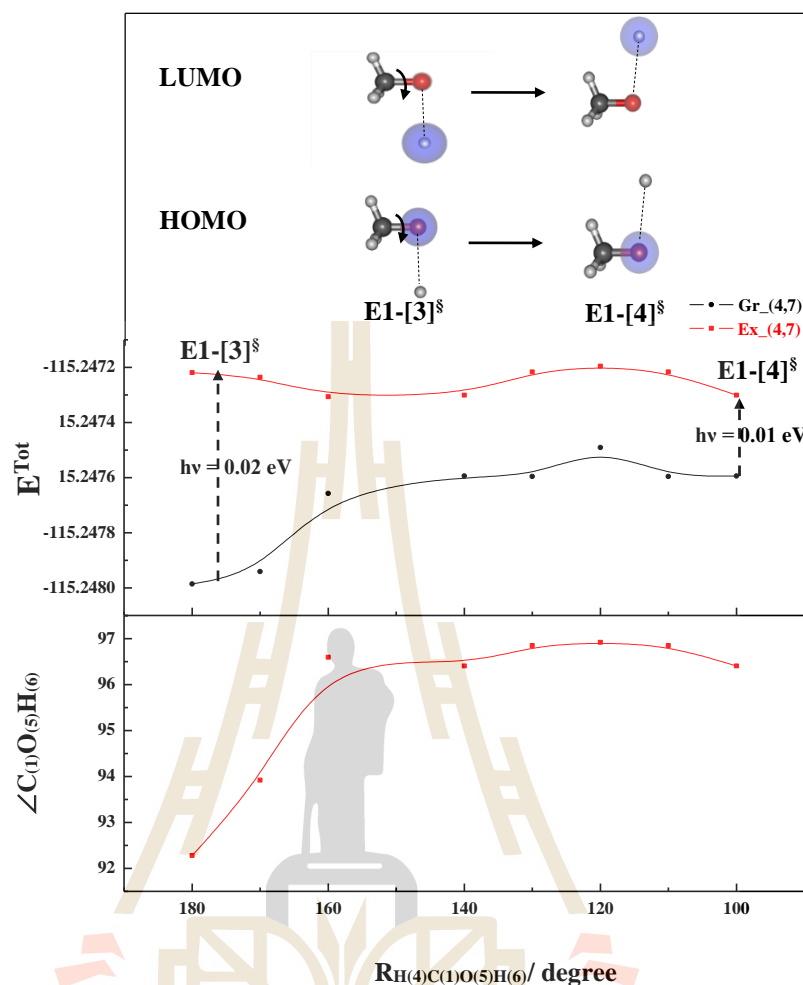
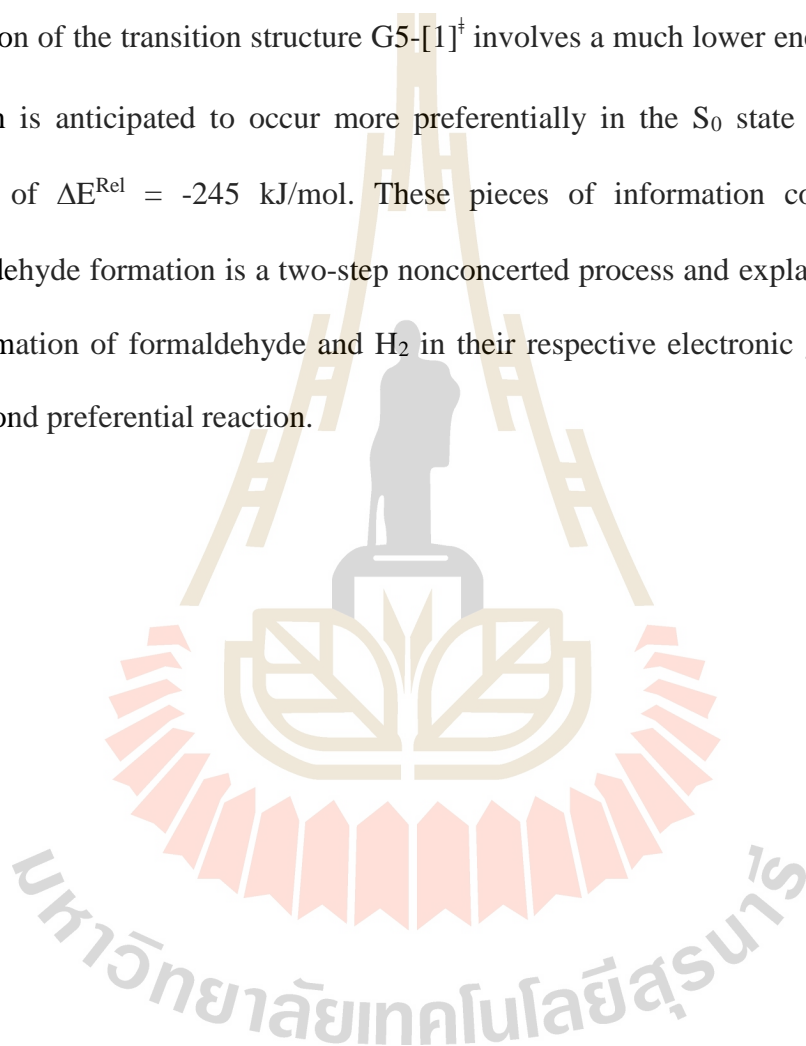


Figure 3.6 The relax-scan potential energy curves for the C–O rotation obtained from CASPT2(4,7) calculations. The energies, distances and angles are in au, Å and degrees, respectively. The values of the HOMO and LUMO isosurfaces are 0.11. [§] = structure at the intersection of the S_0 and S_1 potential energy curves; and Gr_(4,7) and Ex_(4,7) = total energies obtained from CASPT2(4,7) calculations in the S_0 and S_1 states, respectively.

Then, the S_1 and S_0 potential energy curves for the dehydrogenation were constructed from structure E1-[4][§] by variation of the $\text{H}_{(4)}\text{--}\text{H}_{(6)}$ distance from 2.66–0.73 Å. The S_0 and S_1 potential energy curves in Figure 3.7 suggest two possibilities

for formaldehyde formation through H_2 elimination, in the S_1 state through the transition structure E5-[2]^\ddagger with $\Delta E^\ddagger = 53$ kJ/mol or in the S_0 state through the transition structure G5-[1]^\ddagger with $\Delta E^\ddagger = 6.29$ kJ/mol. Since the precursor (structure $\text{E1-[4]}^{\text{§}}$) is energetically at the intersection of the S_1 and S_0 states ($E^{\text{Ex}} = 0.01$ eV) and the formation of the transition structure G5-[1]^\ddagger involves a much lower energy barrier, the reaction is anticipated to occur more preferentially in the S_0 state with an energy release of $\Delta E^{\text{Rel}} = -245$ kJ/mol. These pieces of information confirm that the formaldehyde formation is a two-step nonconcerted process and explain in detail why the formation of formaldehyde and H_2 in their respective electronic ground states is the second preferential reaction.



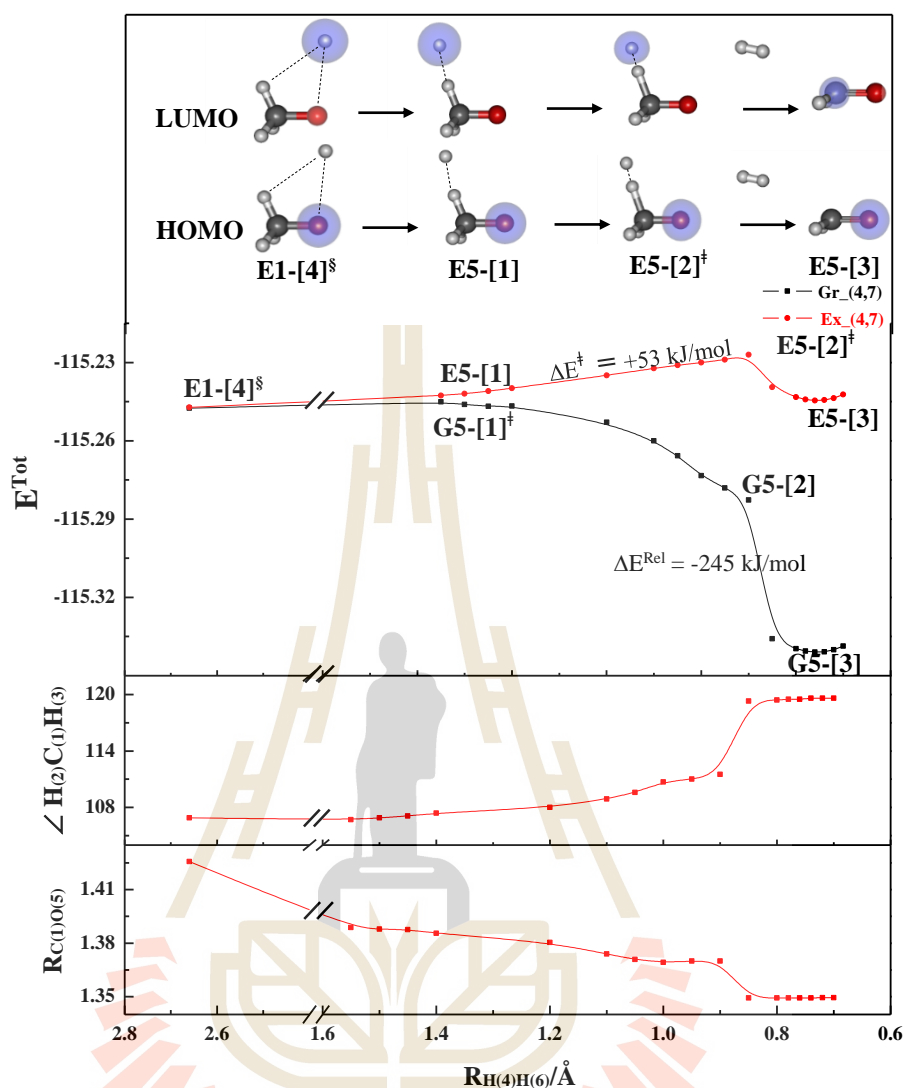
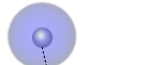
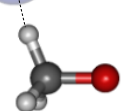

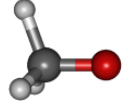

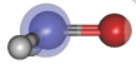


Figure 3.7 The relax-scan potential energy curves for formaldehyde formation from the O–H dissociated structure (structure E1-[4][§]) obtained from CASPT2(4,7) calculations. The energies, distances and angles are in au, Å and degrees, respectively. The values of the HOMO and LUMO isosurfaces are 0.11. ΔE^{Rel} = energy release; ΔE^{\ddagger} = energy barrier; \ddagger = transition structure; \S = structure at the intersection of the S_0 and S_1 potential energy curves; and Gr_(4,7) and Ex_(4,7) = total energies obtained from CASPT2(4,7) calculations in the S_0 and S_1 states, respectively.

Table 3.6 Characteristic structures of CH₃OH on the S₁ relax-scan potential energy curve for the elimination of H₂.

The electronic configurations and CI coefficients were obtained from CASPT2(4,7) calculations in the S₀ and S₁ states.

The values of the LUMO isosurfaces are 0.11.

| Structure | S ₁ | | Structure | S ₀ | | | |
|---------------------|---|--------------------------------------|-----------|---|--------------------------|---------------------------------|--------|
| | Conf. | CI Coeff. | | Conf. | CI Coeff. | | |
| E5-[1] |  | $\Psi_9^{\overline{10}}$ | 0.9712 |  | $\Psi_8^{\overline{10}}$ | 0.8594 | |
| | | $\Psi_{9,8}^{\overline{10,10}}$ | 0.1944 | | G5-[1] [†] | Ψ_0 | 0.4157 |
| | | $\Psi_8^{\overline{10}}$ | 0.0756 | | | $\Psi_{8,8}^{\overline{10,10}}$ | 0.2635 |
| E5-[2] [†] |  | $\Psi_9^{\overline{10}}$ | 0.9457 |  | Ψ_0 | 0.8963 | |
| | | $\Psi_{9,8}^{\overline{10,10}}$ | 0.3039 | | G5-[2] | $\Psi_8^{\overline{10}}$ | 0.3227 |
| | | $\Psi_{9,8,8}^{\overline{10,12,12}}$ | 0.0523 | | | $\Psi_{8,8}^{\overline{10,10}}$ | 0.2726 |
| E5-[3] |  | $\Psi_9^{\overline{10}}$ | 0.9569 |  | Ψ_0 | 0.9298 | |
| | | $\Psi_{9,8}^{\overline{10,10}}$ | 0.2675 | | G5-[3] | $\Psi_8^{\overline{10}}$ | 0.2551 |
| | | $\Psi_{9,8,8}^{\overline{10,12,12}}$ | 0.0472 | | | $\Psi_{8,8}^{\overline{10,10}}$ | 0.2285 |

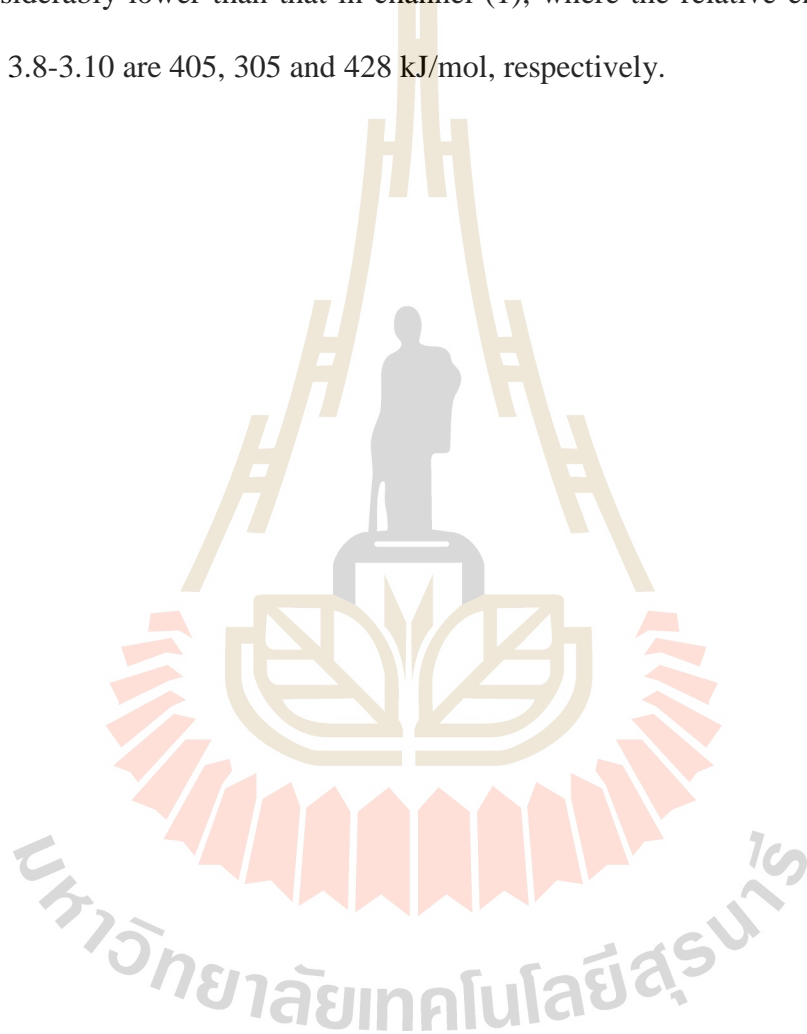
Analysis of the electronic configurations and CI coefficients of the structures on the S_0 and S_1 potential energy curves in Table 3.6 confirms the role played by the electronic configuration inversion. In this case, the transformation of structure E1-[4][§] into G5-[3] (the CH_2O and H_2 molecules) is more preferential on the S_0 potential energy curve because the electronic configuration inversion in this case involves the inversion of the singlet electronic state $\Psi_8^{\overline{10}}$ with a higher energy to the electronic ground state with a lower energy Ψ_0 .

3.7 The interplay between the thermal excitation and photoexcitation

Based on the discussion on the structures and energetics as well as the electronic configurations on the S_0 and S_1 potential energy curves, the photodissociation mechanisms of CH_3OH in the S_1 state are summarized in Figures 3.8-3.10. Since the $S_0 \rightarrow S_1$ vertical excitation energies (E^{Ex}) are approximately the same and because the thermally excited structures in the S_0 state are the precursors for the formations of the transition structures in the S_1 state as well as the products in their respective electronic ground states, one can conclude that the thermal excitation in the electronic ground state plays the most important role in determining the photodissociations in channels (3) and (4). Figures 3.8-3.10 illustrates that photons with approximately the same energy, 6.3–6.5 eV or 192–196 nm, can generate the transition structures for the photodissociations in channels (3) and (4). In other words, the photodissociation processes of CH_3OH in the S_1 state are thermally selective.

In addition, because the O–H dissociation is with barrierless energy and the formation of CH_2O and H_2 involves a very low energy barrier, the photodissociations

in channels (1) and (5) are kinetically controlled, whereas the photodissociations in channels (3) and (4) are thermodynamically controlled. The C–O dissociation and $[\text{CH}_3\text{OH}] \rightarrow [\text{CH}_2\text{OH}_2]$ isomerization require higher thermal energies to generate the precursors in the S_0 state, but the total energies of the products in channels (3) and (4) are considerably lower than that in channel (1), where the relative energies (E^{Rel}) in Figures 3.8-3.10 are 405, 305 and 428 kJ/mol, respectively.



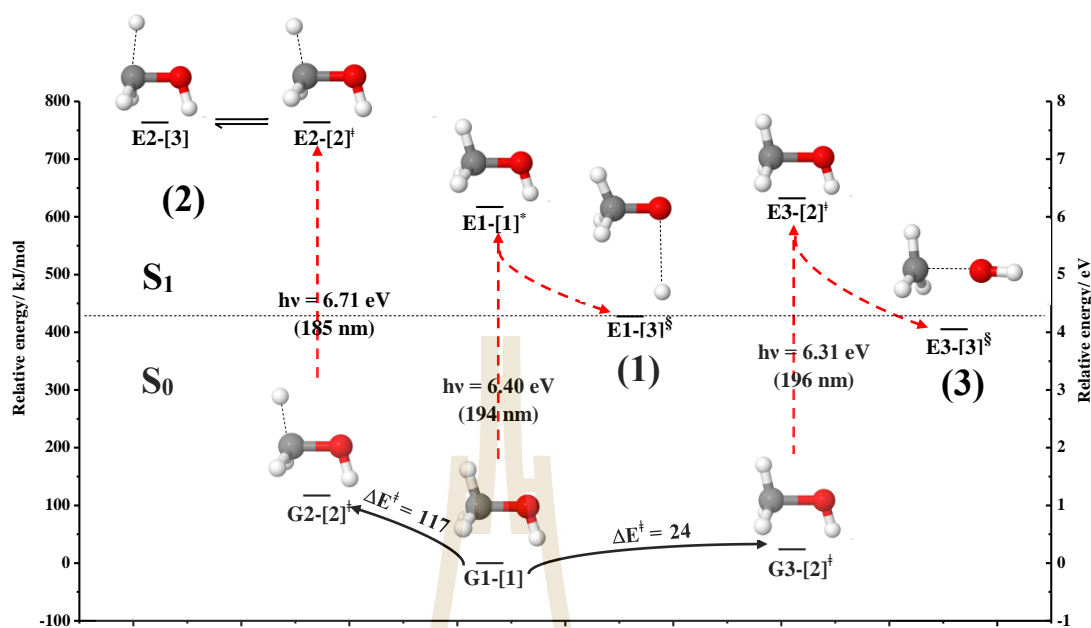


Figure 3.8 Mechanisms of the unimolecular photodissociations of CH₃OH obtained from the analysis of the S₀ and S₁ potential energy curves obtained from the CASPT2(4,7) method. The relative energies are with respect to structure G1-[1]. The energy releases (ΔE^{Rel}) and energy barriers (ΔE^\ddagger) are in kJ/mol. ‡ = transition structure and § = structure at the intersection of the S₀ and S₁ potential energy curves. a) Channels (1)-(3). b) Channel (4). c) Channel (5).

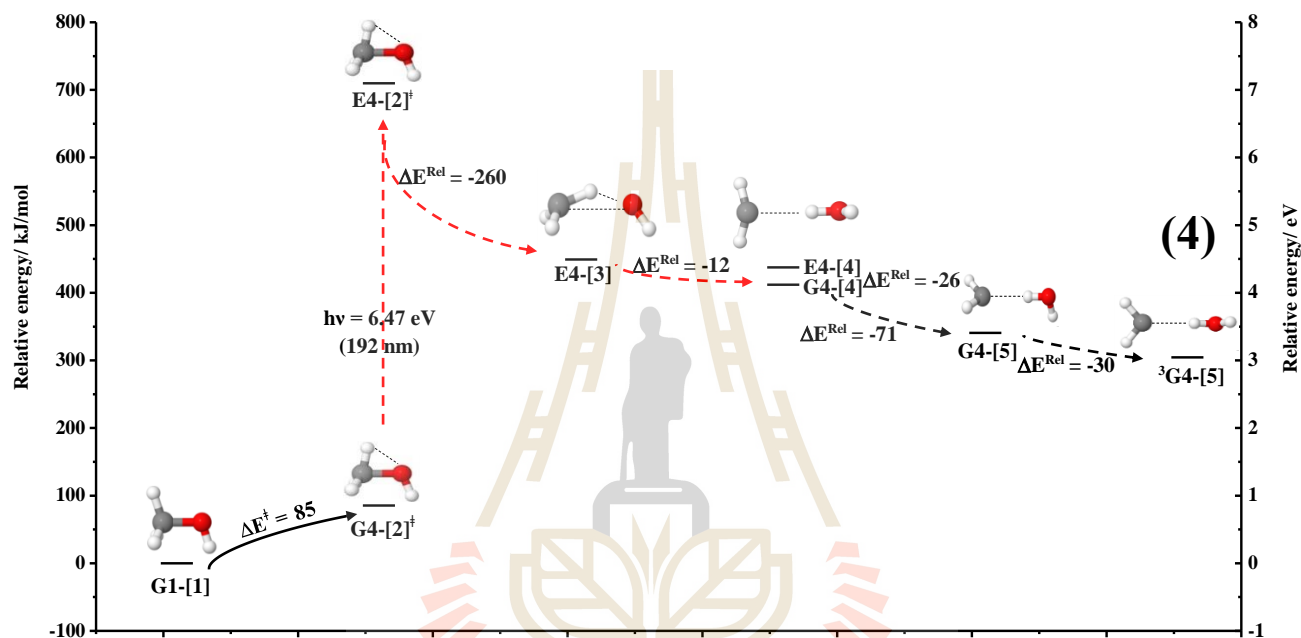


Figure 3.9 Mechanisms of the unimolecular photodissociations of CH_3OH obtained from the analysis of the S_0 and S_1 potential energy curves obtained from the CASPT2(4,7) method. The relative energies are with respect to structure G1-[1]. The energy releases (ΔE^{Rel}) and energy barriers (ΔE^\ddagger) are in kJ/mol. ‡ = transition structure and s = structure at the intersection of the S_0 and S_1 potential energy curves.

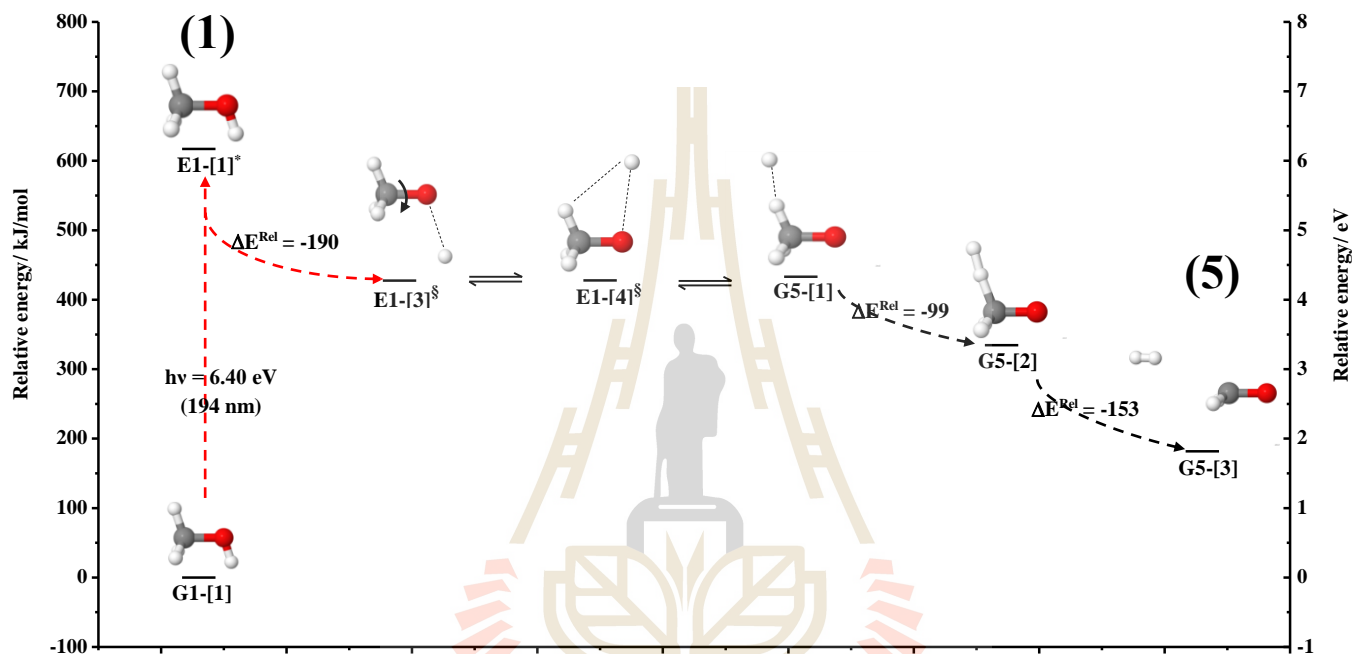


Figure 3.10 Mechanisms of the unimolecular photodissociations of CH₃OH obtained from the analysis of the S₀ and S₁ potential energy curves obtained from the CASPT2(4,7) method. The relative energies are with respect to structure G1-[1]. The energy releases (ΔE^{Rel}) and energy barriers (ΔE^{\ddagger}) are in kJ/mol. \ddagger = transition structure and \S = structure at the intersection of the S₀ and S₁ potential energy curves.

CHAPTER IV

CONCLUSION

In this work, the mechanisms of the photodissociations of single-isolated CH_3OH in the lowest singlet-excited (S_1) state were systematically studied using the CASPT2 method with the aug-cc-pVDZ basis set. The theoretical study considered single-photon photodissociations in the five proposed channels, with an emphasis on nonradiative relaxation that bring the $S_0 \rightarrow S_1$ vertically excited structures to the products in their respective electronic ground states and on the interplay between the thermal excitation and photoexcitation.

The S_1 relax-scan potential energy curves confirmed that the O–H dissociation is the predominant exothermic process, whereas the formation of the formaldehyde (CH_2O) and hydrogen (H_2) molecules is the second preferential process, in which the O–H dissociated species becomes the precursor in the S_0 state ($\Delta E^\ddagger = 6 \text{ kJ/mol}$). For the C–O dissociation, the relax-scan potential energy curves suggested a thermally excited precursor ($\Delta E^\ddagger = 24 \text{ kJ/mol}$) in the S_0 state, from which the $S_0 \rightarrow S_1$ vertical excitation leads to a transition structure and the formation of the $[\text{CH}_3]^\cdot$ and $[\text{OH}]^\cdot$ products in their respective electronic ground states. The CASPT2 results also revealed a possibility for the $[\text{CH}_3\text{OH}] \rightarrow [\text{CH}_2\text{OH}_2]$ isomerization dissociation, in which another thermally excited precursor ($\Delta E^\ddagger = 85 \text{ kJ/mol}$) is vertically excited to generate a transition structure in the S_1 state, from which the C–O dissociation

and intermolecular proton transfer from $[\text{CH}_3]^\cdot$ to $[\text{OH}]^\cdot$ leads to the $[\text{CH}_2]$ and $[\text{H}_2\text{O}]$ products. The O–H dissociation with barrierless energy and the formation of CH_2O and H_2 with a low energy barrier are kinetically controlled, whereas the C–O dissociation and $[\text{CH}_3\text{OH}] \rightarrow [\text{CH}_2\text{OH}_2]$ isomerization with higher energy barriers are thermodynamically controlled.

Analysis of the electronic configurations and CI coefficients suggested that the precursors and transition structures for the photodissociations are characterized by electronic configuration inversions in the S_0 state, which lead to the intersection of the S_0 and S_1 potential energy curves and the products in their respective electronic ground states, and the C–H dissociation, which generates $[\text{CH}_2\text{OH}]^\cdot$ and $[\text{H}]^\cdot$, is unlikely to be unimolecular because of the lack of the electronic configuration inversion and the intersection of the S_0 and S_1 potential energy curves. The present theoretical results revealed that photons with approximately the same energy can generate all of the products in their respective electronic ground states in channels (1) and (3)-(5), and they provide insights into the thermal selectivity and interplay between the thermal excitation and photoexcitation as well as the importance of the multiconfigurational characters in the covalent bond dissociation, which can be used as guidelines for further theoretical and experiment studies.



REFERENCES

มหาวิทยาลัยเทคโนโลยีสุรนารี



REFERENCES

- Allouche, A. R. (2011). Gabedit-A graphical user interface for computational chemistry softwares. **Journal of Computational chemistry**. 32: 174-182.
- Baker, J., Butcher, V., Dyke, J. M. and Morris, A. (1990). Vacuum Ultraviolet Photoelectron Spectroscopic Study of the NH₂O and HNO molecules. **Journal of the Chemical Society, Faraday Transactions**. 86: 3843-3851.
- Bauschlicher Jr., C. W. and Shavitt, I. (1978). Accurate ab Initio Calculations on the Singlet-Triplet Separation in Methylene. **Journal of the American Chemical Society**. 100: 739-743.
- Bialkowski, S. E. and Guillory W. A. (1978). Collisionless formation and rovibronic relaxation of CH and OH from the ir multiphoton photolysis of CH₃OH. **The Journal of Chemical Physics**. 68: 3339.
- Blitz, M. A., Pilling, M. J. and Seakins, P. W. (2001). Collision induced intersystem crossing in methylene on reactive surfaces: application of a new technique to CH₂(a₁A₁) + H₂. **Physical Chemistry Chemical Physics**. 3: 2241-2244.
- Buenker, R. J., Olbrich, G., Schuchmann, H. P., Schuermann, B. L. and Sonntag, C. V. (1984). Photolysis of methanol at 185 nm. Quantum-mechanical calculations and product study. **Journal of the American Chemical Society**. 106: 4362-4368.

- Bunker, P. R. and Jensen, P. (1983). A refined potential surface for the \tilde{X}^3B_1 electronic state of methylene CH_2 . **The Journal of Chemical Physics**. 79: 1224.
- Buszek, R. J., Sinha, A. and Francisco, J. S. (2011). The Isomerization of Methoxy Radical: Intramolecular Hydrogen Atom Transfer Mediated through Acid Catalysis. **Journal of the American Chemical Society**. 133: 2013-2015.
- Carter, J. T. and Cook, D. B. (1991). The methoxy radical. **Journal of Molecular Structure: THEOCHEM**. 251: 111-122.
- Casavecchia, P., Buss, R. J., Sibener, S. J. and Lee, Y. T. (1980). A crossed molecular beam study of the $O(^1D_2)+CH_4$ reaction. **The Journal of Chemical Physics**. 73: 6351.
- Chen, Z., Eppink, A. T. J. B., Jiang, B., Groenenboom, G. C., Yang, X. and Parker, D. H. (2011). Product pair correlation in CH_3OH photodissociation at 157 nm: the $OH+CH_3$ channel. **Physical Chemistry Chemical Physics**. 13: 2350-2355.
- Cheng, B.-M., Bahou, M., Chen, W.-C., Yui, C.-h., Lee, Y.-P. and Lee, L. C. (2002). Experimental and theoretical studies on vacuum ultraviolet absorption cross sections and photodissociation of CH_3OH , CH_3OD , CD_3OH , and CD_3OD . **The Journal of Chemical Physics**. 117: 1633-1640.
- De Frémont, P., Marion, N. and Nolan, S. P. (2009). Carbenes: Synthesis, properties, and organometallic chemistry. **Coordination Chemistry Reviews**. 253: 862-892.

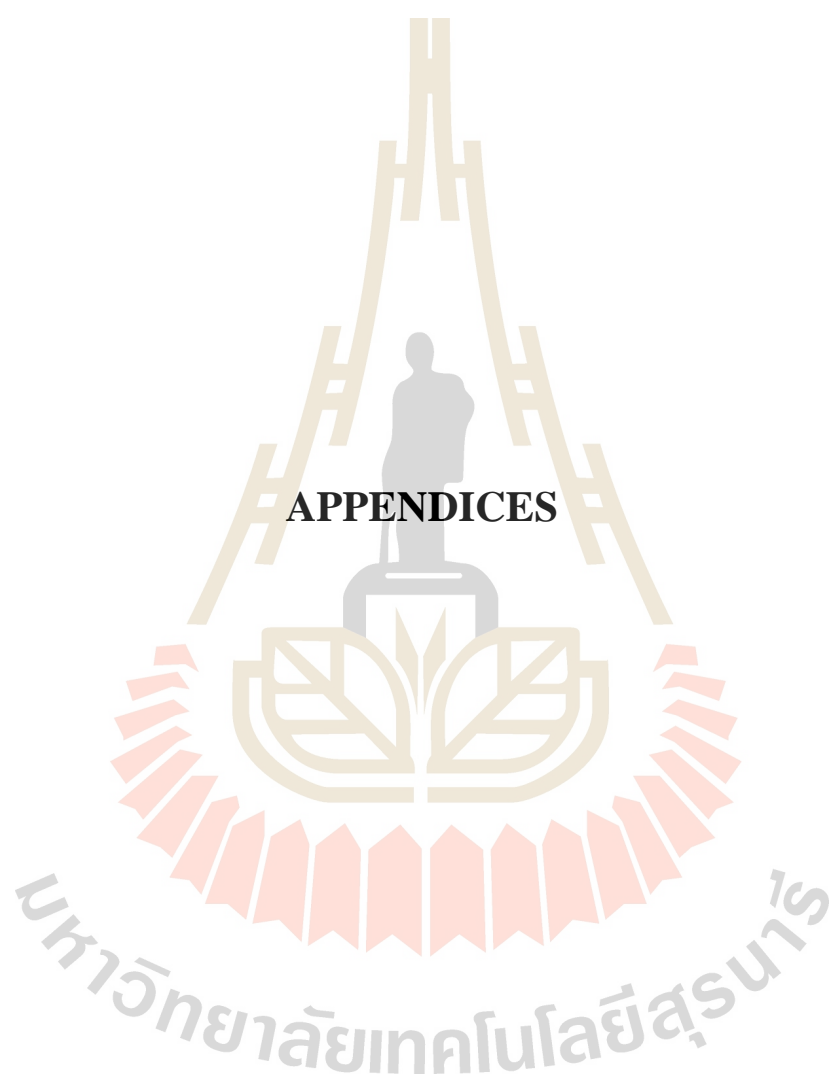
- Gerry, M. C. L., Lees, R. M. and Winnewisser, G. (1976). The torsion-rotation microwavespectrum of $12\text{CH}_3^{18}\text{OH}$ and the structure of methanol. **Journal of Molecular Spectroscopy**. 61: 231-242.
- Gilbert, A. (2002). Photochemistry. **The Royal Society of Chemistry**. Athenaeum Press Ltd, Gateshead, Tyne & Wear.
- Gonzalez, L., Escudero, D. and Serrano-Andres, L. (2012). Progress and Challenges in the Calculation of Electronic Excited States. **Chemical Physics Physical Chemistry**. 13: 28-51.
- Harding, L. B., Schlegel, H. B., Krishnan, R. and Pople, J. (1980). **Potential energy surfaces and dynamics calculations : for chemical reactions and molecular energy transfer**. New York: Plenum Press.
- Jensen, P., Bunker, P. R. and Hoy, A. R. (1982). The equilibrium geometry, potential function, and rotation-vibration energies of CH_2 in the $\tilde{X}^3\text{B}_1$ ground state. **The Journal of Chemical Physics**. 77: 5370.
- Kassab, E., Gleghorn, J. T. and Evleth, E. M. (1983). Theoretical aspects of the photochemistry of methanol, methylamine, and related materials. **Journal of the American Chemical Society**. 105: 1746-1753.
- Kirmse, W. (1971). **Carbene Chemistry**. New York: Academic Press.
- Knowles, P. J. and Werner, H.-J. (1985). An efficient second-order MC SCF method for long configuration expansions. **Chemical Physics Letters**. 115: 259-267.
- Lao-ngam, C., Asawakun, P., Wannarat, S. and Sagarik, K. (2011). Proton transfer reactions and dynamics in protonated water clusters. **Physical Chemistry Chemical Physics**. 13: 4562.

- Lao-ngam, C., Phonyiem, M., Chaiwongwattana, S., Kawazoe, Y. and Sagarik, K. (2013). Characteristic NMR spectra of proton transfer in protonated water clusters. **Chemical Physics**. 420: 50-61.
- Leopold, D. G., Murray, K. K., Miller, S. and Lineberger, W. C. (1985). Methylene: A Study of the $\tilde{X}^3 B_1$ and $\tilde{a}^1 A_1$ States by Photoelectron Spectroscopy of CH_2^- and CD_2^- . **The Journal of Chemical Physics**. 83: 4849-4865.
- Marston, C. C., Weide, K., Schinke, R. and Suter, H. U. (1993). Product selectivity of vibrationally mediated photofragmentation of methanol. **The Journal of Chemical Physics**. 98: 4718.
- McKellar, A. R. W., Bunker, P. R., Sears, T. J., Evenson, K. M., Saykally, R. J. and Langhoff, S. R. (1983). Far infrared laser magnetic resonance of singlet methylene: singlet-triplet perturbations, singlet-triplet transitions, and the singlet-triplet splitting. **The Journal of Chemical Physics**. 79: 5251-5264.
- MOLPRO, version 2015.1, (2015). A package of *ab initio* programs, H.-J. Werner, P. J. Knowles, G. Knizia, F. R. Manby, M. Schütz and others, 2015; available from <http://www.molpro.net>.
- Porter, R. P. and Noyes Jr., W. A. (1959). Photochemical Studies. LIV. Methanol Vapor. **Journal of the American Chemical Society**. 81: 2307-2311.
- Phibbs, M. K. and Darwent, B. deB. (1950). The mercury photosensitized reactions of methyl alcohol. **The Journal of Chemical Physics**. 18: 495.
- Ravishankara, A. R. (1988). Kinetics of radical reactions in the atmospheric oxidation of CH_4 . **Annual Review of Physical Chemistry**. 39: 367-394.

- Saebo, S., Radom, L. and Schaefer III, H. F. (1983). The weakly exothermic rearrangement of methoxy radical (CH_3O) to the hydroxymethyl radical (CH_2OH). **The Journal of Chemical Physics**. 78: 845-853.
- Sagarik, K., Panajapo, P., Phonyiem, M. and Thisuwan, J. (2015). Dynamics of Proton Exchange in a Model Phosphonic Acid-Functionalized Polymer. **International Journal of Quantum Chemistry**. 115: 1161-1174.
- Satyapal, S., Park, J., Bersohn, R. and Katz, B. (1989). Dissociation of methanol and ethanol activated by a chemical reaction or by light. **The Journal of Chemical Physics**. 91: 6873.
- Sarkar, S., Mallick, S., Deepak, D., Kumar, P. and Bandyopadhyay, B. (2017). Isomerization of Methoxy Radical in Troposphere: Competition Between Acidic, Neutral and Basic Catalysts. **Physical Chemistry Chemical Physics**. 19: 27848-27858.
- Schmiedl, R., Meier, U. and Welge, K. H. (1981). State selective laser photofragment spectroscopy of OH in the MPD of CH_3OH in a molecular beam. **Chemical Physics Letters**. 80: 495-498.
- Schreiber, M., Silva-Junior, M. R., Sauer, S. P. A. and Thiel, W. (2008). Benchmarks for electronically excited states: CASPT2, CC2, CCSD, and CC3. **The Journal of Chemical Physics**. 128: 134110.
- Seinfeld, J. H. and Pandis, S. N. (2016). **Atmospheric Chemistry and Physics: From Air Pollution to Climate Change**. John Wiley & Sons, Inc., Hoboken, New Jersey, 3rd edn.
- Shainyan, B. A., Kuzmin, A.V. and Moskalik, M. Y. (2013). Carbenes and Nitrenes. An Overview. **Computational and Theoretical Chemistry**. 1006: 5261.

- Sonntag, C. V. and Schuchmann, H.-P. (1977). **Advances in Photochemistry**. In: Pitts LN, Hammond GS, Gollnick (eds). 10: 59.
- Standard, J. M. (2016). Effects of solvation and hydrogen bond formation on singlet and triplet alkyl or aryl carbenes. **The Journal of Physical Chemistry A**. 121: 381-393.
- Suwannakham, P., Chaiwongwattana, S. and Sagarik, K. (2018). Mechanisms of photoexcitation and photoionization in small water clusters. **Royal Society of Chemistry Advances**. 8: 36731-36744.
- Suwannakham, P. and Sagarik, K. (2017). Dynamics of structural diffusion in phosphoric acid hydrogen-bond clusters. **Royal Society of Chemistry Advances**. 7: 21492-21506.
- Suwannakham, P., Chaiwongwattana, S. and Sagarik, K. (2015). Proton dissociation and transfer in hydrated acid clusters. **International Journal of Quantum Chemistry**. 115: 486-501.
- Sun, J. Q. and Ruedenberg, K. (1994). Locating transition states by quadratic image gradient descent on potential energy surfaces. **The Journal of Physical Chemistry**. 101: 2157.
- Takezaki, Y. and Takeuch, C. (1954). Decomposition of methanol induced by methoxy radicals. **The Journal of Chemical Physics**. 22: 1527.
- Terenin, A. and Neujmin, H. (1935). Photodissociation of polyatomic molecules in the schumann ultraviolet. **The Journal of Chemical Physics**. 3: 436.
- TURBOMOLE V7.2. (2018). A development of University of Karlsruhe and Forschungszentrum Karlsruhe GmbH, 1989-2007, TURBOMOLE GmbH, since 2007; available from <http://www.turbomole.com>.

- Wadt, W. R. and Goddard III, W. A. (1976). The low-lying excited states of water, methanol, and dimethyl ether. **Chemical Physics**. 18: 1-11.
- Wen, Y., Segall, J., Dulligan, M. and Wittig, C. (1994). Photodissociation of methanol at 193.3 nm: Translational energy release spectra. **The Journal of Chemical Physics**. 101: 5665-5671.
- Werner, H.-J., Knowles, P. J., Knizia, G., Manby, F. R. and Schütz, M. (2012). Molpro: a general-purpose quantum chemistry program package. **WIREs Computational Molecular Science**. 2: 242-253.
- Werner, H.-J. and Knowles, P. J. (1985). A second order multiconfiguration SCF procedure with optimum convergence. **The Journal of Chemical Physics**. 82: 5053-5063.
- Werner, H.-J. and Meyer, W. (1980). A quadratically convergent multiconfiguration–self-consistent field method with simultaneous optimization of orbitals and CI coefficients. **The Journal of Chemical Physics**. 73: 2342-2356.



APPENDIX A

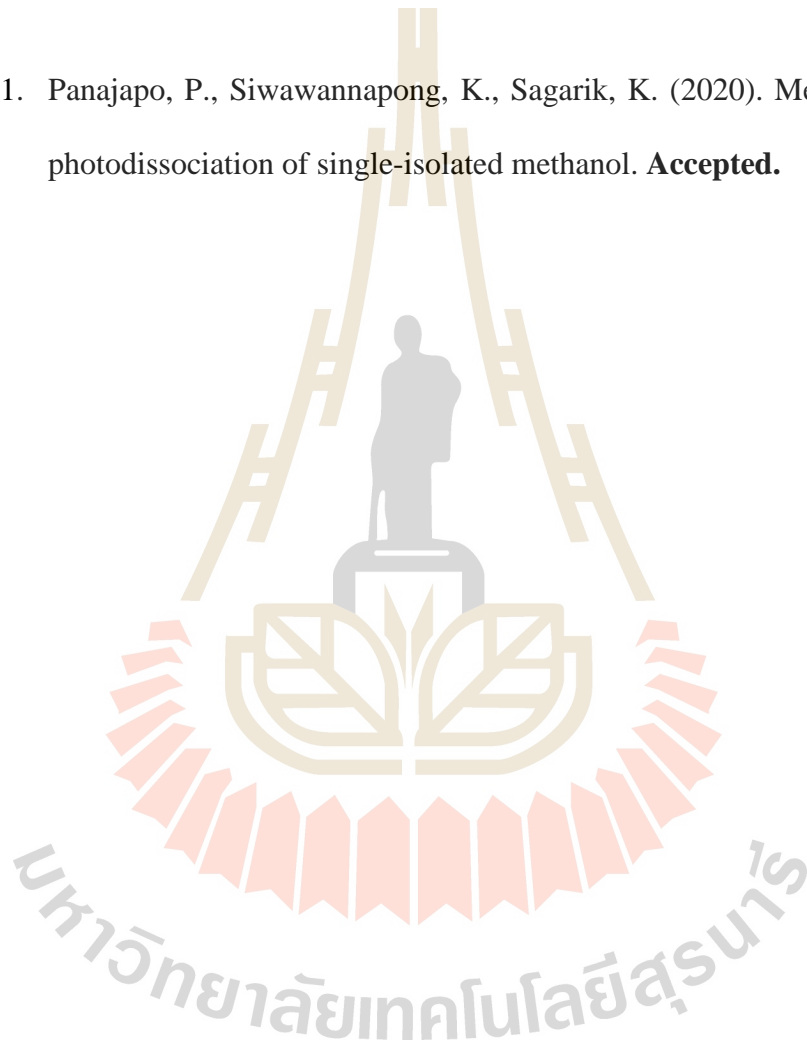
LIST OF POSTER AND PRESENTATION

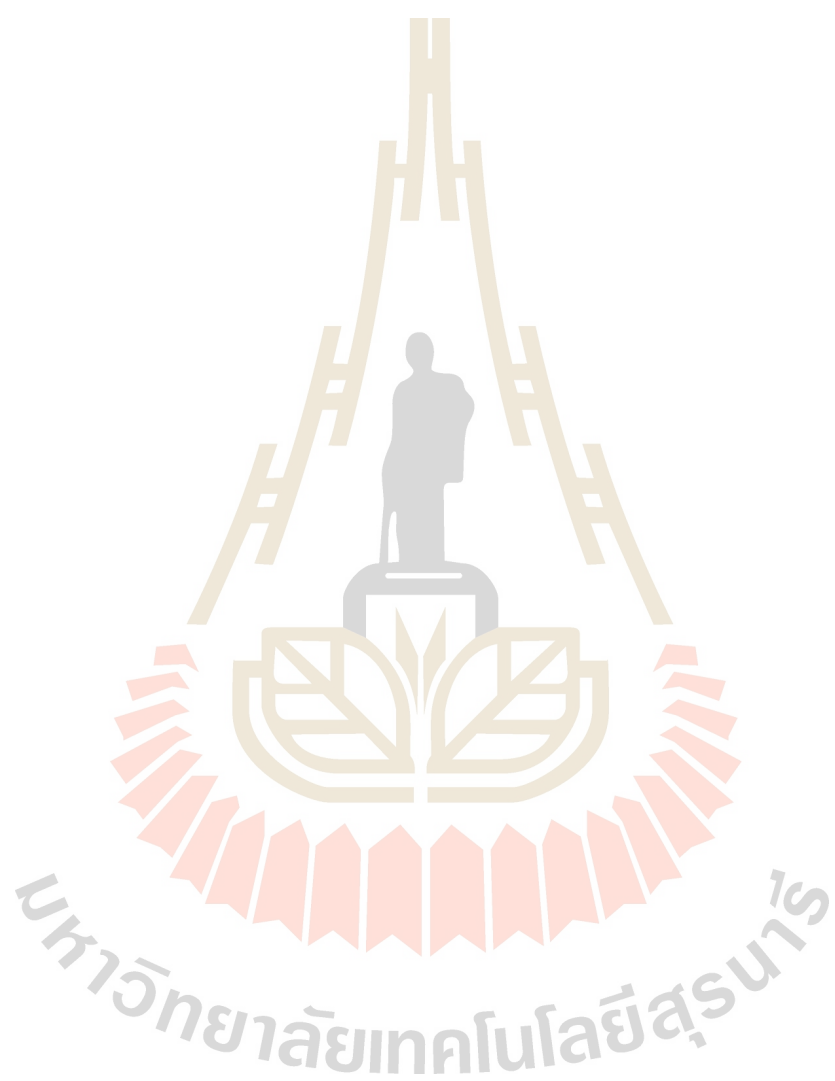
1. Panajapo, P*. and Sagarik, K. (July 23-28, 2013). Dynamics and mechanisms of proton transfer reactions in poly (2-vinylimidazole). **The 7th Conference of the Asain Consortium on Computational Materials Science (ACCMS7)**. Nakhon Ratchasima, Thailand.
2. Sagarik, K*. and Panajapo, P. (September 15-20, 2013). Structural diffusion in hydrogen bond of proton conducting polymer: poly(vinylimidazole) as model system. **Internatinal Conference on Horizons in Hydrogen Bond Research (HBOND2013)**. University of Antwerp, Belgium.
3. Panajapo, P*. and Sagarik, K. (December 2-4, 2014). Effects of backbone conformations on proton transfer in polymer electrolyte membranes. **The 40th Congress on Science and Technology of Thailand (STT40)**. Hotel Pullman Khon Kaen Raja Orchid, Thailand.
4. Panajapo, P*. and Sagarik, K. (June 11-13, 2015). Dynamics and mechanisms of proton transfer reactions in poly (2-vinylimidazole). **RGJ-Ph.D. Congress XVI**. Jomtien Palm Beach Hotel & Resort, Thailand.

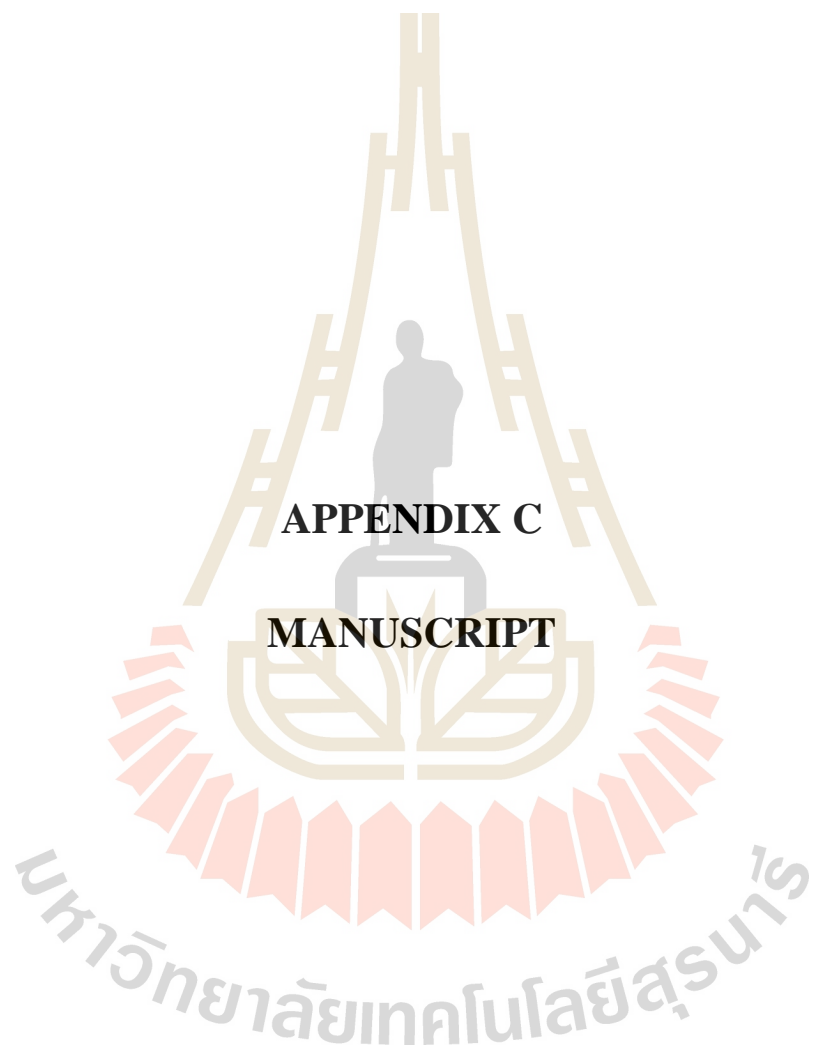
APPENDIX B

PUBLICATION

1. Panajapo, P., Siwawannapong, K., Sagarik, K. (2020). Mechanism of the photodissociation of single-isolated methanol. **Accepted.**







From: aipadv-edoffice@aip.org <aipadv-edoffice@aip.org>
Sent: Wednesday, July 8, 2020 12:01 PM
To: Kritsana Sagarik
Cc: kritsanasagarik@gmail.com
Subject: AIP Advances MS #ADV20-AR-01203-TR2 Decision Letter

Dear Prof. Dr. Sagarik,

We are pleased to inform you that your manuscript, referenced below, has been accepted for publication in AIP Advances and is tentatively scheduled for publication in the July issue:

"Mechanisms of the photodissociations of single-isolated methanol"

Papers published in AIP Advances are subject to an Article Processing Charge, which allows the published paper to be made freely available to all readers and gives authors the broadest possible distribution of their research.

When your manuscript enters the production process, you will receive an email from the AIP Advances production office with further instructions. Direct all questions pertaining to papers in the production process to the contact information supplied in that e-mail. Be sure to include your manuscript number (ADV20-AR-01203-TR2) on all correspondence.

Please note that your manuscript will be evaluated during the production process to ensure that it meets the language standards for the journal. If your manuscript does not meet those standards you may be required to take further action before your paper can be published.

To track the status of your manuscript once it has entered the production process, login to the AIP Advances submission site (<https://aipadvances.pearsonpress.org/submit/main.html>) and click on the Manuscript ID link in the "Manuscripts in Production" folder.

AIP Advances

aipadvances.pearsonpress.org

eJournalPress is mission critical software providing online submission, review and tracking of manuscripts via the Internet. It was designed from the ground up to provide rock solid security, reliability and ease of use.

Thank you for your contribution to the Journal. If you have any questions, please contact us at aipadv-edoffice@aip.org.

Sincerely,

Fei Gao
Associate Editor

Ben Slater
Deputy Editor

AIP Advances
AIP Publishing
Suite 300
1305 Walt Whitman Road
Melville, NY 11747-4300 USA

Mechanisms of the photodissociations of single-isolated methanol†

by

Pannipa Panajapo

Kittipan Siwawannapong

and

Kritsana Sagarik*

School of Chemistry

Institute of Science

Suranaree University of Technology

Nakhon Ratchasima 30000

Thailand

*Corresponding author: kritsana@sut.ac.th

Tel./Fax: (6644) 224635

Keywords: single-isolated methanol, CASPT2, photodissociation mechanisms, lowest singlet-excited state, potential energy surfaces.

†Supplementary material available.

I. INTRODUCTION

The photochemistry of molecules in the gas and condensed phases has been extensively studied in the past decades, with the most investigated topic being the photodissociation of small molecules in the Earth's atmosphere, which leads to serious environmental problems.¹ Solar radiation induces photochemical reactions through the formation of radicals, anions, and cations. Modern spectroscopic techniques, such as fluorescence, resonance-enhanced multiphoton ionization (REMPI), and time-resolved vibrational spectroscopy, in combination with quantum chemical methods, have proven to be powerful tools for studying photodissociation reactions.²

The photodissociation of methanol (CH_3OH) has received particular interest because the methoxy ($[\text{CH}_3\text{O}]^\cdot$) and hydroxymethyl ($[\text{CH}_2\text{OH}]^\cdot$) radical products are reactive intermediates in atmospheric, combustion, and industrial processes.^{1,3} For example, in the Earth's atmosphere, $[\text{CH}_3\text{O}]^\cdot$ can be generated *via* the oxidation of CH_4 .⁴ The photolysis of CH_3OH in the gas phase has been studied extensively using various theoretical and experimental techniques.⁵ Its dissociation paths, radical intermediates and products, electronic states, and associated absorption spectra have attracted general interest. Theoretically, at least five unimolecular dissociation channels exist for CH_3OH in the gas phase.^{6,7} These channels are depicted, along with their standard enthalpies of dissociation (ΔH°), in Fig. 1. Channels (1), (2), and (3) involve the homolytic cleavage of covalent bonds (O-H, C-H, and C-O dissociation, respectively) and generate radical products, whereas the products of channels (4) and (5) are molecules in their electronic ground states.⁷

The photofragmentation of CH_3OH in its lowest singlet-excited state (S_1) has received special attention due to the experimental observation that at 193 nm, the branching ratio of channel (1) is significantly higher than that of channel (3),⁷ despite the fact that the standard enthalpy of dissociation of the former is higher than that of the latter ($\Delta H^\circ = 432$ and 389 kJ/mol, respectively). For alcohols in their electronic ground state, the C-O bond is generally weaker than the O-H bond.⁸ In contrast, an infrared multiple photon dissociation (IRMPD) experiment⁹ revealed that the dominant products of CH_3OH photodissociation are the same as those found from thermal excitation⁷ irrespective of the excitation energy, namely, $[\text{CH}_3]^\cdot$ and $[\text{OH}]^\cdot$ from channel (3). To study the branching ratio of channels (1) and (3), two-dimensional (2D) potential energy surfaces

ABSTRACT

The mechanisms of the photodissociation of single isolated methanol (CH_3OH) molecule in the lowest singlet-excited (S_1) state were systematically studied using the CASPT2 and transition state (TST) theories. This theoretical study focused on the nonradiative relaxation processes that transform the $S_0 \rightarrow S_1$ vertically excited molecule to the products in their respective electronic ground states. The results confirmed that O-H dissociation is the predominant exothermic process and that the formation of formaldehyde (CH_2O) in which the O-H dissociated species are the precursors for the reaction in the S_0 state, is the second most-favorable process. For C-O dissociation, the theoretical results suggested a thermally excited precursor in a different Franck-Condon region in the S_0 state, from which vertical excitation leads to a transition structure in the S_1 state and spontaneously to the $[\text{CH}_3]^\cdot$ and $[\text{OH}]^\cdot$ products in their electronic ground states. The CASPT2 and TST results also revealed the possibility of $[\text{CH}_3\text{OH}] \rightarrow [\text{CH}_2\text{OH}_2]$ isomerization dissociation, in which another thermally excited precursor is vertically excited and C-O dissociation and intermolecular proton transfer lead to the singlet and triplet $[\text{CH}_2] \rightarrow [\text{H}_2\text{O}]$ H-bond complexes in their electronic ground states. Although sufficient thermal energy to generate the precursors in the S_0 state is available and the reactions are kinetically feasible at high temperatures, the strongly kinetically controlled O-H dissociation predominates the C-O and $[\text{CH}_3\text{OH}] \rightarrow [\text{CH}_2\text{OH}_2]$ isomerization dissociations. The present results verified and confirmed the reported theoretical and experimental findings and provided insights into the thermal selectivity and interplay between thermal excitation and photoexcitation.

in the S_0 and S_1 states were constructed using the complete active-space self-consistent field (CASSCF) method.¹⁰ The theoretical results showed that dissociation in the vibrational ground state generates $[\text{CH}_2\text{O}]$ and $[\text{H}]$ exclusively (channel (1)), whereas exciting the CH_3O mode prior to $S_0 \rightarrow S_1$ excitation increases the quantum yield for $[\text{OH}]$.

The photodissociation of CH_3OH through channel (3) was studied at 157 nm using the velocity map imaging technique with the detection of $[\text{CH}_3]$.¹¹ A two-step dissociation process was observed, in which the generation of $[\text{CH}_3\text{O}]$ via O–H bond cleavage was the primary process and the photodissociation of the nascent $[\text{CH}_3\text{O}]$ into $[\text{CH}_3]$ by the probe laser was the secondary process. The proposed dissociation steps were supported by the potential energy surfaces in the S_0 and S_1 states obtained from *ab initio* multireference single- and double-excitation configuration interaction ($\Delta\text{MRD-CI}$) calculations with the freeze-scan method and a photolysis experiment at 185 nm,⁸ which suggested that the homolytic cleavage of the O–H bond occurred along a purely repulsive potential energy curve and was associated with the conversion of the $3s$ Rydberg orbital into a $1s$ atomic orbital (AO) of the dissociating hydrogen atom.

In contrast, C–O bond cleavage occurs along a low-energy-barrier pathway, which results from “a sharply avoided crossing between the respective Rydberg and valence electronic configurations”.⁸ The freeze-scan potential energy surfaces in Ref. [8] also suggested that C–H dissociation in channel (2), which leads to $[\text{CH}_2\text{OH}]$ and $[\text{H}]$, was not favorable in the S_1 state. In the second most-favorable process, i.e., the formation of formaldehyde (CH_2O) via channel (5), the elimination of H_2 occurs on a low-barrier surface. Because the S_0 and S_1 potential energy curves for the formation of CH_2O and H_2 did not intersect at separation distances $R \geq 3 \text{ \AA}$, the authors attributed the generation of these two molecules to “surface-hopping effects” between the S_0 and S_1 states.

The photodissociation of CH_3OH vapor through channels (1)–(3) and (5) was studied at wavelengths below 200 nm using scavengers and CD_3OH .¹² The experimental results showed that the main photolysis products were H_2 , CH_2O , and ethylene glycol ($\text{C}_2\text{H}_4\text{O}_2$), along with small amounts of CO and CH_4 . In the presence of scavengers, the formation of CH_2O and H_2 via channel (5) was concluded to be a primary process. CH_2O could also be formed by the thermal decomposition of $[\text{CH}_3\text{O}]$ or $[\text{CH}_2\text{OH}]$, whereas the contribution of channel (3) was found to be

FIG. 1. Proposed dissociation channels for CH_3OH in the gas phase. δ , γ , $\Delta H^\circ = \text{standard dissociation enthalpy}$.

negligible due to the small amount of methane (CH_4) detected. In addition, although dissociation *via* channels (1) and (2) cannot be easily distinguished experimentally, the authors anticipated that $[\text{CH}_2\text{OH}]^+$ could be formed from CH_3OH through the hydrogen abstraction by $[\text{CH}_3\text{O}]^+$.¹² The predominance of channel (5) was in agreement with the results in Ref. [13], in which equal amounts of CH_2O and H_2 were observed, whereas $[\text{CH}_2\text{OH}]^+$ and $[\text{H}]^+$ were only detected in the initial stage of the mercury-sensitized reaction.

Isomerization-mediated dissociation is one of the most common radical reactions. Photodissociation *via* channel (4) is interesting from a theoretical point of view, because single-point CCSD(T)-F12 and MRCI+Q calculations using an equilibrium structure obtained from B3LYP-D3/aug-cc-pVTZ geometry optimizations showed that the hydrogen-bond (H-bond) complex formed by $^1[\text{CH}_2]$ and $[\text{H}_2\text{O}]$ is 10-13 kJ/mol more stable than that formed between $^3[\text{CH}_2]$ and $[\text{H}_2\text{O}]$.¹⁴ In our opinion, this finding is not reasonable, because the H-bond distance obtained from the B3LYP-D3/aug-cc-pVTZ geometry optimizations is too long.

To clarify the ambiguities that remain due to the limitations of the theoretical and experimental data obtained in previous experiments, in this work, a theoretical study of the mechanisms of the photodissociation of single isolated CH_3OH molecule in the S_1 state has been carried out using *ab initio* calculations at the complete active-space second-order perturbation theory (CASPT2) level and transition state theory (TST). The main purposes of this work are: (1) To provide insight into the unimolecular photodissociation of CH_3OH (i.e., *via* channels (1)-(5)) in the S_1 state, with an emphasis on nonradiative relaxation processes after the $\text{S}_0 \rightarrow \text{S}_1$ vertical excitation that transform the excited CH_3OH molecule into the ground-state products. (2) To identify possible mechanisms for the formation of electronic ground-state precursors whose $\text{S}_0 \rightarrow \text{S}_1$ excitation can lead to the products *via* dissociation channels (2)-(5), because O-H dissociation has been reported to be the predominant process in the S_1 state. (3) To study the effects of the scan method. In the previous work,⁸ a freeze-scan method was used to obtain the MRD-CI potential energy curves. In this method, only the bond distances of the dissociating bonds (e.g., the O-H, C-H, and C-O distances) were varied, while all other degrees of freedom were kept constant. In this work, a relax-scan method, in which all of the important structural parameters on the S_1 potential energy curves were optimized, was used, and the interplay between structure and energetics in the S_0 and S_1 states

were studied in detail. (4) To take into account the effects of thermal energy in this process. None of the previous *ab initio* studies explicitly included the effects of thermal energy. In this work, the thermodynamic (thermal selectivity) and kinetic aspects of the photodissociation processes were investigated based on TST. (5) To study the multiconfigurational character and the effects or contributions of the electronic configurations (states) in the dissociation processes, the values of the configuration interaction (CI) coefficients of the characteristic structures on the S_0 and S_1 potential energy curves were systematically analyzed. The theoretical results obtained in this work have been discussed and compared to the available theoretical and experimental data.

II. COMPUTATIONAL METHODS

A. *Ab initio* calculations

Because the photodissociation of CH_3OH involves the breaking and formation of covalent bonds, closed-shell and open-shell configurations must be considered in *ab initio* calculations of this process.³ To account for the multiconfigurational characteristics of the photolysis of CH_3OH , *ab initio* calculations were performed using the CASPT2 method,¹⁵ which has been accepted as one of the standard methods used in excited-state calculations.¹⁶ Since large-scale *ab initio* CI calculations suggested that the S_1 state of CH_3OH can be represented by a Rydberg-like character¹⁷ that results from an adiabatic $\text{S}_0 \rightarrow \text{S}_1$ ($n \rightarrow 3s$) excitation, all of the S_1 state calculations were conducted adiabatically and restricted to C_1 symmetry. The use of the adiabatic method is supported by the UV absorption spectra of CH_3OH , CH_3OD , CD_3OH , and CD_3OD ,¹⁸ which show only one notable broad structureless peak in the range of 163-210 nm, and by our preliminary CASPT2 calculations for CH_3OH , which showed that most of the $\text{S}_0 \rightarrow \text{S}_1$ excitations are bound-free transitions. However, the absorption spectrum in the range of 140-163 nm is represented by small vibrational modes that were attributed to a "broad double-well-like potential energy curve".¹⁸

In this study, because the energy gradients with respect to the degrees of freedom and the Hessian had to be computed extensively, state-specific CASSCF/CASPT2 calculations with the aug-cc-pVDZ basis set were used to optimize the computational resources. Although the multistate complete-active-space second-order perturbation theory (MS-CASPT2) method might be more accurate,² it is only applicable to small systems. Augmented basis sets with diffuse functions have

been proven to be suitable for singlet-state calculations.¹⁶ In our previous study, CASPT2 calculations with the aug-cc-pVDZ basis set were shown to yield reasonable potential energy curves and $S_0 \rightarrow S_1$ vertical excitation energies for small water clusters.¹⁹

As previous *ab initio* calculations²⁰ and our preliminary calculations showed that only single photons excited the oxygen lone-pairs of CH_3OH , the active space for CH_3OH was defined by assigning four electrons ($n = 4$) to seven active orbitals ($m = 7$), which we abbreviate as the (4,7) active space. The remaining electrons were assigned to seven doubly occupied orbitals (close = 7). For the equilibrium structure with C_{2v} symmetry, the doubly occupied orbitals were $(1a)^2(2a)^2(3a)^2(4a)^2(5a)^2(1a')^2(6a')^2$. Although these orbitals were not part of the active space (close = 7), they were fully optimized. For the (4,7) active space, the active orbitals were $7a'$, $2a''$, $8a'$, $9a'$, $3a''$, $10a'$, and $11a'$; i.e., five orbitals with a' symmetry and two orbitals with a'' symmetry. To ensure that the number of electrons included in the active orbitals was reasonable, calculations were also performed with an extended active space (14,12). Only two orbitals with a' symmetry were found to be doubly occupied ($n = 14$, $m = 12$ and close = 2). The doubly occupied orbitals were $(1a)^2$ and $(2a)^2$ and the active orbitals were $3a'$, $4a'$, $5a'$, $1a''$, $6a'$, $7a'$, $2a''$, $8a'$, $9a'$, $3a''$, $10a'$, and $11a'$. The (4,7) and (14,12) active space calculations involved 196 and 169,884 CASCHF reference wavefunctions, respectively. The details of the (4,7) and (14,12) active space calculations are summarized in Table I.

All *ab initio* calculations were performed using the MOLPRO software package.^{21,22} The Werner-Meyer-Knowles nonlinear optimization method²³⁻²⁵ was used in the CASSCF orbital/state optimizations. To characterize the $S_0 \rightarrow S_1$ excited species, spatial distributions of the natural orbitals were computed and displayed with the same isosurface value (0.11) using the software GABEDIT.²⁶ Information on the electronic configurations of the structures in the S_0 and S_1 states was obtained from analyses of the CI coefficients.

B. Equilibrium geometries and potential energy curves

To obtain fundamental information on the photodissociation processes, the equilibrium geometry of CH_3OH in the S_0 state was optimized using CASPT2(4,7) and (14,12) calculations with the geometry direct inversion in the iterative subspace (DIIS) method²⁷ included in the MOLPRO software package. Because the equilibrium geometry of CH_3OH in the S_0 state is dominated by

the Hartree-Fock reference, to ensure that the selected CASPT2 methods yielded reliable results, the equilibrium geometry and vibrational frequencies were benchmarked against the CCSD(T)/aug-cc-pVDZ method. In this work, harmonic vibrational frequencies were computed using numerically approximating Hessian and central energy differences included in the MOLPRO software package.²⁸

Because O-H dissociation in the S_1 state occurs along a purely repulsive potential energy curve,⁸ the transition states could not be optimized using quadratic steepest descent (QSD) method; a recommended method for transition state optimizations in the MOLPRO software package. Therefore, to search for the transition structures in dissociation channels (1)-(3), S_1 potential energy curves with respect to the O-H, C-H, and C-O coordinates were constructed. In contrast to previous studies, which employed freeze-scan methods,^{8,10,18,29} the present work used a relax-scan method, in which all important structural parameters on the S_1 potential energy curves were optimized using CASPT2(4,7) calculations. Since preliminary CASPT2(4,7) calculations showed that the C-H bond lengths did not significantly change along the S_1 potential energy curves, the C-H bond distances were constrained at the equilibrium value in the S_0 state ($R_{\text{C-H}} = 1.10 \text{ \AA}$) to reduce the computational effort. In addition, because O-H dissociation is the most favorable process in the S_1 state, the S_1 potential energy curves for C-H and C-O dissociation were tentatively constructed by constraining the O-H distance at the equilibrium value in the S_0 state ($R_{\text{O-H}} = 0.97 \text{ \AA}$). The S_1 potential energy curves with a constrained O-H distance were used to search for the precursors in the S_0 state whose $S_0 \rightarrow S_1$ vertical excitation leads to a transition structure for the C-H and C-O dissociations in the S_1 state. All of the S_0 potential energy curves obtained from the CASPT2(4,7) and (14,12) methods were compared with the results obtained from the CCSD(T)/CBS method.

To study photodissociation *via* channel (4), the S_1 potential energy curve for unimolecular $[\text{CH}_3\text{OH}] \rightarrow [\text{CH}_2\text{OH}]$ isomerization, which leads to the products $[\text{CH}_2]$ and $[\text{H}_2\text{O}]$ in their respective electronic ground states, was constructed. The O–H distance was constrained at 0.97 Å, and intramolecular isomerization was simulated by transferring one of the hydrogen atoms from the CH_3 group to the OH group. Because the single-point single-reference CCSD(T)-F12 method predicted that the $^1[\text{CH}_2]\text{--}[\text{H}_2\text{O}]$ H-bond complex was more strongly associated than the $^3[\text{CH}_2]\text{--}[\text{H}_2\text{O}]$ H-bond complex, singlet-triplet intersystem crossing and H-bond formation were taken into account for channel (4) by performing CASPT2(4,7) geometry optimization on the $[\text{CH}_2]\text{--}[\text{H}_2\text{O}]$ H-bond complex in the S_0 and T_1 states. In addition, because formaldehyde formation was suggested to involve a nonconcerted process in which dehydrogenation proceeds after O–H dissociation,⁸ the S_1 potential energy curve for H_2 elimination was constructed using the O–H dissociated products in channel (1) ($[\text{CH}_3\text{O}^\bullet$ and $[\text{H}]^\bullet$) as the precursors to discuss the mechanism in channel (5). The constrained structural parameters and degrees of freedom used in the calculations of the S_1 potential energy curves are summarized in Fig. 2.

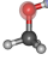
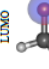
C. Effects of thermal energy in the photodissociation reactions

Because the total energies derived from quantum chemical calculations do not take thermal energy, which underlies the thermodynamic and kinetic aspects of chemical reactions, into account, the effects of temperature and thermal selectivity on the elementary processes were included in the model calculations using transition state theory (TST).^{30, 31} For elementary processes with energy barriers higher than the thermal energy ($k_B T$),³² unimolecular rate constants were calculated over the temperature range 200–1200 K. The classical rate constants (k^{Class}) and rate constants with quantized vibrations ($k^{\text{Q-vib}}$) were initially computed. The classical rate constants were computed using the expression:³³

$$k^{\text{Class}}(T) = \frac{k_B T}{h} \frac{Q^\ddagger}{Q^R} e^{-\Delta E^\ddagger/k_B T}, \quad (1)$$

where ΔE^\ddagger is the energy barrier of the relax-scan potential energy curve, k_B and h are the Boltzmann and Planck constants, respectively, and Q^R and Q^\ddagger are the partition functions of the reactant and transition structures, respectively. The barrier heights obtained with the zero-point vibrational energies ($\Delta E_{\text{ZPE}}^\ddagger$) were used in the calculations of the rate constants with quantized vibrations ($k^{\text{Q-vib}}$):

TABLE I. The number of configuration state functions (CSFs) considered (N e-internal) and those generated by the CASPT2 methods ($N-1$ and $N-2$ e-internals) used in the calculations of CH_3OH . The values of the HOMO-1, HOMO and LUMO isosurfaces are 0.11.

| Structure | CASPT2 (n,nd) | Number of CSFs | | E^{th} | S_1 | | S_0 | |
|--|------------------|------------------|--|-----------------|-------------------------|-----------|---------------------|-----------|
| | | N e-internal | N-2 e-internal | | Conf. | CI Coeff. | Conf. | CI coeff. |
|  LUMO | | | | | Ψ_9^{D} | 0.9850 | Ψ_0 | 0.9829 |
|  HOMO | (4,7) [14,12] | 196 [169,884] | 112 [339,768] 49 [608,751] [648] | 6.74 [6.48] | $\Psi_{9,3}^{\text{D}}$ | 0.0909 | Ψ_9^{D} | 0.0730 |

n = number of active electrons; n = number of active orbitals; $[]$ = value obtained from CASPT2(4,12) calculations; E^{th} = vertical excitation energy in eV; S_0 and S_1 = ground and lowest singlet excited states, respectively; Ψ_0 = electronic ground state; Ψ_9^{D} and Ψ_9^{D} = $s \rightarrow r$ singly excited state (S-type); $\Psi_{9,3}^{\text{D}}$ = $s \rightarrow r$ and $b \rightarrow s$ doubly excited state (D-type); the indices s and b , and r and s label occupied and virtual or unoccupied spin orbitals, respectively; a bar or lack of a bar is to denote beta (β) and alpha (α) spin orbitals, respectively.

$$k^{\text{Q-cvb}}(T) = \frac{k_B T}{h} \frac{Q_{\text{ZPE}}^{\ddagger}}{Q_{\text{ZPE}}^{\text{R}}} e^{-\Delta E_{\text{ZPE}}^{\ddagger}/k_B T}, \quad (2)$$

where $Q_{\text{ZPE}}^{\ddagger}$ and $Q_{\text{ZPE}}^{\text{R}}$ are the partition functions of the transition and reactant structures obtained, referenced to their zero-point vibrational energies. The crossover temperatures (T_c), i.e., the temperatures below which the transition states are dominated by quantum mechanical tunneling, were also estimated.³⁴

$$T_c = \frac{h\Omega^{\ddagger}}{\Delta E^{\ddagger}}. \quad (3)$$

In Eqn. (3), Ω^{\ddagger} is the imaginary frequency of the transition structure.

The discussion of the effects of thermal energy focuses on the results at the highest temperature (1200 K), as the population of high-energy precursors would be greatest at this temperature. However, to justify the hypothesis that quantum mechanical tunneling was not significant, the rate constants were corrected using the Eckart correction (k^{Eckart}).³⁵ This correction is based on the probability of quantum mechanical tunneling and polynomial fitting of the potential energy curve. In this case, quantum mechanical harmonic oscillators are assumed for all degrees of freedom perpendicular to the reaction coordinate.

To discuss the effects of thermal energy, the enthalpy changes (ΔH) in the elementary processes were computed. The Eyring equation was used for elementary reactions that follow the Arrhenius behavior with energy barriers (ΔE^{\ddagger}) higher than $k_B T$.³³

$$\ln k^{\text{Q-cvb}}(T) = \ln A - \frac{\Delta H^{\ddagger}}{RT} + \frac{\Delta S^{\ddagger}}{R}, \quad (4)$$

where ΔS^{\ddagger} is the entropy of activation and R is the gas constant. ΔH^{\ddagger} is the enthalpy of activation obtained from the linear relationship between $\ln k^{\text{Q-cvb}}(T)$ and $1/T$. The conventional relative Gibbs free energy expression ($\Delta G^{\ddagger, \text{rel}} = \Delta H^{\ddagger, \text{rel}} - T\Delta S^{\ddagger, \text{rel}}$) was used for spontaneous elementary reactions with energy barriers less than $k_B T$ ($\Delta G \leq 0$ or barrierless), through the linear relationship between $\Delta G^{\ddagger, \text{rel}}$ and T , and the exothermic energy ($|\Delta H^{\ddagger, \text{rel}}|$) as the y-intercept. All TST calculations were carried out using the program DL-FIND³⁶ incorporated in the ChemShell software package.³⁷

FIG. 2. a) Equilibrium structure of CH₃OH in the S₀ state obtained from CASPT2(4,7) geometry optimizations. b)-f) Constrained structural parameters used in the calculations of the S₁ relax-scan potential energy curves for dissociation channels (1)-(5), respectively. Double sided arrows represent the degrees of freedom used in the calculations of the S₁ relax-scan potential energy curves. Distances are in Å.

III. RESULTS AND DISCUSSION

To facilitate the discussion, each of the characteristic structures of CH_3OH in the S_0 and S_1 states is referred to using a three-character code, e.g., Gk-[l], Ek-[l][†], or Ek-[l]^{*}, where G represents a structure in the S_0 state and E a structure in the S_1 state. The value of k corresponds to dissociation channels (1)–(5). Different CH_3OH structures in the same dissociation channel are distinguished by [l]^{*} and [†] denote vertically excited structures and structures at the intersection of the S_0 and S_1 potential energy curves, respectively, whereas [†] refers to transition structures. For example, using this three-character code, structures G1-[1]^{*} and E1-[1]^{*} represent the same structures ($l = 1$) computed in the S_0 (G) and S_1 (E) states, respectively. These structures are involved in O-H dissociation in channel (1) ($k = 1$). Structures E4-[1]^{*} and E4-[2][†] are different structures ($l = 1$ and 2) on the S_1 potential energy curve for the $[\text{CH}_3\text{OH}]\rightarrow[\text{CH}_2\text{OH}_2]$ isomerization ($k = 4$). They are vertically excited (^{*}) and transition structures ([†]), respectively.

The characteristic structures and energies for O-H dissociation, as well as the three leading electronic configurations and CI coefficients (cut-off = 0.05) obtained from the CASPT2(4,7) calculations, are given as examples in Table II, where Ψ_0 and C_0 correspond to the electronic ground state, Ψ_a^r and C_a^r to an a→r singly excited state (S-type); and $\Psi_{a,b}^{rs}$ and $C_{a,b}^{rs}$ to an a→r and b→s doubly excited state (D-type). The indices a and b, as well as r and s, denote occupied and virtual or unoccupied spin orbitals, respectively; the bar or lack of bar indicates beta (β) or alpha (α) spin orbitals, respectively.

The potential energy curves with respect to the O–H, C–O, and C–H coordinates are shown in Fig. 3. The potential energy curves for $[\text{CH}_3\text{OH}]\rightarrow[\text{CH}_2\text{OH}_2]$ isomerization and formaldehyde formation are shown in Figs. 4 and 5, respectively. The energies and structural parameters of the characteristic structures of CH_3OH on the potential energy curves are summarized in Table S1(a)[†]. The equilibrium geometries and vibrational frequencies in the electronic ground state obtained from CASPT2(4,7), CASPT2(14,12) and CCSD(T) calculations with the aug-cc-pVDZ basis set are compared with the values obtained from experiments in Tables S1(b)[†] and S1(c)[†], respectively. The three leading electronic configurations and CI coefficients of the characteristic structures are included in Tables S2–S5[†].

FIG. 3. a)–c) The potential energy curves with respect to the O–H, C–O and C–H coordinates obtained from the CASPT2(4,7)/aug-cc-pVDZ, CASPT2(14,12)/aug-cc-pVDZ and CCSD(T)/CBS methods. Solid lines represent the relax-scan potential energy curves. Dash lines denote the energies calculated using the geometries on the relax-scan potential energy curves. Relative energies (E^{rel}) and distances are in kJ/mol and Å, respectively. The values of the HOMO and LUMO isosurfaces are 0.11. Gr₋(4,7) and Ex₋(4,7) = relative energies obtained from CASPT2(4,7) calculations in the S_0 and S_1 states, respectively; Gr₋(14,12) and Ex₋(14,12) = relative energies obtained from CASPT2(14,12) calculations in the S_0 and S_1 states, respectively; Gr₋CCSD(T) = relative energies obtained from CCSD(T) calculations in the S_0 state; [†] = transition structure; δ = structure at the intersection of the S_0 and S_1 potential energy curves; and ΔE^{rel} and ΔE^{\ddagger} = energy release and barrier on the Ex₋(4,7) and Gr₋(4,7) potential energy curves, respectively.

FIG. 4. a) The potential energy curves for $[\text{CH}_3\text{OH}]\rightarrow[\text{CH}_2\text{OH}_2]$ isomerization obtained from the CASPT2(4,7)/aug-cc-pVDZ, CASPT2(14,12)/aug-cc-pVDZ and CCSD(T)/CBS methods. Solid line represents the relax-scan potential energy curve. Dash lines denote the energies calculated using the geometries on the relax-scan potential energy curve. Relative energies (E^{rel}) and distances are in kJ/mol and Å, respectively. The values of the HOMO and LUMO isosurfaces are 0.11. Gr₋(4,7) and Ex₋(4,7) = relative energies obtained from CASPT2(4,7) calculations in the S_0 and S_1 states, respectively; Gr₋(14,12) and Ex₋(14,12) = relative energies obtained from CASPT2(14,12) calculations in the S_0 and S_1 states, respectively; Gr₋CCSD(T) = relative energies obtained from CCSD(T) calculations in the S_0 state; [†] = transition structure; and ΔE^{\ddagger} = energy barriers on the Ex₋(4,7) and Gr₋(4,7) potential energy curves.

b) Equilibrium structures of the $[\text{CH}_2]\cdot\text{[H}_2\text{O}]$ H-bond complexes in the S_0 and T_1 states, obtained from CASPT2(4,7) calculations. The values in parentheses are the results reported in Ref. [20].

All thermodynamic and kinetic results obtained from the TST calculations are included in Tables S6-S9[†]. The kinetic results suggested that quantum mechanical tunneling was only potentially important for elementary processes involving O-H dissociation, e.g., channels (1) and (4); at the highest temperature (1200 K), the value of k^{Eckart} is approximately 8% and 2% higher than that of $k^{\text{Q-ub}}$ for the direct O-H bond and $[\text{CH}_3\text{OH}]\text{-}[\text{CH}_2\text{OH}_2]$ isomerization dissociation, respectively. These findings confirmed the applicability of $k^{\text{Q-ub}}$ at high temperatures.

A. Equilibrium structures

The equilibrium structure of CH_3OH in the electronic ground state obtained from CASPT2(4,7) calculations is shown in Fig. 2(a) (structure G1-[1]) with $R_{\text{O}(\text{O})\text{-H}(\text{O})} = 0.97 \text{ \AA}$, $R_{\text{C}(\text{O})\text{-H}(\text{O})} = 1.10 \text{ \AA}$, $R_{\text{C}(\text{O})\text{-O}(\text{O})} = 1.42 \text{ \AA}$, $\angle\text{H}(\text{O})\text{C}(\text{O})\text{H}(\text{O}) = 109^\circ$, and $\angle\text{H}(\text{O})\text{O}(\text{O})\text{C}(\text{O}) = 108^\circ$. The structural parameters obtained from the CASPT2(14,12) geometry optimizations were approximately the same ($R_{\text{O}(\text{O})\text{-H}(\text{O})} = 0.97 \text{ \AA}$, $R_{\text{C}(\text{O})\text{-H}(\text{O})} = 1.10 \text{ \AA}$, $R_{\text{C}(\text{O})\text{-O}(\text{O})} = 1.44 \text{ \AA}$, $\angle\text{H}(\text{O})\text{C}(\text{O})\text{H}(\text{O}) = 109^\circ$, and $\angle\text{H}(\text{O})\text{O}(\text{O})\text{C}(\text{O}) = 107^\circ$). The values are in good agreement with those obtained from CCSD(T)/aug-cc-pVDZ geometry optimizations (Table S1(b)[†]) and the microwave and millimeter wave spectrum ($R_{\text{O}(\text{O})\text{-H}(\text{O})} = 0.95 \text{ \AA}$, $R_{\text{C}(\text{O})\text{-H}(\text{O})} = 1.09 \text{ \AA}$, $R_{\text{C}(\text{O})\text{-O}(\text{O})} = 1.42 \text{ \AA}$, $\angle\text{H}(\text{O})\text{C}(\text{O})\text{H}(\text{O}) = 108^\circ$ and $\angle\text{H}(\text{O})\text{O}(\text{O})\text{C}(\text{O}) = 108^\circ$).³⁸ The vibrational frequencies of CH_3OH obtained from the CASPT2 and CCSD(T) methods are also in accordance with the experimental results (Table S1(c)[†]).

FIG. 5. The potential energy curves for formaldehyde formation from the O-H dissociated structure (structure EL-[4]‡) obtained from the CASPT2(4,7)/aug-cc-pVDZ, CASPT2(14,12)/aug-cc-pVDZ and CCSD(T)/CBS methods. Solid line represents the relax-scan potential energy curve. Dash lines denote the energies calculated using the geometries on the relax-scan potential energy curve. Relative energies (E^{rel}) and distances are in kJ/mol and \AA , respectively. The values of the HOMO and LUMO isosurfaces are 0.11. Gr_(4,7) and Ex_(4,7) = relative energies obtained from CASPT2(4,7) calculations in the S_0 and S_1 states, respectively; Gr_(14,12) and Ex_(14,12) = relative energies obtained from CASPT2(14,12) calculations in the S_0 and S_1 states, respectively; Gr_CCSD(T) = relative energies obtained from CCSD(T) calculations in the S_0 state; † = transition structure; ‡ = structure at the intersection of the S_0 and S_1 potential energy curves; and ΔE^{rel} and ΔE^\ddagger = energy release and barrier on the Ex_(4,7) and Gr_(4,7) potential energy curves, respectively.

The $S_0 \rightarrow S_1$ vertical excitation energies obtained from the CASPT2(4,7) and (14,12) calculations were 6.74 and 6.48 eV, respectively. These values are in excellent agreement with *ab initio* MRD-CI calculations⁸ and experiments at 6.94 and 6.75 eV, respectively.¹⁸ Therefore, $[\text{CH}_2\text{OH}]^+$ could be formed by isomerization of the dissociated product $[\text{CH}_2\text{O}]^+$.³⁹

For the structure G1-[1], the shapes of the HOMO-1 ($n_{\text{orb}} = 8$), HOMO ($n_{\text{orb}} = 9$), and LUMO ($n_{\text{orb}} = 10$) in Table I show the electron density distributions of the O-H bonding, lone-pair, and O-H anti-bonding natural orbitals, respectively. The CI coefficients obtained from the CASPT2(4,7) calculations reveal that in the S_0 state, the ground state configuration Ψ_0 dominates with a small contribution from the singly excited configuration Ψ_9^{\uparrow} ($C_0 = 0.9829$ and $C_9^{\uparrow} = 0.0730$), whereas in the S_1 state, the singly excited configuration Ψ_9^{\uparrow} is dominant with a small contribution from the doubly excited configuration $\Psi_{9,9}^{\uparrow\uparrow}$ ($C_9^{\uparrow} = 0.9850$ and $C_{9,9}^{\uparrow\uparrow} = 0.0909$).

B. O-H dissociation

The S_1 relax-scan potential energy curve with respect to the O-H coordinate obtained from the CASPT2(4,7) method is illustrated in Fig. 3(a). The energies of the CASPT2(14,12) and CCSD(T)/CBS methods were calculated using the CASPT2(4,7) geometries. The shapes of the S_1 potential energy curves obtained using both CASPT2 methods are approximately the same. Likewise, the shapes of the S_0 potential energy curves obtained using both CASPT2 methods are the same as that obtained from the CCSD(T)/CBS method. Because the same results were obtained for all of the S_0 and S_1 potential energy curves calculated in this work (Figs. 3–5), the applicability of the CASPT2(4,7) method for calculation of the potential energy curves of CH_2OH was confirmed; thus, only the CASPT2(4,7) results have been discussed throughout this study.

The S_1 potential energy curves in Fig. 3(a) reveal that $S_0 \rightarrow S_1$ vertical excitation of structure G1-[1]⁺ leads to structure EL-[1]⁺. Structure EL-[1]⁺ is transformed into structure EL-[2]⁺, in which O-H dissociation occurs at $R_{\text{O}(\text{O})\text{-H}(\text{O})} = 1.40$ Å. The shape of the LUMO in Fig. 3(a) suggests that structure EL-[2]⁺ is a $[\text{CH}_2\text{O}]^+ \cdots [\text{H}]^+$ radical pair (diradical), which dissociates into the products $[\text{CH}_2\text{O}]^+$ and $[\text{H}]^+$ in their respective electronic ground states at the intersection of the S_0 and S_1 states at $R_{\text{O}(\text{O})\text{-H}(\text{O})} = 2.60$ Å (structure G1-[3]⁺ with $E^{\text{ex}} \approx 0$ eV). Table S1(a)[†] shows that the

TABLE II. Characteristic structures of CH_2OH on the S_0 and S_1 potential energy curves for the O-H dissociation. The electronic configurations and CI coefficients were obtained from CASPT2(4,7) calculations in the S_0 and S_1 states. The values of the LUMO isosurfaces are 0.11.

| Structure | S_1 | | S_0 | | |
|---------------------|---------------------------------|-----------|---------------------|---------------------------------|--------|
| | Conf. | CI Coeff. | Structure | Conf. | |
| EL-[1] ⁺ | Ψ_9^{\uparrow} | 0.9850 | G1-[1] ⁺ | Ψ_0 | 0.9830 |
| | $\Psi_{9,9}^{\uparrow\uparrow}$ | 0.0890 | | Ψ_9^{\uparrow} | 0.0723 |
| | $\Psi_{9,8}^{\uparrow\uparrow}$ | 0.0715 | | $\Psi_{3,8}^{\uparrow\uparrow}$ | 0.0698 |
| EL-[2] ⁺ | Ψ_9^{\uparrow} | 0.9639 | G1-[2] ⁺ | Ψ_0 | 0.9511 |
| | $\Psi_{9,8}^{\uparrow\uparrow}$ | 0.2262 | | Ψ_9^{\uparrow} | 0.1997 |
| | Ψ_9^{\uparrow} | 0.0496 | | $\Psi_{3,8}^{\uparrow\uparrow}$ | 0.1719 |
| EL-[3] ⁺ | Ψ_9^{\uparrow} | 0.9746 | G1-[3] ⁺ | Ψ_0 | 0.8381 |
| | $\Psi_{9,8}^{\uparrow\uparrow}$ | 0.1973 | | Ψ_9^{\uparrow} | 0.4241 |
| | $\Psi_{9,8}^{\uparrow\uparrow}$ | 0.0604 | | $\Psi_{3,8}^{\uparrow\uparrow}$ | 0.2688 |

Ψ_0 = electronic ground state; Ψ_i = a-r singly excited state (S-type); $\Psi_{a,b}^{\uparrow}$ = a-r and b-s doubly excited state (D-type); the indices a and b, and r and s label occupied and virtual or unoccupied spin orbitals, respectively; a bar or lack of a bar is to denote beta (β) and alpha (α) spin orbitals, respectively.

extension of the O-H bond in the S_1 state is accompanied by shortening of the C-O bond from $R_{C(O)-O(O)} = 1.42$ Å in structure **E1-[1]**[†] to $R_{C(O)-O(O)} = 1.39$ Å in structures **E1-[2]**[†] and **E1-[3]**[‡].

The transformation of structure **E1-[1]**[†] into **E1-[3]**[‡] in the S_1 state occurs through homolytic cleavage of the O-H bond along a purely repulsive potential energy curve. Based on the approximation that structure **E1-[1]**[†] dissociates spontaneously into the products $[CH_3O]$ and $[H]$ in their respective electronic ground states at $R_{O(O)-H(O)} = 2.60$ Å (Table S7, $\Delta G^{298} = -298$ kJ/mol at 1200 K), the thermal energy due to the exothermic process could be approximated as $\Delta H^{298} = 189$ kJ/mol. This value is in excellent agreement with the experimentally determined available energy (188 kJ/mol) following the production of $[CH_3O]$ and $[H]$ via absorption of a 193 nm photon;⁷ at 193 nm, the maximum translation energy release obtained based on the high- n Rydberg time-of-flight (HRTOF) method was 178 kJ/mol.²⁹ Since the experiment showed that 82% of the energy release (ΔH^{298}) was translational energy,⁷ a maximum kinetic energy of 155 kJ/mol (equivalent to 18,640 K) could be transferred to another CH_3OH molecule.

In the electronic ground (S_0) state, the energy barrier (ΔE^\ddagger) for O-H dissociation was 443 kJ/mol, which is also in excellent agreement with the experimental value of 422 kJ/mol.⁴⁰ *Ab initio* MRD-CI calculations for the S_0 state using a freeze-scan method yielded a smaller energy barrier of $\Delta E^\ddagger = 418$ kJ/mol.⁸ Therefore, O-H dissociation in channel (1) was confirmed to be most favorable in the S_1 state, which is in accordance with all previous theoretical and experimental studies.^{7, 10, 11}

41

The CI coefficients in Table II show the dependence of the electronic configurations on the O-H distance. This is especially apparent in the S_0 state. While the CI coefficient of Ψ_0 gradually decreases from $C_0 = 0.9830$ for structure **G1-[1]**[†] to $C_0 = 0.9511$ for structure **G1-[2]**[†] and to $C_0 = 0.4241$ for structure **G1-[3]**[‡], the contribution of the singly excited configuration Ψ_8^{IV} to the transition structure increases and becomes dominant at the intersection of the S_0 and S_1 states, where $C_8^{\text{IV}} = 0.1997$ and 0.8581 for structures **G1-[2]**[†] and **G1-[3]**[‡], respectively. The situation seems to be different in the S_1 state, in which the CI coefficient of the singly excited configuration Ψ_6^{IV} dominates and varies within a narrow range on the S_1 potential energy curve. The contribution of Ψ_6^{IV} varies from $C_6^{\text{IV}} = 0.9850$ for structure **E1-[1]**[†] to $C_6^{\text{IV}} = 0.9639$ for structure **E1-[2]**[†] and to $C_6^{\text{IV}} = 0.9746$ for structure **E1-[3]**[‡]. It should be noted that at the intersection of the

20

S_0 and S_1 states (at long O-H distances), the lone-pair natural orbitals of the oxygen atom are degenerate; the energies and shapes of the HOMO-1 ($n_{\text{orb}} = 8$) and HOMO ($n_{\text{orb}} = 9$) are approximately the same. Therefore, the singly excited states Ψ_8^{IV} and Ψ_9^{IV} of structures **G1-[3]**[‡] and **E1-[3]**[‡] are equivalent.

Analysis of the CI coefficients in Table II also shows that in the S_0 state, electronic configuration inversion, in which the singly excited state Ψ_8^{IV} becomes more important than the lower-energy electronic ground state Ψ_0 , results in an increase in the total energy and leads to the convergence of the S_0 and S_1 potential energy curves at long O-H distances. Therefore, the electronic configuration inversion $\Psi_0 \rightarrow \Psi_8^{\text{IV}}$ can be considered to be characteristic of O-H dissociation, with $R_{O(O)-H(O)} = 1.40$ Å being the "threshold structural parameter" for inversion (structure **G1-[2]**[†] with $\Delta H^\ddagger = 184$ kJ/mol, Table S6[†]). This electronic configuration inversion explains why O-H dissociation is a strongly endothermic process in the S_0 state, while the lack of electronic configuration inversion in the S_1 state results in a purely repulsive potential energy curve.

C. C-O dissociation

Due to the predominance of O-H dissociation in the S_1 state, O-H dissociation must be temporarily suppressed to study C-O dissociation (channel (3)). The S_1 potential energy curve with respect to the C-O coordinate was constructed by constraining the O-H distance to the ground-state equilibrium distance ($R_{O(O)-H(O)} = 0.97$ Å). The S_1 potential energy curve in Fig. 3(b) shows that starting from the $S_0 \rightarrow S_1$ vertically excited structure **E3-[1]**[†] with $R_{C(O)-O(O)} = 1.42$ Å, C-O dissociation occurs through the transformation of the CH_3 structure from a pyramidal (structure **E3-[1]**[†]) to planar structure (structure **E3-[3]**[‡]). C-O bond cleavage is observed at approximately $R_{C(O)-O(O)} = 1.60$ Å (structure **E3-[2]**[†]) and the energy barrier ΔE^\ddagger is 15.0 kJ/mol. A small ΔE^\ddagger was also found on the freeze-scan potential energy curve.⁸ The relaxation of structure **E3-[2]**[†] to structure **E3-[3]**[‡] at $R_{C(O)-O(O)} = 2.30$ Å is an exothermic process with $\Delta H^{298} = -1.65$ kJ/mol (Table S7[†]) and is accompanied by a decrease in $\angle H(O)C(O)O(O)$ from 108° in structure **E3-[1]**[†] to 99° in structure **E3-[3]**[‡] (Table S1(a)[†]).

As mentioned above, the S_1 potential energy curve for C-O dissociation was calculated by constraining the O-H distance to $R_{O(O)-H(O)} = 0.97$ Å; without this constraint, the reaction would

21

preferentially proceed along O-H dissociation path. To confirm that the transition structure for C-O dissociation is structure E3-[2][‡] with $R_{C(1)-O(5)} = 1.60$ Å, CASPT2(4,7) geometrical optimization without any geometrical constraints was performed for structure E3-[2][‡]. The optimization was started with the $R_{C(1)-O(5)}$ distances slightly shifted, where $R_{C(1)-O(5)} = 1.55$ and 1.65 Å. The results show that for $R_{C(1)-O(5)} = 1.55$ Å, structure E3-[2][‡] relaxes to structure E1-[3][‡] (the O-H dissociated structure), whereas for $R_{C(1)-O(5)} = 1.65$ Å, C-O dissociation occurs, leading to the products [CH₃][•] and [OH][•] (structure E3-[3][‡]) in their respective electronic ground states. Therefore, $R_{C(1)-O(5)} = 1.60$ Å can be regarded as the threshold structural parameter for C-O dissociation.

These findings suggest that photodissociation of the C-O bond cannot proceed through the S₀→S₁ vertical excitation of the ground-state equilibrium structure (structure G1-[1]). However, the S₀ and S₁ potential energy curves in Fig. 3(b) reveal an alternative path. Specifically, before S₀→S₁ vertical excitation, a precursor for C-O dissociation can be generated by thermal excitation to a different Franck-Condon region in the S₀ state ($\Delta H^\ddagger = 45$ kJ/mol): structure G3-[2][‡] with $R_{C(1)-O(5)} = 1.60$ Å (at the threshold distance) and a Gibbs free energy barrier ΔG^\ddagger of 50 kJ/mol at 1200 K (Table S6[†]). The precursor structure G3-[2][‡] undergoes S₀→S₁ vertical excitation ($E_{\text{ex}} = 6.31$ eV (196 nm)) to the transition structure E3-[2][‡], which then spontaneously dissociates on the barrierless S₁ potential energy curve into the products [CH₃][•] and [OH][•] at the intersection of the S₀ and S₁ states, structure E3-[3][‡] (Table S7[†], $\Delta H_{\text{ex}}^\ddagger = -1.65$ and $\Delta G_{\text{ex}}^\ddagger = -1.73$ kJ/mol at 1200 K).

This mechanism is different from that reported in Ref. [8], in which the freeze-scan method simulation led to the conclusion that C-O dissociation occurs through vertical excitation of the CH₃OH equilibrium structure in the S₀ state, and that C-O bond cleavage takes place with a "low" energy barrier to avoid crossing between the respective Rydberg and valence electronic configurations. In our opinion, this pathway is not reasonable, because S₀→S₁ vertical excitation of the CH₃OH equilibrium structure would lead to predominance of O-H dissociation unless another precursor outside the Franck-Condon region of the ground state equilibrium geometry were photoexcited.

Our proposed mechanism supports the results of the laser-induced fluorescence experiment at 193 nm,⁷ which showed that C-O dissociation in channel (3) is a minor process and that thermal excitation of the CH₃O mode prior to S₀→S₁ excitation (e.g., $\Delta H^\ddagger = 45$ kJ/mol in Table S6[†])

increases the quantum yield for the dissociation of C-O into [CH₃][•] and [OH][•].¹⁰ Our theoretical results suggest that the branching ratio for channel (3) might increase due to growth of the population of the precursor in the electronic ground state (structure G3-[2][‡]) upon thermal (vibrational) excitation prior to photoexcitation. The suggestion that the thermal excitation leads to an increase in the yield of the products [CH₃][•] and [OH][•] is also in accordance with the state-selective laser photofragment spectroscopy results in Ref. [9].

The values of the CI coefficients in the S₀ and S₁ states in Table S2[†] show the dependence of the electronic configurations on the C-O distance. As in the case of O-H dissociation, electronic configuration inversion occurs in the S₀ state when the structure G3-[1][‡] is transformed into structures G3-[2][‡] and G3-[3][‡] (the products [CH₃][•] and [OH][•]). On the S₀ potential energy curve, the contribution of the electronic ground state Ψ_0 gradually decreases from $C_0 = 0.9830$ for structure G3-[1][‡] to $C_0 = 0.9781$ for structure G3-[2][‡]. Meanwhile, the contributions of the singly excited states associated with the excitation of an electron from the lone-pair natural orbital (Ψ_9^Z and Ψ_9^Y), increase from $C_9^Z = 0.0724$ for structure G3-[1][‡] to $C_9^Z = 0.0763$ for structure G3-[2][‡] and to $C_9^Y = 0.9929$ for the C-O dissociated structure G3-[3][‡]. The electronic configuration inversion $\Psi_0 \rightarrow \Psi_9^Y$ in the S₀ state leads to a substantial increase in the total energy and eventually to the intersection of the S₀ and S₁ states at long C-O distances. This finding explains why C-O dissociation in the S₀ state involves a rather high energy barrier ($\Delta E^\ddagger = 42.3$ kJ/mol).

In the S₁ state, while the singly excited configuration Ψ_9^Y dominates for the vertically excited and transition structures, i.e., structures E3-[1][‡] and E3-[2][‡] with $C_9^Y = 0.9849$ and 0.9803 , respectively, the contribution of the electronic configuration associated with the excitation of an electron out of the HOMO-1 natural orbital (Ψ_8^Y) is most notable for the C-O dissociated structure E3-[3][‡] with $C_8^Y = 0.9877$. Although the electronic configuration inversion in the S₁ state occurs between the singly excited configurations $\Psi_9^Y \rightarrow \Psi_8^Y$, the relaxation of structure E3-[2][‡] into structure E3-[3][‡] is barrierless. This is because the lone-pair natural orbitals of the oxygen atom ($n_{\text{orb}} = 8$ and 9) in the dissociated structure E3-[3][‡] are approximately degenerate. Therefore, in this case electronic configuration inversion does not lead to an increase in the total energy on the S₁ potential energy curve.

D. C-H dissociation

Although previous theoretical and experimental studies suggested that channel (2) was not important,^{8,17} to investigate possible unimolecular C–H dissociation and to confirm the results of our CASPT2(4,7) calculations, the S_1 potential energy curve with respect to the C–H distance was tentatively constructed by suppressing O–H dissociation ($R_{O(4)-H(6)} = 0.97$ Å). The outstanding features of the S_1 potential energy curve in Fig. 3(c) are the existence of a minimum at $R_{C(1)-H(4)} = 1.10$ Å (structure **E2-1I**) and of a transition structure in which the C–H bond breaks at $R_{C(1)-H(4)} = 1.50$ Å (structure **E2-2I**) with an energy barrier of $\Delta E^\ddagger = 146$ kJ/mol. The value of ΔE^\ddagger is the same as that obtained from *ab initio* MRD-CI calculations in Ref. [8].

Unimolecular C–H dissociation into the products $[\text{CH}_2\text{OH}]^\cdot$ and $[\text{H}]^\cdot$ in their respective ground states via the $S_0 \rightarrow S_1$ vertical excitation of structure **G2-2I**[†] does not seem to be feasible due to the lack of an intersection between the S_0 and S_1 potential energy curves at long C–H distances. To confirm this, CASPT2(4,7) geometry optimizations without geometry constraints were performed on structure **E2-2I**[†] starting from $R_{C(1)-H(4)} = 1.55$ Å. Structure **E2-2I**[†] appears to relax along the O–H dissociation path, resulting in structure **E1-3I**[‡]. This finding is in line with the reported experimental and theoretical studies,^{8,17} which suggested that $[\text{CH}_2\text{OH}]^\cdot$ is preferentially formed via a bimolecular reaction, e.g., from $[\text{CH}_3\text{O}]^\cdot$ and CH_3OH ,⁴² or by the isomerization of $[\text{CH}_3\text{O}]^\cdot$ in the presence of catalysts.³⁹

Analysis of the electronic configurations in Table S3[†] reveals different trends in the CI coefficients as a function of the C–H coordinate compared with those of the O–H and C–O dissociation. In this case, the leading CI coefficients do not significantly change upon C–H dissociation in the S_0 and S_1 states characterized by Ψ_0 and Ψ_1^{IV} , respectively. In the S_0 state, C_0 decreases gradually from 0.9830 for structure **G2-1I** to 0.9753 for structure **G2-2I**[†] and to 0.9553 for the C–H dissociated structure **G2-3I**. In the S_1 state, C_0^{IV} decreases from 0.9850 for structure **E2-1I**[†] to 0.9758 for structure **E2-2I**[†] and to 0.9669 for the C–H dissociated structure **E2-3I**. The lack of electronic configuration inversion, especially in the S_0 state, makes the intersection of the S_0 and S_1 potential energy curves at long C–H distances unlikely and confirms that unimolecular photodissociation of the C–H bond of CH_3OH into $[\text{CH}_2\text{OH}]^\cdot$ and $[\text{H}]^\cdot$ in their respective ground states is not feasible in the S_1 state.

E. Isomerization-mediated C–O dissociation

24

Although previous studies^{39,43} anticipated that the formation of $[\text{CH}_3]$ and $[\text{H}_2\text{O}]$ in the S_1 state would occur through bimolecular reactions and that the intramolecular isomerization of $[\text{CH}_3\text{O}]^\cdot$ would be enhanced by catalysts, the possibility of $[\text{CH}_3\text{OH}] \rightarrow [\text{CH}_2\text{OH}_2]$ isomerization within a single isolated molecule was of interest in this work. To study the formation of $[\text{CH}_3]$ and $[\text{H}_2\text{O}]$ in channel (4), an isomerization-mediated C–O dissociation potential energy curve was constructed by constraining the O–H distance at $R_{O-H} = 0.97$ Å. The $[\text{CH}_3\text{OH}] \rightarrow [\text{CH}_2\text{OH}_2]$ isomerization was simulated by transferring one of the H atoms ($H(4)$) from the CH_3 group to the OH group. The S_1 potential energy curve with respect to the $H(4)-O(5)$ coordinate in Fig. 4(a) reveals that intramolecular isomerization initially leads to the transition structure **E4-2I**[†] with $R_{H(4)-O(5)} = 1.60$ Å and $\Delta E^\ddagger = 92$ kJ/mol, followed by homolytic cleavage of the C–O bond and formation of the $[\text{CH}_3]^\cdot$ –[OH][•] H-bond structure **E4-3I** with $R_{H(4)-O(5)} = 1.58$ Å, $R_{C(1)-O(5)} = 2.64$ Å, and $E^{\text{Ex}} = 0.64$ eV (62 kJ/mol).

Similarly to in the case of C–O dissociation via channel (3), CASPT2(4,7) geometry optimizations without geometry constraints were performed on structure **E4-2I**[†] with $R_{H(4)-O(5)}$ slightly shifted to confirm that structure **E4-2I**[†] is the transition structure for $[\text{CH}_3\text{OH}] \rightarrow [\text{CH}_2\text{OH}_2]$ isomerization. Similar results were observed, namely, starting from structure **E4-2I**[†] with $R_{H(4)-O(5)} = 1.65$ Å, the CASPT2(4,7) geometrical optimizations yielded structure **E1-3I**[‡] (the O–H dissociated structure). When starting from structure **E4-2I**[†] with $R_{H(4)-O(5)} = 1.58$ Å, C–O dissociation and intermolecular proton transfer from $[\text{CH}_3]^\cdot$ to $[\text{OH}]^\cdot$ generate the $[\text{CH}_3] \rightarrow [\text{H}_2\text{O}]$ H-bond complex in the S_1 state, i.e., structure **E4-4I** in Fig. 4(b), with $E^{\text{Ex}} = 0.28$ eV (26 kJ/mol), $R_{C(1)-O(5)} = 3.26$, and $R_{C(1)-H(4)} = 2.30$ Å.

To investigate the nonradiative relaxation in channel (4) and verify the interaction energies of the H-bond complexes formed from $[\text{CH}_3]$ and $[\text{H}_2\text{O}]$ and from $[\text{CH}_3]$ and $[\text{H}_2\text{O}]$ obtained using single-point CCSD(T)-F12 and MRCI+Q calculations with the B3LYP-D3/aug-cc-pVTZ equilibrium structures,¹⁴ the $[\text{CH}_3] \rightarrow [\text{H}_2\text{O}]$ H-bond complex was fully optimized in the S_0 and T_1 states using the CASPT2(4,7) method. The results in Fig. 4(b) reveal that the C–H distances and the $\angle\text{HCH}$ angles in the optimized structures **G4-5I** and **3G4-5I** are in excellent agreement with those obtained experimentally,^{44,45} but the H-bond distances are systematically shorter than those used in the single-point single-reference CCSD(T)-F12/avg-cc-pVDZ/B3LYP-D3/avg-cc-pVTZ

25

calculations.¹⁴ This difference was particularly notable in the S_0 state, where $\Delta R_{C(1)-O(5)} = 0.16 \text{ \AA}$.¹⁴ The H-bond interaction energies (ΔE^{HB}) of structures **G4-[5]** and **³G4-[5]** are -33.0 and -5.5 kJ/mol, respectively, with a singlet-triplet energy gap of $\Delta E^{\text{ST}} = 30 \text{ kJ/mol}$. The values of ΔE^{HB} obtained from the fully optimized structures are lower, whereas the ΔE^{ST} value is higher than those obtained from single-point single-reference CCSD(T)-F12/avg-cc-pVDZ/BS3LYP-D3/avg-cc-pVTZ calculations.¹⁴ In Ref. [14], the ΔE^{HB} values in the S_0 and T_1 states were -13.9 and -2.3 kJ/mol, respectively, with an ΔE^{ST} of 27.4 kJ/mol. In addition, analysis of the CI coefficients in Fig. 4(b) suggests that the neglect of the multiconfigurational character of the wavefunctions in Ref. [14] could also lead to discrepancies in ΔE^{HB} and ΔE^{ST} , especially in the S_0 state. For structure **G4-[5]**, the doubly excited configuration ($\Psi_{9,9}^{10,10}$), which is characteristic of the singlet carbene ($^1[\text{CH}_2]$), contributes approximately 15% of the closed-shell electronic ground-state configuration Ψ_0 .

These results and the fact that the S_1 potential energy curve in Fig. 4(a) was computed by constraining the O-H distance at $R_{O-H} = 0.97 \text{ \AA}$ lead to the conclusion that the intramolecular isomerization-mediated C-O dissociation in channel (4) can occur when the equilibrium structure in the electronic ground state (structure **G1-[1]**) is thermally excited to structure **G4-[2][†]** ($\Delta H^\ddagger = 106 \text{ kJ/mol}$, Table S8[†]). Structure **G4-[2][†]** then undergoes $S_0 \rightarrow S_1$ vertical excitation ($E^{\text{ex}} = 6.47 \text{ eV}$ or 192 nm) to the transition structure **E4-[2][‡]**, which is exothermically ($\Delta H^{\text{ex}} = -277 \text{ kJ/mol}$) transformed into the $[\text{CH}_2]\text{-}[\text{H}_2\text{O}]$ H-bond complex in the S_1 state (structures **E4-[3]** and **E4-[4]** in Fig. 4(b), respectively). Due to the small energy gap between the total energies (only 26.0 kJ/mol, nonradiative relaxation of structure **E4-[4]** to **G4-[4]** is likely possible, and the relaxation of structure **G4-[4]** to **G4-[5]** is anticipated to be an exothermic process).

The trends of the CI coefficients in Table S4[†] confirm the role of electronic configuration inversion. In the S_0 state, the electronic configuration inversion $\Psi_0 \rightarrow \Psi_8^0$ increases the total energy on the $[\text{CH}_3\text{OH}]\text{-}[\text{CH}_2\text{OH}_2]$ isomerization potential energy curve (structure **G4-[2][†]** to **G4-[3]**), leading to a decrease in the energy gap between the S_0 and S_1 states. The energy gap between structures **E4-[3]** and **G4-[3]** is 62 kJ/mol, and the threshold distance for the electronic configuration inversion $R_{H(4)-O(5)}$ is 1.60 Å. Although both channels (3) and (4) involve C-O bond cleavage, the CI coefficients in Table S2[†] and Fig. 4(b) reveal the different characteristic electronic

states of the products. In channel (3), structure **G3-[3][‡]** is dominated by the singly excited state Ψ_6^0 with $C_{9,9}^{10} = 0.9929$, confirming that the homolytic cleavage of the C-O bond leads to the $[\text{CH}_3]^\cdot$ and $[\text{OH}]^\cdot$ radicals, represented by one outstanding S-type configuration with two open shells (Ψ_9^{10}). In channel (4), the $^1[\text{CH}_2]\text{-}[\text{H}_2\text{O}]$ H-bond complex (structure **G4-[5]**) is characterized by the electronic ground state Ψ_0 with $C_0 = 0.9748$ and a small contribution of the electronic configuration of the singlet methylene, the doubly excited state $\Psi_{9,9}^{10,10}$ with $C_{9,9}^{10,10} = 0.1582$. In contrast, the $^3[\text{CH}_2]\text{-}[\text{H}_2\text{O}]$ H-bond complex (structure **³G4-[5]**) is characterized by the open-shell configuration Ψ_9^{10} with $C_9^{10} = 0.9992$, which is characteristic of triplet methylene.

F. Rotationally mediated C-H dissociation

Formaldehyde could potentially be formed through various radical reactions, e.g., the bimolecular reaction between $[\text{CH}_2\text{OH}]^\cdot$ or $[\text{CH}_3\text{O}]^\cdot$ and O_2 ,⁴ as well as C-H dissociation of $[\text{CH}_3\text{O}]^\cdot$.¹² In this work, we were interested in the possibility of generating formaldehyde directly from the single isolated CH_3OH molecule. The freeze-scan potential energy curve in the lowest singlet-excited state obtained from *ab initio* MRD-CI calculations⁸ showed a low energy barrier for H₂ elimination (approximately 52 kJ/mol). However, the S_0 and S_1 potential energy curves for the dehydrogenation did not intersect at large CH_2O and H_2 separations; thus, the high percentages of CH_2O and H_2 in their respective electronic ground states observed in the experiment cannot be explained. The energy gap between the S_0 and S_1 states at $R = 3 \text{ \AA}$ was 262 kJ/mol.⁸ The lack of the intersection of the S_0 and S_1 states implied that the CH_2O and H_2 products are still in the electronic excited state. This could be due to the freeze-scan method and the degrees of freedom chosen in the calculations of the S_0 and S_1 potential energy curves. In Ref. [8], the dehydrogenation was hypothesized to occur through a concerted reaction in which the hydrogen atom of the OH group and one hydrogen atom of the CH_3 group were coplanar and left the CH_2O moiety at the same rate.

Based on the observation that O-H dissociation is the most favorable process in the S_1 state and the anticipation that H₂ elimination involves a two-step nonconcerted mechanism,⁸ formaldehyde formation in this work was hypothesized occur from the O-H dissociated structure **E1-[3][‡]**. To search for an appropriate precursor, the S_1 and S_0 potential energy curves with respect to the C-O rotation were constructed for structure **E1-[3][‡]**. Starting from structure **E1-[3][‡]**, the variation of the

dihedral angle $\angle\text{H}_{(9)}\text{C}_{(10)}\text{O}_{(5)}\text{H}_{(6)}$ from 180 to 120 degrees yielded structure **E1-[4][‡]**, in which two hydrogen atoms ($\text{H}_{(6)}$ of the OH group and $\text{H}_{(9)}$ of the CH_3 group) are coplanar. This process was barrierless in both the S_1 and S_0 states; e.g., in the S_1 state, ΔE^\ddagger is 0.27 kJ/mol and E^{Ex} is 0.01 eV. The S_1 and S_0 potential energy curves for the dehydrogenation were then constructed from structure **E1-[4][‡]** by varying the $\text{H}_{(9)}\text{-H}_{(6)}$ distance from 2.66–0.73 Å.

The S_0 and S_1 potential energy curves in Fig. 5 suggest two possibilities for formaldehyde formation through H_2 elimination: Formation in the S_1 state through the transition structure **E5-[2][‡]** with $\Delta E^\ddagger = 53$, $\Delta H^\ddagger = 14$, and $\Delta G^\ddagger = 109$ kJ/mol at 1200 K (Table S9[†]), or in the S_0 state through the transition structure **G5-[1][‡]** with $\Delta E^\ddagger = 6.29$ kJ/mol. Since the precursor (structure **E1-[4][‡]**) is energetically at the intersection of the S_1 and S_0 states ($E^{\text{Ex}} = 0.01$ eV) and the formation of the transition structure **G5-[1][‡]** involves a very low energy barrier, the reaction is anticipated to occur more preferentially and spontaneously in the S_0 state through an exothermic process with $\Delta H^{\text{Ex}} = -317$ and $\Delta G^{\text{Ex}} = -493$ kJ/mol at 1200 K (Table S8[†]). These results confirm that formaldehyde formation is a two-step nonconcerted process and explain why the formation of formaldehyde and H_2 in their respective electronic ground states is the second most-preferred reaction. The proposed elementary processes are different from that in Ref. [8]; in the present work, the H_2 elimination takes place preferentially on the S_0 potential energy curve with a barrierless potential ($\Delta E^\ddagger = 6$ kJ/mol), whereas in Ref. [8], the reaction occurred in the S_1 state (without the intersection of the S_0 and S_1 state) and involved an ΔE^\ddagger value of 52 kJ/mol.

Analysis of the electronic configurations and CI coefficients of the structures on the S_0 and S_1 potential energy curves in Table S5[†] confirmed the role of electronic configuration inversion. In this case, the transformation of structure **E1-[4][‡]** into **G5-[3]** (CH_2O and H_2 molecules) is more favorable on the S_0 potential energy curve because in this case, the electronic configuration inversion involves the inversion of the higher-energy singlet electronic state Ψ_8^0 to the lower-energy electronic ground state Ψ_0 .

G. Interplay between thermal excitation and photoexcitation

Based on the discussion of the structures and energetics, as well as the electronic configurations of the S_0 and S_1 potential energy curves, the photodissociation mechanisms for CH_3OH in the S_1

state are summarized in Fig. 6. The $\text{S}_0\text{-S}_1$ vertical excitation energies (E^{Ex}) are approximately the same, and the thermally excited structures in the S_0 state are the precursors for the formation of the transition structures in the S_1 state and the products in their respective electronic ground states. From this, it can be concluded that thermal excitation in the electronic ground state plays the most important role in determining the photodissociation *via* channels (3) and (4). Figure 6 and the normalized oscillator strengths in Table S10[†] illustrate that in photodissociation *via* channels (3) and (4), photons with approximately the same energy as those in channel (1), i.e., 6.3–6.5 eV or 192–196 nm, could generate the transition structures in the S_1 state from the thermally excited precursors in the S_0 state. In other words, the photodissociation processes of CH_3OH in the S_1 state are thermally determined.

Because our model calculations took the effects of thermal energy into account for the first time, it is reasonable to connect the theoretical results with experimental data. Previous theoretical studies discussed experimental data solely on the basis of the potential energy curves obtained from quantum chemical methods.^{8,10,18,46} Consideration of the effects of thermal energy is crucial, especially when the exothermicity of C–O and O–H dissociation is compared.⁸ The S_0 potential energy curves obtained from *ab initio* MRD-CI calculations showed that the C–O bond is 109 kJ/mol weaker than the O–H bond. Based on this, the exothermicity ($|\Delta E^{\text{Ex}}|$) of the photolysis of the C–O bond with respect to the vertically excited structure (e.g., structure **E1-[1][‡]**) was anticipated to be significantly higher than that of the O–H bond.⁸ In this work, although our S_0 and S_1 potential energy curves suggested a similar result (Table S7[†], $|\Delta E^{\text{Ex}}| = 227$ and 190 kJ/mol, respectively), the TST calculations revealed that O–H dissociation is approximately 24 kJ/mol more exothermic than C–O dissociation ($|\Delta H^{\text{Ex}}| = 189$ and 165 kJ/mol, respectively). It should be emphasized that based on our relax-scan potential energy curves, C–O dissociation cannot proceed directly through the vertical excitation of the equilibrium structure in the electronic ground state.

Extensive discussion of the kinetics of the photodissociation reactions cannot be provided in this work because the experimental data for CH_3OH are limited, especially for unimolecular photodissociation processes (first-order reactions); the reported experimental kinetic data involve mostly bimolecular processes (second-order reaction).^{7,8,47} Because the preexponential factor (vibrational frequency) in the Arrhenius equation does not change significantly with temperature and atomic vibrations generally have a period of 0.1–1.0 ps,³² the preexponential factor could be

approximated as 10^{12} – 10^{13} vibrations per second. This value is in agreement with the O–H dissociation time of less than 1 ps estimated based on the spatial anisotropy of the fragments.²⁹ Therefore, the rate constant for the barrierless O–H dissociation pathway ($\Delta E^\ddagger = 0$ kJ/mol) can be roughly estimated as $k = 1.0 \times 10^{12}$ – 1.0×10^{13} s⁻¹,³² those of the barrierless elementary reactions to generate methyl mercaptan (CH₃SH) from interstellar carbon monosulfide (CS) were also approximated to be 1.0×10^{12} s⁻¹.⁴⁸

The rate determining process for C–O dissociation proposed in this work is the formation of the precursor (structure G3-[2][†]) in the S₀ state with $k^{\text{Q-vib}} = 1.65 \times 10^{11}$ s⁻¹ at 1200 K. Thus, O–H dissociation is more than six times faster (kinetically controlled) than C–O dissociation, which is in reasonable agreement with the values (O–H dissociation five times faster than that of C–O) predicted based on a simple classical model and the ratios of the light and heavy fragmented products in these two dissociation channels.⁸ Likewise, using the same approximation and the value of the rate constant for the generation of the precursor in the S₀ state (structure G4-[2][†] with $k^{\text{Q-vib}} = 2.16 \times 10^8$ s⁻¹ at 1200 K), O–H dissociation is more than 4,000 times faster than [CH₃OH]–[CH₂OH] isomerization dissociation. This, along with the finding that the formation of structure G4-[2][†] in the electronic ground state is an endothermic process that requires a rather high thermal energy ($\Delta H^\ddagger = 106$ kJ/mol), confirms that unimolecular isomerization-mediated C–O dissociation is not preferred for CH₃OH.

Finally, because O–H dissociation is barrierless in the S₁ state and the formation of CH₃O and H₂ involves a low energy barrier in the S₁ state or no barrier in the S₀ state, the photodissociation reactions in channels (1) and (5) are strongly kinetic controlled, and the fast photoexcitation process (on the femtosecond time scale) prohibits the formation of the precursors in the S₀ state for the dissociations in channels (3) and (4). This could be the main reason why only the unimolecular dissociations in channels (1) and (5) were observed experimentally.

IV. CONCLUSIONS

In this work, the mechanisms of the photodissociation reactions of a single-isolated CH₃OH in the lowest singlet-excited (S₁) state were systematically studied using the CASPT2 method with the aug-cc-pVDZ basis set and the transition state theory (TST). The theoretical study considered

FIG. 6. Mechanisms of the unimolecular photodissociations of CH₃OH obtained from the analysis of the S₀ and S₁ potential energy curves. Energies are in kJ/mol and the relative energies are with respect to structure G1-[1]. $\Delta G^{\ddagger \text{rel}}$ = relative Gibbs free energy at 1200 K; $\Delta H^{\ddagger \text{rel}}$ = reaction enthalpy; ΔG^\ddagger = relative Gibbs free energy for formation of transition structure at 1200 K; ΔH^\ddagger = enthalpy of activation; $k^{\text{Q-vib}}$ = rate constant with quantized vibrations at 1200 K; [†] = transition structure and [‡] = structure at the intersection of the S₀ and S₁ potential energy curves. a) Channels (1)–(3). b) Channel (4). c) Channel (5).

single-photon photodissociation in the five proposed channels, with an emphasis on nonradiative relaxation processes that transform the S_0 - S_1 vertically excited structures into the products in electronic ground states, and on the interplay between thermal excitation and photoexcitation. The kinetic and thermodynamic aspects of the elementary reactions, which have not been included in previous theoretical models, were discussed in connection to the available experimental data. Thus, the five main objectives listed at the end of the introduction have all been achieved, and the results for each can be summarized as follows:

(1)-(2) S_1 relax-scan potential energy curves and TST calculations confirmed that O-H dissociation is the predominant exothermic process, whereas the formation of formaldehyde (CH_2O) and hydrogen (H_2) molecules, in which the O-H dissociated species becomes the precursor in the S_0 state, is the second most-favorable process. For C-O dissociation, the relax-scan potential energy curves suggested a thermally excited precursor ($\Delta H^\ddagger = 45 \text{ kJ/mol}$) in a different Franck-Condon region in the S_0 state, whose S_0 - S_1 vertical excitation leads to a transition structure and spontaneous formation of the $[\text{CH}_3]^\ddagger$ and $[\text{OH}]^\ddagger$ products in their respective electronic ground states *via* an exothermic process ($\Delta H^{\text{rel}} = -165 \text{ kJ/mol}$): S_0 - S_1 vertical excitation at the same excitation wavelength (196 nm) could lead spontaneously to direct C-O dissociation in the S_1 state on a "barrierless" potential energy curve. The CASPT2 and TST results revealed a possibility for $[\text{CH}_3\text{OH}]-[\text{CH}_2\text{OH}_2]$ isomerization dissociation in which another thermally excited precursor ($\Delta H^\ddagger = 106 \text{ kJ/mol}$) is vertically excited to generate a transition structure in the S_1 state. C-O dissociation and intermolecular proton transfer from $[\text{CH}_3]^\ddagger$ to $[\text{OH}]^\ddagger$ then lead to the products $[\text{CH}_2]$ and $[\text{H}_2\text{O}]$.

(3) The CASPT2 potential energy curves obtained based on the relax-scan method revealed that C-O dissociation in the S_1 state is not feasible in the Franck-Condon region of the CH_3OH equilibrium structure in the S_0 state because of the predominance of O-H dissociation in the S_1 state. Based on the hypothesis that the O-H dissociated structure is the precursor for the second most-favorable process, the relax-scan potential energy curves revealed an intersection of the S_0 and S_1 states. This indicates that the formation of CH_2O and H_2 is a non-radiative process without surface hopping effects. These results are different from those obtained based on the freeze-scan MRD-CI method, in which C-O dissociation was anticipated to occur through the vertical excitation of the CH_3OH equilibrium structure in the electronic ground state, and surface hopping

effects are an important relaxation processes to bring CH_2O and H_2 to their respective electronic ground states.⁹

(4) According to the TST results, the elementary reactions to generate the precursors in the electronic ground state are thermodynamically and kinetically feasible at high temperatures. However, the stronger kinetic-control character of O-H dissociation dominates the C-O and $[\text{CH}_3\text{OH}]-[\text{CH}_2\text{OH}_2]$ isomerization dissociations; O-H dissociation and the formation of CH_2O and H_2 are both more thermodynamically and kinetically favorable than these two dissociation reactions. These kinetic and thermodynamic results explain why the products of the former two unimolecular processes have rarely been found in experiments.

(5) Analysis of the electronic configurations and CI coefficients suggested that the precursors and transition structures for the photodissociation reactions are characterized by threshold structural parameters and electronic configuration inversions in the S_0 state, which lead to the intersection of the S_0 and S_1 potential energy curves and the products in their respective electronic ground states. C-H dissociation, which generates $[\text{CH}_2\text{OH}]^\ddagger$ and $[\text{H}]^\ddagger$, is unlikely to be unimolecular because of the lack of the electronic configuration inversion and the intersection of the S_0 and S_1 potential energy curves.

The present CASPT2 results verified and confirmed the reported theoretical and experimental findings, as well as showing as an example how the multiconfigurational characters change in covalent bond dissociation processes, which could be further studied in theories and experiments.

SUPPLEMENTARY MATERIAL

See the supplementary material for the characteristic structures and energetic on the potential energy curves and for the thermodynamic and kinetic data associated to the results reported in the main text.

ACKNOWLEDGMENTS

The authors would like to acknowledge the financial support provided by the Royal Golden Jubilee (RGJ) Ph.D. Program of the Thailand Research Fund (TRF) (Grant No. PHD/0139/2554) to Pannipa Panjapo and Prof. Kritsana Sagarik and the Advanced Research Scholarship (Grant No. BRG-5580011) to Prof. Kritsana Sagarik. Kitiapan Siwawampong would like to acknowledge the financial support provided by the Development and Promotion of Science and Technology Talents Project (DPST). The high-performance computer facilities provided by the following organizations are gratefully acknowledged: School of Mathematics and School of Chemistry, SUT, the National e-Science project of the National Electronics and Computer Technology Centre (NECTEC), and the National Science and Technology Development Agency (NSTDA). This work was supported in part by the Higher Education Research Promotion and National Research University (HERP-NRU) Project of the Office of the Higher Education Commission (OHEC), Thailand.

DATA AVAILABILITY

The data that support the findings of this study are available within the article and its supplementary material.

References

- 1 J. H. Seinfeld and S. N. Pandis, *Atmospheric Chemistry and Physics: From Air Pollution to Climate Change*, John Wiley & Sons, Inc., Hoboken, New Jersey, 3rd edn, 2016.
- 2 L. Gonzalez, D. Escudero and L. Serrano-Andres, *ChemPhysChem*, 2012, **13**, 28-51.
- 3 A. Gilbert, *Photochemistry*, The Royal Society of Chemistry, Atheneum Press Ltd, Gateshead, Tyne & Wear, 2002.
- 4 A. R. Ravishankara, *Atmos. Rev. Phys. Chem.*, 1988, **39**, 367-394.
- 5 C. V. Sonntag and H.-P. Schuchmann, *Adv. Photochem.*, 1977, **10**, 59.
- 6 S. Saebo, L. Raddom and H. F. Schaefer III, *J. Chem. Phys.*, 1983, **78**, 845-853.
- 7 S. Satyapal, J. Park, R. Bersohn and B. Katz, *J. Chem. Phys.*, 1989, **91**, 6873.
- 8 R. J. Buenker, G. Olbrich, H. P. Schuchmann, B. L. Schuermann and C. V. Sonntag, *J. Am. Chem. Soc.*, 1984, **106**, 4362-4368.
- R. Schmiedl, U. Meier and K. H. Welge, *Chem. Phys. Lett.*, 1981, **80**, 495-498.
- C. C. Marston, K. Weide, R. Schimke and H. U. Suter, *J. Chem. Phys.*, 1993, **98**, 4718.
- Z. Chen, A. T. J. B. Eppink, B. Jiang, G. C. Groenenboom, X. Yang and D. H. Parker, *Phys. Chem. Chem. Phys.*, 2011, **13**, 2350-2355.
- R. P. Porter and W. A. Noyes Jr., *J. Am. Chem. Soc.*, 1959, **81**, 2307-2311.
- F. Patat and H. Koch, *Z. Elektrochem.*, 1935, **41**, 494.
- J. M. Standard, *J. Phys. Chem. A*, 2016, **121**, 381-393.
- K. Andersson, P.-Å. Mahmqvist and B. O. Roos, *J. Chem. Phys.*, 1992, **96**, 1218.
- M. Schreiber, M. R. Silva-Junior, S. P. A. Sauer and W. Thiel, *J. Chem. Phys.*, 2008, **128**, 134110.
- E. Kassab, J. T. Gleghorn and E. M. Evleth, *J. Am. Chem. Soc.*, 1983, **105**, 1746-1753.
- B.-M. Cheng, M. Bahou, W.-C. Chen, C.-H. Yui, Y.-P. Lee and L. C. Lee, *J. Chem. Phys.*, 2002, **117**, 1633-1640.
- P. Suwannakham, S. Chaiwongwatana and K. Sagarik, *RSC Advances*, 2018, **8**, 36731-36744.
- W. R. Wadt and W. A. Goddard III, *Chem. Phys.*, 1976, **18**, 1-11.
- H.-J. Werner, P. J. Knowles, G. Knizia, F. R. Manby and M. Schütz, *WIREs Comput Mol Sci*, 2012, **2**, 242-253.
- MOLPRO, version 2015.1, a package of *ab initio* programs, H.-J. Werner, P. J. Knowles, G. Knizia, F. R. Manby, M. Schütz and others, 2015; available from <http://www.molpro.net>.
- P. J. Knowles and H.-J. Werner, *Chem. Phys. Lett.*, 1985, **115**, 259-267.
- H.-J. Werner and P. J. Knowles, *J. Chem. Phys.*, 1985, **82**, 5053-5063.
- H.-J. Werner and W. Meyer, *J. Chem. Phys.*, 1980, **73**, 2342-2356.
- A. R. Allouche, *J. Comput. Chem.*, 2011, **32**, 174-182.
- F. Eckert, P. Pulay and H.-J. Werner, *J. Comput. Chem.*, 1997, **18**, 1473-1483.
- T. Hrenar, G. Rauhut, and H.-J. Werner, *J. Phys. Chem. A*, 2006, **110**, 2060-2064.
- Y. Wen, J. Segall, M. Dulligan and C. Wittig, *J. Chem. Phys.*, 1994, **101**, 5665-5671.
- P. Hänggi, P. Talkner and M. Borkovec, *Rev. Mod. Phys.*, 1990, **62**, 251.
- E. Pollak and P. Talkner, *Chaos*, 2005, **15**, 026116.

- 32 D. S. Sholl and J. A. Steckel, *Density Functional Theory: A Practical Introduction*, John Wiley & Sons, Inc., Hoboken, New Jersey, 2009.
- 33 J. E. House, *Principles of Chemical Kinetics, 2nd edn*, Elsevier, USA, 2007.
- 34 E. Wigner, *Z. Phys. Chem.*, 1932, **15**, 203-216.
- 35 C. Eckart, *Phys. Rev.*, 1930, **35**, 1303.
- 36 J. Kästner, J. M. Carr, T. W. Keal, W. Thiel, A. Wander and P. Sherwood, *J. Phys. Chem. A*, 2009, **113**, 11856-11865.
- 37 ChemShell, a Computational Chemistry Shell, see www.chemshell.org.
- 38 M. C. L. Gerry, R. M. Lees and G. Winnewisser, *J. Mol. Spectrosc.*, 1976, **61**, 231-242.
- 39 S. Sarkar, S. Mallik, D. Deepak, P. Kumar and B. Bandyopadhyay, *Phys. Chem. Chem. Phys.*, 2017, **19**, 27848-27858.
- 40 L. B. Harding, H. B. Schlegel, R. Krishnan and J. Pople, ed. D. G. Truhlar, *Potential energy surfaces and dynamics calculations: for chemical reactions and molecular energy transfer*, Plenum Press, New York, 1980, pp. 169-183.
- 41 J. Baker, V. Butcher, J. M. Dyke and A. Morris, *J. Chem. Soc. Faraday Trans.*, 1990, **86**, 3843-3851.
- 42 Y. Takezaki and C. Takeuchi, *J. Chem. Phys.*, 1954, **22**, 1527.
- 43 R. J. Buszek, A. Sinha and J. S. Francisco, *J. Am. Chem. Soc.*, 2011, **133**, 2013-2015.
- 44 P. R. Bunker and P. Jensen, *J. Chem. Phys.*, 1983, **79**, 1224.
- 45 P. Jensen, P. R. Bunker and A. R. Hoy, *J. Chem. Phys.*, 1982, **77**, 5370.
- 46 J. M. Hutchinson, R. J. Holiday, A. Bach, S. Hsieh and F. F. Crim, *J. Phys. Chem. A*, 2004, **108**, 8115-8118.
- 47 T. P. M. Goumans and J. Kästner, *J. Phys. Chem. A*, 2011, **115**, 10767-10774.
- 48 T. Lamberts, *A&A*, 2018, **615**, L2.

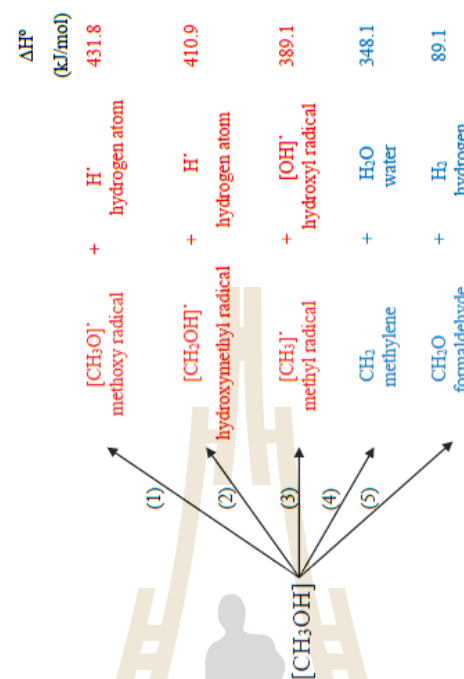


FIG. 1. Proposed dissociation channels for CH₃OH in the gas phase.^{6,7} ΔH° = standard dissociation enthalpy.

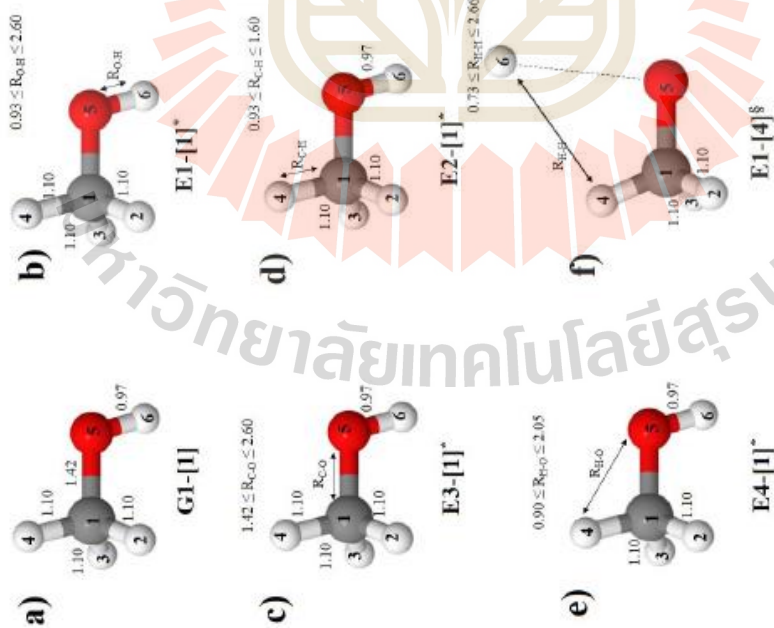


FIG. 2. a) Equilibrium structure of CH_3OH in the S_0 state obtained from CASPT2(4,7) geometry optimizations. b)-f) Constrained structural parameters used in the calculations of the S_1 relax-scan potential energy curves for dissociation channels (1)–(5), respectively. Double sided arrows represent the degrees of freedom used in the calculations of the S_1 relax-scan potential energy curves. Distances are in Å.

FIG. 3. a)-c) The potential energy curves with respect to the O-H, C-O and C-H coordinates obtained from the CASPT2(4,7)/aug-cc-pVDZ, CASPT2(14,12)/aug-cc-pVDZ and CCSD(T)/CBS methods. Solid lines represent the relax-scan potential energy curves. Dash lines denote the energies calculated using the geometries on the relax-scan potential energy curves. Relative energies (E^{rel}) and distances are in kJ/mol and Å, respectively. The values of the HOMO and LUMO isosurfaces are 0.11. $\text{Gr}_{(4,7)}$ and $\text{Ex}_{(4,7)}$ = relative energies obtained from CASPT2(4,7) calculations in the S_0 and S_1 states, respectively; $\text{Gr}_{(14,12)}$ and $\text{Ex}_{(14,12)}$ = relative energies obtained from CASPT2(14,12) calculations in the S_0 and S_1 states, respectively; $\text{Gr}_{\text{CCSD(T)}}$ = relative energies obtained from CCSD(T) calculations in the S_0 state; † = transition structure; ‡ = structure at the intersection of the S_0 and S_1 potential energy curves; and ΔE^{rel} and ΔE^\ddagger = energy release and barrier on the $\text{Ex}_{(4,7)}$ and $\text{Gr}_{(4,7)}$ potential energy curves, respectively.

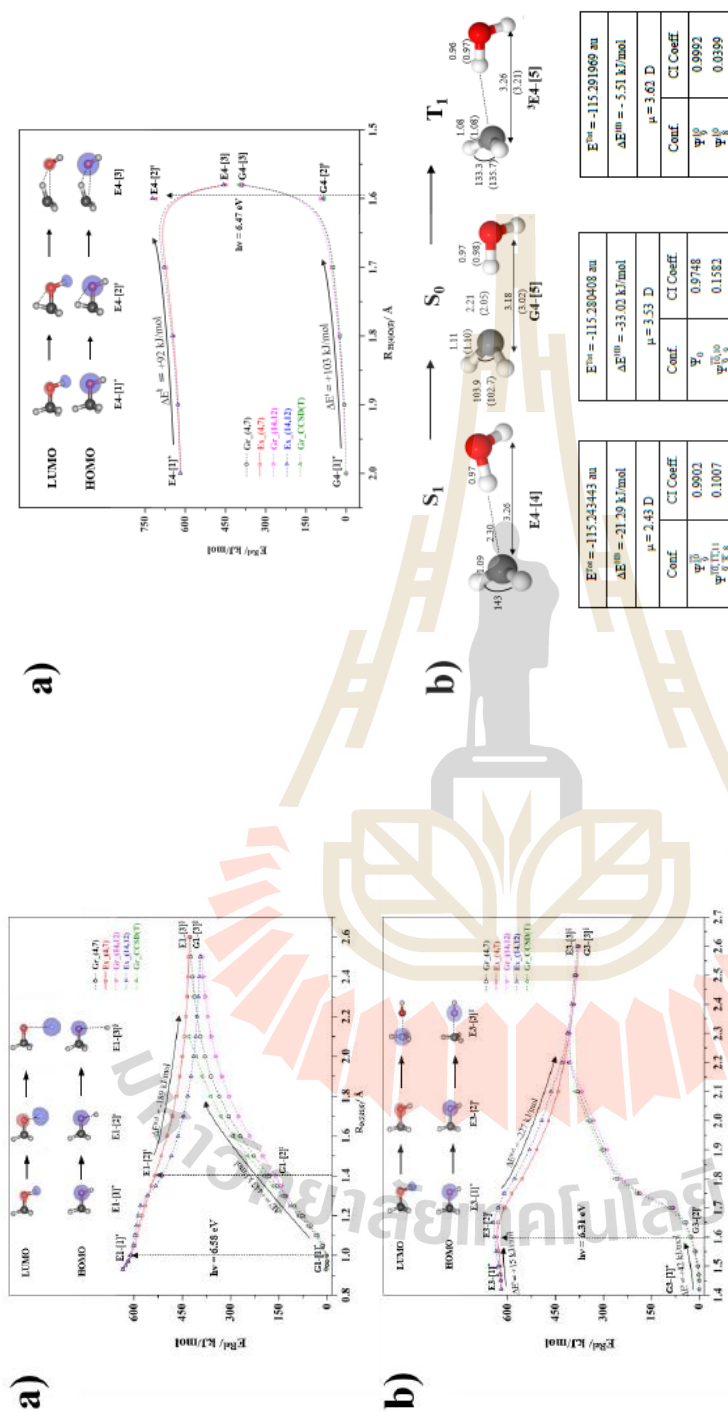


FIG. 4.

a) The potential energy curves for $[\text{CH}_3\text{OH}] \rightarrow [\text{CH}_3\text{OH}_2]$ isomerization obtained from the CASPT2(4,7)/aug-cc-pVDZ, CASPT2(14,12)/aug-cc-pVDZ and CCSD(T)/CBS methods. Solid line represents the relax-scan potential energy curve. Dash lines denote the energies calculated using the geometries on the relax-scan potential energy curve. Relative energies ($E_{rel}^{S_0}$) and distances are in kJ/mol and Å, respectively. The values of the HOMO and LUMO isosurfaces are 0.11. $\text{Gr}_-(4,7)$ and $\text{Ex}_-(4,7)$ = relative energies obtained from CASPT2(4,7) calculations in the S_0 and S_1 states, respectively; $\text{Gr}_-(14,12)$ and $\text{Ex}_-(14,12)$ = relative energies obtained from CASPT2(14,12) calculations in the S_0 state; † = transition structure; and ΔE^\ddagger = energy barriers on the $\text{Ex}_-(4,7)$ and $\text{Gr}_-(4,7)$ potential energy curves.

b) Equilibrium structures of the $[\text{CH}_3\text{OH} \cdots \text{H}_2\text{O}]$ H-bond complexes in the S_0 and T_1 states, obtained from CASPT2(4,7) calculations. The values in parentheses are the results reported in Ref. [20].

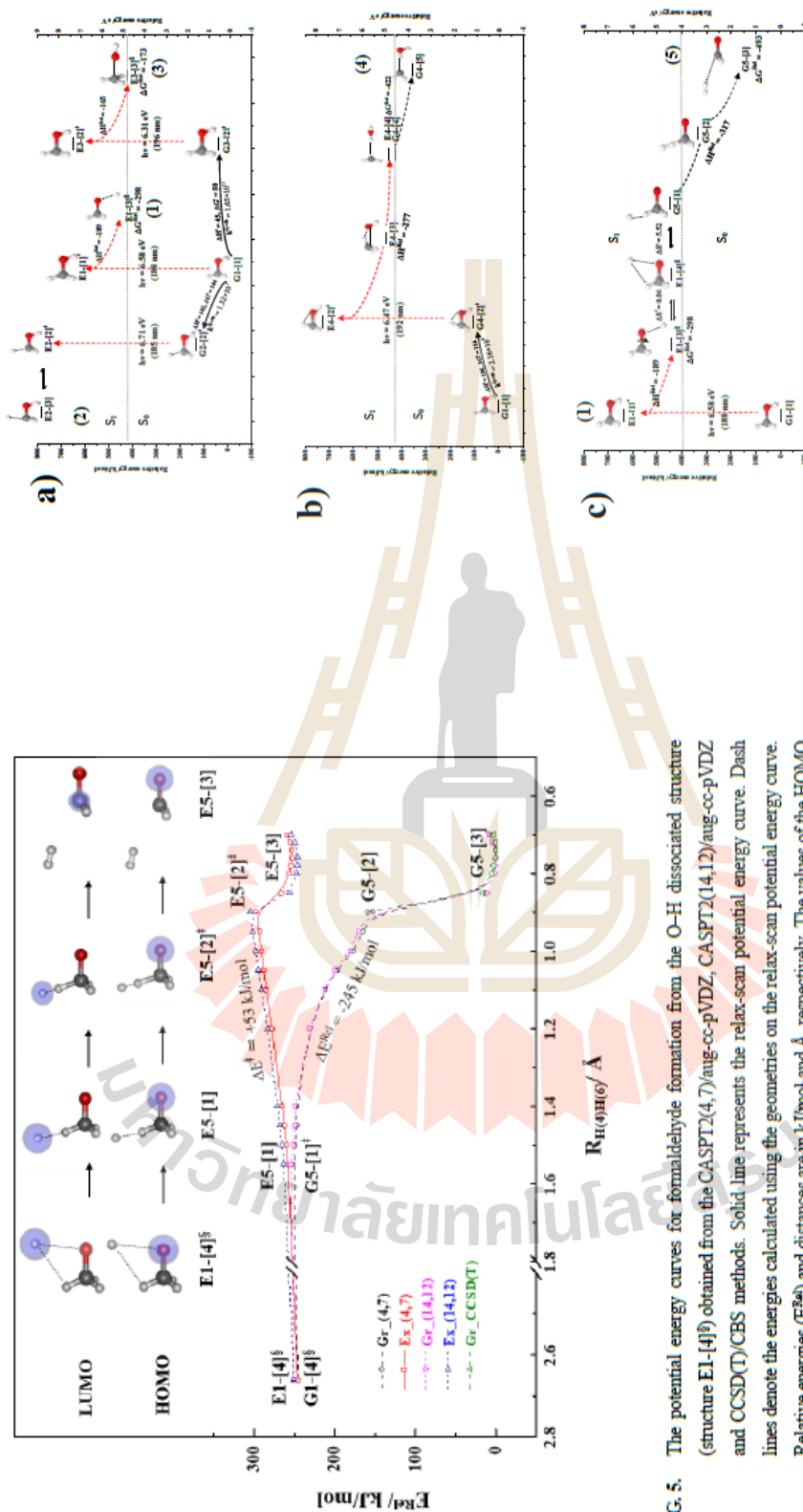


FIG. 5. The potential energy curves for formaldehyde formation from the O-H dissociated structure (structure E1-[4]‡) obtained from the CASPT2(4,7)/aug-cc-pVDZ, CASPT2(14,12)/aug-cc-pVDZ and CCSD(T)/CBS methods. Solid line represents the relax-scan potential energy curve. Dash lines denote the energies calculated using the geometries on the relax-scan potential energy curve. Relative energies (E^{\ddagger}) and distances are in kJ/mol and Å, respectively. The values of the HOMO and LUMO isosurfaces are 0.11. Gr_(4,7) and Ex_(4,7) = relative energies obtained from CASPT2(4,7) calculations in the S_0 and S_1 states, respectively; Gr_(14,12) and Ex_(14,12) = relative energies obtained from CASPT2(14,12) calculations in the S_0 and S_1 states, respectively; Gr_CCSDT = relative energies obtained from CCSD(T) calculations in the S_0 state; ‡ = transition structure; δ = structure at the intersection of the S_0 and S_1 potential energy curves; and ΔE^{\ddagger} and ΔE^0_0 = energy release and barrier on the Ex_(4,7) and Gr_(4,7) potential energy curves, respectively.

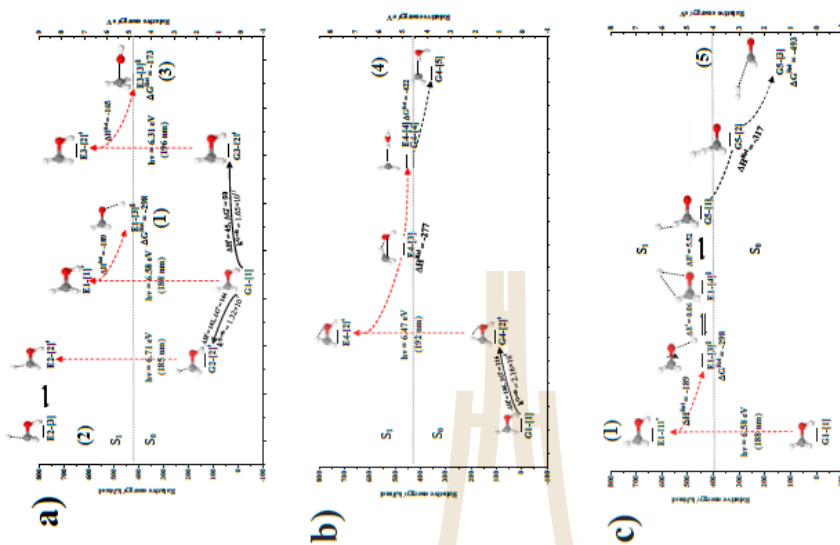
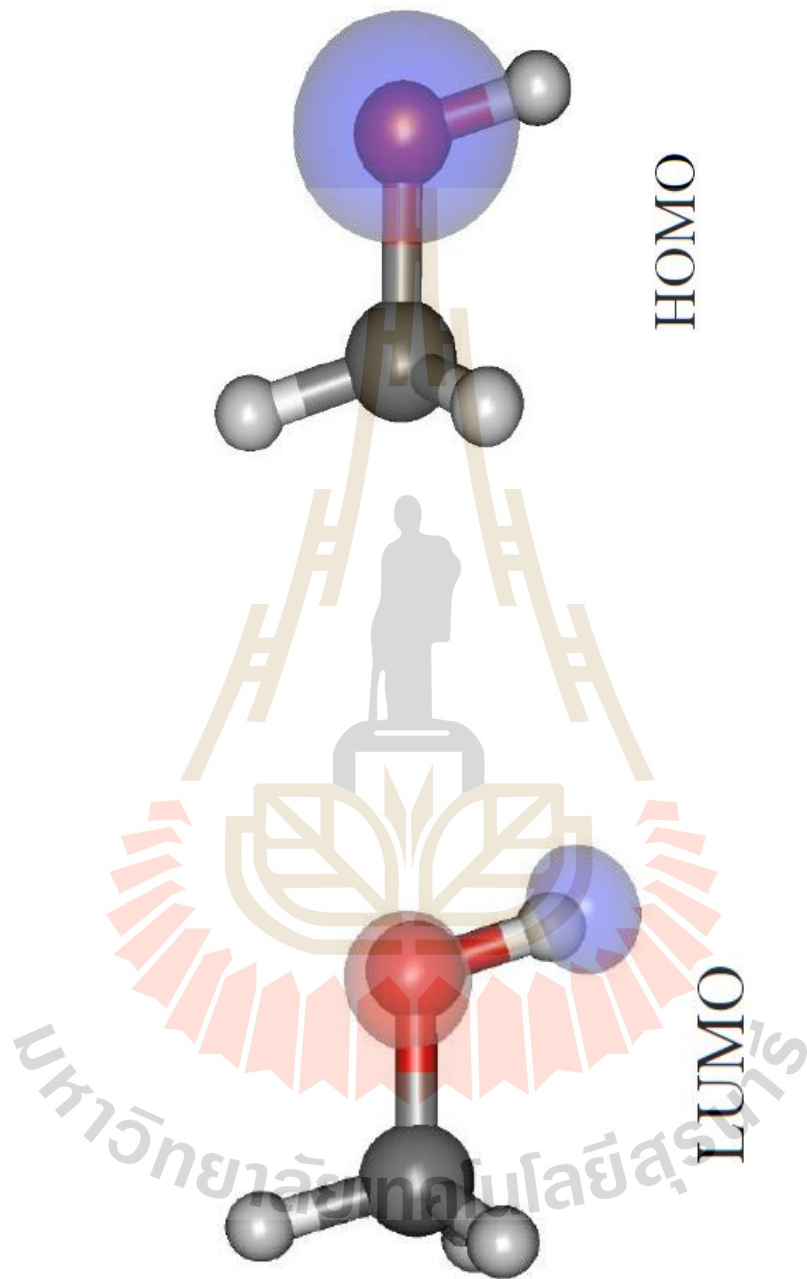
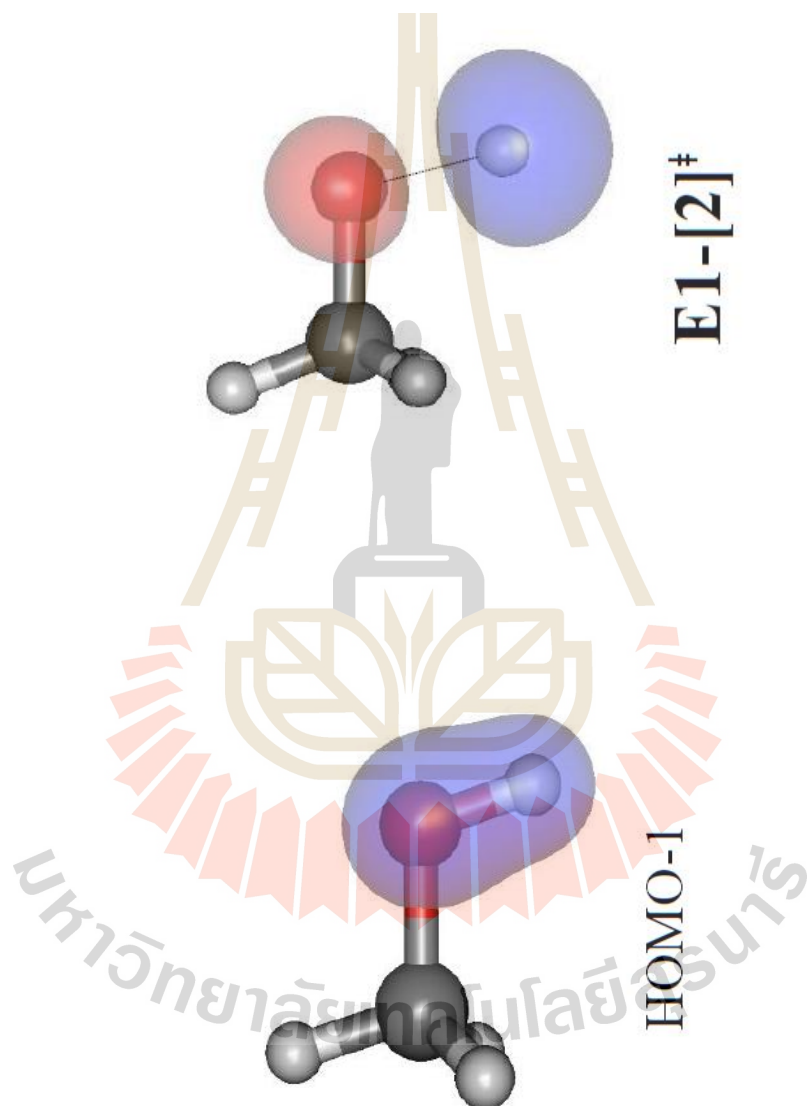


FIG. 6. Mechanisms of the unimolecular photodissociations of CH_3OH obtained from the analysis of the S_0 and S_1 potential energy curves. Energies are in kJ/mol and the relative energies are with respect to structure G1-[1]. ΔG^{\ddagger} = relative Gibbs free energy at 1200 K, ΔH^{\ddagger} = reaction enthalpy, ΔG^\ddagger = relative Gibbs free energy for formation of transition structure at 1200 K, ΔH^\ddagger = enthalpy of activation; $k^{\text{C}^{\ddagger\delta}}$ = rate constant with quantized vibrations at 1200 K; ‡ = transition structure and δ = structure at the intersection of the S_0 and S_1 potential energy curves. a) Channels (1)-(3). b) Channel (4). c) Channel (5).





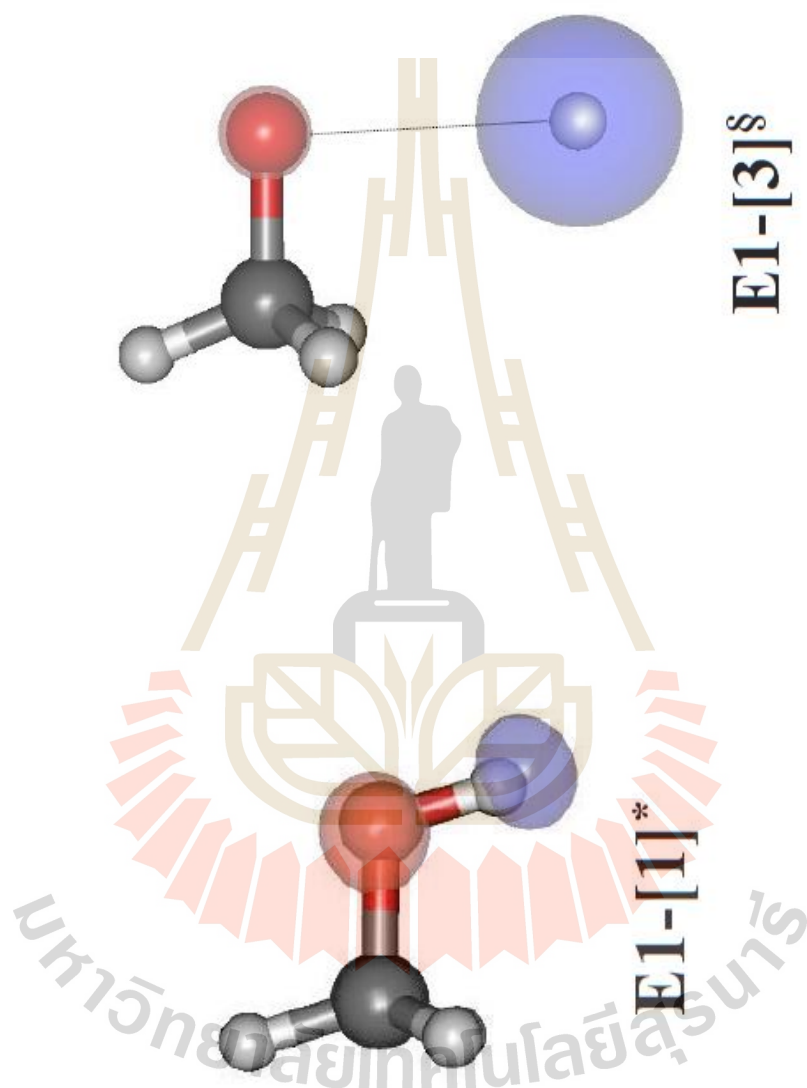


Table S1(a) Characteristic structures, structure parameters and energetics of CHOH, observed on the potential energy curves obtained from CASPT2(4,7) calculations.

| Structure | E_{rel} | C-H | | Regions | $\Delta H_{\text{C}_1\text{O}_2}$ | $\Delta H_{\text{C}_1\text{O}_3}$ | $\Delta H_{\text{C}_1\text{O}_4}$ | $\Delta H_{\text{C}_1\text{O}_5}$ | $\Delta H_{\text{C}_1\text{O}_6}$ | $\Delta H_{\text{C}_1\text{O}_7}$ | $\Delta H_{\text{C}_1\text{O}_8}$ |
|-----------|---|----------------|----------------|----------------|-----------------------------------|-----------------------------------|-----------------------------------|-----------------------------------|-----------------------------------|-----------------------------------|-----------------------------------|
| | | Regions | Regions | | | | | | | | |
| | | | | | | | | | | | |
| | 0.477 (-115.16845) [0.2382] (6.48) | 1.10 [1.10] | 1.10 [1.10] | 1.43 [1.44] | 0.97 [0.97] | 112 [112] | 107 [107] | 108 [108] | 108 [108] | 108 [108] | 108 [108] |
| | | | | | | | | | | | |
| | -115.19865 (6.46) | 1.10 | 1.10 | 1.42 | 0.97 | 105 | 108 | 106 | 116 | 108 | 108 |
| | | | | | | | | | | | |
| | -115.2061868 (6.67) | 1.10 | 1.10 | 1.39 | 1.40* | 107 | 113 | 106 | 112 | 105 | 105 |
| | | | | | | | | | | | |
| | -115.3472186 (0.02) | 1.10 | 1.10 | 1.39 | 2.60 | 108 | 114 | 106 | 110 | 93 | 93 |
| | | | | | | | | | | | |
| | -115.3471961 (0.01) | 1.10 | 1.10 | 1.39 | 2.60 | 108 | 113 | 106 | 110 | 97 | 97 |

Supplementary Material

Mechanisms of the photodissociations of single-isolated methanol

Pannipa Panjapo, Kittipan Siwawannapong, and Kritsana Sagarik*

School of Chemistry, Institute of Science, Suranaree University of Technology, Nakhon

Ratchasima 30000, Thailand

E-mail: kritsana@sut.ac.th

Table S1(a) (Cont.)

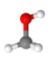
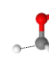
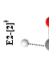
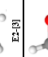
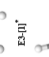
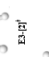
| E ^{Te} | E ^{Es} | | C-H | | Repos | Repos | $\Delta H_{\text{C}}(\text{O})$ | $\Delta H_{\text{C}}(\text{O})$ | $\Delta H_{\text{C}}(\text{O})$ | $\Delta H_{\text{C}}(\text{O})$ | $\Delta H_{\text{C}}(\text{O})$ | $\Delta H_{\text{C}}(\text{O})$ | $\Delta H_{\text{C}}(\text{O})$ | $\Delta H_{\text{C}}(\text{O})$ | $\Delta H_{\text{C}}(\text{O})$ | $\Delta H_{\text{C}}(\text{O})$ | |
|---|-----------------|------------------|-------|-------------------|-------------------|-------|---------------------------------|---------------------------------|---------------------------------|---------------------------------|---------------------------------|---------------------------------|---------------------------------|---------------------------------|---------------------------------|---------------------------------|-----|
| | Repos | Repos | Repos | Repos | | | | | | | | | | | | | |
|  E-101 ⁺ | -115.1749831 | 0.2352 (6.40) | 1.10 | 1.10 | 1.42 | 0.97 | 105 | 108 | 106 | 116 | 108 | 108 | 106 | 106 | 106 | 106 | 108 |
|  E-101 ⁺ | -115.119023 | 0.3465 (6.71) | 1.10 | 1.30 [*] | 1.44 | 0.97 | 105 | 102 | 111 | 116 | 105 | 108 | 105 | 105 | 105 | 105 | 108 |
|  E-101 ⁺ | -115.119147 | 0.2290 (6.25) | 1.10 | 1.70 | 1.44 | 0.97 | 99 | 87 | 99 | 130 | 106 | 106 | 99 | 80 | 111 | 122 | 111 |
|  E-101 ⁺ | -115.174954 | 0.2354 (6.41) | 1.10 | 1.10 | 1.42 | 0.97 | 105 | 108 | 106 | 116 | 108 | 108 | 105 | 105 | 110 | 116 | 123 |
|  E-101 ⁺ | -115.169220 | 0.2319 (6.31) | 1.10 | 1.10 | 1.60 [*] | 0.97 | 102 | 102 | 112 | 118 | 107 | 107 | 102 | 106 | 143 | 106 | 108 |
|  E-101 ⁺ | -115.230989 | 0.0495 (1.35) | 1.10 | 1.10 | 2.30 | 0.97 | 100 | 99 | 118 | 119 | 178 | 178 | 100 | 99 | 118 | 119 | 178 |

Table S1(a) (Cont.)



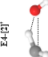

| E ^{Te} | E ^{Es} | | C-H | | Repos | Repos | $\Delta H_{\text{C}}(\text{O})$ | $\Delta H_{\text{C}}(\text{O})$ | $\Delta H_{\text{C}}(\text{O})$ | $\Delta H_{\text{C}}(\text{O})$ | $\Delta H_{\text{C}}(\text{O})$ | $\Delta H_{\text{C}}(\text{O})$ | $\Delta H_{\text{C}}(\text{O})$ | $\Delta H_{\text{C}}(\text{O})$ | $\Delta H_{\text{C}}(\text{O})$ | $\Delta H_{\text{C}}(\text{O})$ | |
|--|-----------------|------------------|-------|-------|-------------------|-------|---------------------------------|---------------------------------|---------------------------------|---------------------------------|---------------------------------|---------------------------------|---------------------------------|---------------------------------|---------------------------------|---------------------------------|-----|
| | Repos | Repos | Repos | Repos | | | | | | | | | | | | | |
|  E-101 ⁺ | -115.174730 | 0.2353 (6.40) | 1.10 | 1.08 | 1.44 | 0.97 | 105 | 106 | 106 | 106 | 106 | 106 | 106 | 106 | 106 | 106 | 108 |
|  E-101 ⁺ | -115.139615 | 0.2381 (6.48) | 1.10 | 1.05 | 1.40 [*] | 0.97 | 108 | 80 | 111 | 122 | 111 | 111 | 108 | 80 | 111 | 122 | 111 |
|  E-101 ⁺ | -115.239006 | 0.0317 (0.64) | 1.10 | 1.20 | 2.64 | 0.97 | 105 | 21 | 110 | 116 | 123 | 123 | 105 | 21 | 110 | 116 | 123 |
|  E-101 ⁺ | -115.243443 | 0.0101 (0.27) | 1.09 | 2.30 | 3.26 | 0.97 | 106 | - | 143 | 106 | 108 | 108 | 106 | - | 143 | 106 | 108 |

Table S1(c) Vibrational frequencies of CH₃OH in the S₀ state obtained from CASPT2(4,7) and CCSD(T) geometry optimizations with the aug-cc-pVDZ basis set compared with the experimental values.^{a)} The scaling factor for the CASPT(4,7) and CCSD(T) frequencies is 0.9434.^{b)} Vibrational frequencies are in cm⁻¹.

| | CASPT(4,7) | CCSD(T) | Exp. |
|----|------------|---------|------|
| 1 | 299 | 290 | 295 |
| 2 | 1013 | 976 | 1033 |
| 3 | 1040 | 1005 | 1060 |
| 4 | 1111 | 1094 | 1165 |
| 5 | 1307 | 1297 | 1345 |
| 6 | 1398 | 1377 | 1455 |
| 7 | 1416 | 1400 | 1477 |
| 8 | 1429 | 1411 | 1477 |
| 9 | 2872 | 2833 | 2844 |
| 10 | 2931 | 2891 | 2960 |
| 11 | 3000 | 2950 | 3000 |
| 12 | 3562 | 3600 | 3681 |

^{a)} W. J. Hehre, L. Radom, P. Schleyer, and J. A. Pople, *Ab Initio Molecular Orbital Theory* (Wiley, New York (1986).
^{b)} A. P. Scott and L. Radom, *J. Phys. Chem.*, 1996, **100**, 16502–16513.

| E ^{Ter} | E ^{Ex} | C-H | | R _{OH} (°) | R _{CO} (°) | R _{COH} (°) | ∠H ₁ C ₁ O ₁ | ∠H ₂ C ₁ O ₁ | ∠H ₁ C ₁ H ₂ | ∠H ₂ C ₁ H ₃ | ∠H ₁ O ₁ C ₁ | ∠H ₂ O ₁ C ₁ |
|------------------|------------------|-------------------|-------------------|---------------------|---------------------|----------------------|---|---|---|---|---|---|
| | | Re _{opt} | Re _{exp} | | | | | | | | | |
| -115.242725 | 0.0024 (0.06) | 1.10 | 1.11 | 1.39 | 3.26 | 108 | 108 | 107 | 110 | 110 | 52 | 52 |
| 115.227004 | 0.6557 (1.52) | 1.10 | 1.31 | 1.37 | 2.93 | 111 | 111 | 111 | 111 | 112 | 46 | 46 |
| 115.244544 | 0.0964 (2.62) | 1.10 | 2.93 | 1.35 | 114 | 114 | 114 | 120 | 120 | 120 | | |

Distances, angles and energies (E^{Ter} and E^{Ex}) are in Å, degree and au, respectively; [..] = values obtained from CASPT2(4,12) calculations; (..) = E^{Ex} in eV. Structures G1-[I] is the fully optimized structure in the S₀ state.

Table S1(b) Structural parameters of CH₃OH in the electronic ground state obtained from CASPT2(4,7), CASPT2(14,12) and CCSD(T) geometry optimizations with the aug-cc-pVDZ basis set compared with the values obtained from microwave and millimeter wave spectrum in Ref. [38]. Distances in Å and angles in degree.

| | CASPT2(4,7) | CASPT2(14,12) | CCSD(T) | Exp. |
|-----------------------|-------------|---------------|---------|------|
| R _{C(O)H(2)} | 1.10 | 1.10 | 1.11 | 1.09 |
| R _{C(O)H(4)} | 1.10 | 1.10 | 1.11 | - |
| R _{C(O)O(5)} | 1.42 | 1.44 | 1.44 | 1.42 |
| R _{O(6)H(6)} | 0.97 | 0.97 | 0.97 | 0.95 |
| ∠H(2)C(O)O(5) | 112.3 | 111.8 | 111.8 | - |
| ∠H(4)C(O)O(5) | 106.8 | 106.6 | 106.5 | - |
| ∠H(2)C(O)H(3) | 108.7 | 109.1 | 109.2 | 108 |
| ∠H(2)C(O)H(4) | 108.3 | 108.7 | 108.7 | - |
| ∠H(6)O(5)C(O) | 108.0 | 107.4 | 107.7 | 108 |

Table S2 Characteristic structures of CH₃OH on the S₀ and S₁ potential energy curves for the C-O dissociation. The electronic configurations and CI coefficients were obtained from CASPT2(4,7) calculations in the S₀ and S₁ states. The values of the LUMO isosurfaces are 0.11.

| Structure | S ₁ | | S ₀ | | |
|----------------------------------|---------------------------|-----------|---------------------|---------------------------|--------|
| | Conf. | CI Coeff. | Structure | Conf. | |
| E ₃ -[1] ⁺ | Ψ_9^{10} | 0.9849 | G3-[1] ⁺ | Ψ_6 | 0.9830 |
| | $\Psi_{5,9}^{10,12}$ | 0.0902 | | Ψ_7^{12} | 0.0724 |
| | $\Psi_{9,8}^{10,10}$ | 0.0686 | | $\Psi_{8,8}^{11,11}$ | 0.0699 |
| E ₃ -[2] ⁺ | Ψ_9^{10} | 0.9803 | G3-[2] ⁺ | Ψ_6 | 0.9781 |
| | $\Psi_{8,8}^{10,11,11}$ | 0.1064 | | Ψ_8^{11} | 0.0865 |
| | $\Psi_{9,9}^{10,12}$ | 0.0937 | | Ψ_7^{12} | 0.0763 |
| E ₃ -[3] [±] | Ψ_8^{10} | 0.9877 | G3-[3] [±] | Ψ_9^{10} | 0.9929 |
| | Ψ_6 | 0.0916 | | $\Psi_{8,8}^{10,11,11}$ | 0.0661 |
| | $\Psi_{8,8,9}^{10,11,12}$ | 0.0657 | | $\Psi_{8,8,9}^{10,11,12}$ | 0.0502 |

Ψ_6 = electronic ground state; Ψ_8 = α - γ singly excited state (S-type); $\Psi_{8,8}^{10,11,11}$ = α - γ doubly excited state (D-type); the indices a and b, and r and s label occupied and virtual or unoccupied spin orbitals, respectively; a bar or lack of a bar is to denote beta (β) and alpha (α) spin orbitals, respectively.

Table S4 Characteristic structures of CH₃OH on the S₀ and S₁ potential energy curves for the intramolecular [CH₂OH]→[CH₂OH] isomerization. The main electronic configurations and CI coefficients were obtained from CASPT2(4,7) calculations in the S₀ and S₁ states.


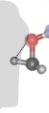

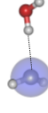
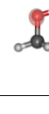
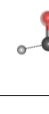

| Structure | S ₁ | | S ₀ | |
|---------------------------|---|----------------------------|---|----------------------------|
| | Conf. | CI Coeff. | Conf. | CI Coeff. |
| E4-[1]⁺ |  Ψ ₉ ¹⁰ Ψ _{9,9} ^{10,11} Ψ _{9,8,8} ^{10,11,11} | 0.9850 0.0898 0.0716 | Ψ ₀ Ψ ₉ ¹⁰ | 0.9830 0.0721 |
| E4-[2]⁺ |  Ψ ₉ ¹⁰ Ψ _{9,8} ^{10,11} Ψ _{9,8,8} ^{10,11,12} | 0.9858 0.1220 0.0878 | Ψ ₀ Ψ ₉ ¹⁰ Ψ _{9,8,8} ^{10,11,12} | 0.9859 0.0936 0.0878 |
| E4-[3] |  Ψ ₉ ¹⁰ Ψ _{9,8} ^{10,11} Ψ _{9,8,8} ^{10,11,12} | 0.9494 0.2928 0.0583 | Ψ ₀ Ψ _{9,8} ^{10,11} Ψ _{9,8,8} ^{10,11,12} | 0.6630 0.6473 0.3564 |
| E4-[4] |  Ψ ₉ ¹⁰ Ψ _{9,8,8} ^{10,11} | 0.9902 0.1007 | Ψ ₀ Ψ _{9,8,8} ^{10,11} | 0.9452 0.2912 0.0962 |

Table S3 Characteristic structures of CH₃OH on the S₀ and S₁ potential energy curves for the C-H dissociation. The electronic configurations and CI coefficients were obtained from CASPT2(4,7) calculations in the S₀ and S₁ states. The values of the LUMO isosurfaces are 0.11.

| Structure | S ₁ | | S ₀ | |
|---------------------------|--|----------------------------|---|----------------------------|
| | Conf. | CI Coeff. | Conf. | CI Coeff. |
| E2-[1]⁺ |  Ψ ₉ ¹⁰ Ψ _{9,9} ^{10,11} Ψ _{9,8,8} ^{10,11,11} | 0.9850 0.0899 0.0715 | Ψ ₀ Ψ ₉ ¹⁰ | 0.9830 0.0722 |
| E2-[2]⁺ |  Ψ ₉ ¹⁰ Ψ _{9,8} ^{10,11} Ψ _{9,8,8} ^{10,11,12} | 0.9758 0.1691 0.1196 | Ψ ₀ Ψ _{9,8} ^{10,11} Ψ _{9,8,8} ^{10,11,12} | 0.9753 0.1682 0.0917 |
| E2-[3] |  Ψ ₉ ¹⁰ Ψ _{9,9} ^{10,11} Ψ _{9,8,8} ^{10,11,11} | 0.9669 0.1160 0.0936 | Ψ ₀ Ψ _{9,8,8} ^{10,11} Ψ _{9,8,8} ^{10,11,11} | 0.9553 0.1919 0.1445 |

Ψ₀ = electronic ground state; Ψ_a^b = a→b singly excited state (S-type); Ψ_{a₁a₂}^{b₁b₂ = a→b and b→a doubly excited state (D-type); the indices a and b, and r and s label occupied and virtual or unoccupied spin orbitals, respectively; a bar or slash of a bar is to denote beta (β) and alpha (α) spin orbitals, respectively.}

Table S5 Characteristic structures of CH₃OH on the S₁ relax-scan potential energy curve for the elimination of H₂. The electronic configurations and CI coefficients were obtained from CASPT2(4,7) calculations in the S₀ and S₁ states. The values of the LUMO isosurfaces are 0.11.

| Structure | S ₁ | | S ₀ | | | |
|----------------|----------------|----------------------|----------------|----------------|----------------------|-----------|
| | Structure | Conf. | CI Coeff. | Structure | Conf. | CI Coeff. |
| E5-[1] | | Ψ_9^{T0} | 0.9712 | G5-[1]' | Ψ_8^{T0} | 0.8594 |
| | | $\Psi_{9,8}^{T0,10}$ | 0.1944 | | Ψ_6^{T0} | 0.4157 |
| E5-[2]' | | Ψ_6^{T0} | 0.0756 | G5-[2] | $\Psi_{8,8}^{T0,10}$ | 0.2635 |
| | | Ψ_9^{T0} | 0.9457 | | Ψ_6^{T0} | 0.8963 |
| | | $\Psi_{9,8}^{T0,10}$ | 0.3039 | | Ψ_8^{T0} | 0.3227 |
| E5-[3] | | $\Psi_{9,8}^{T0,12}$ | 0.0523 | G5-[3] | $\Psi_{8,8}^{T0,10}$ | 0.2726 |
| | | Ψ_9^{T0} | 0.9569 | | Ψ_0^{T0} | 0.9298 |
| | | $\Psi_{9,8}^{T0,10}$ | 0.2675 | | Ψ_8^{T0} | 0.2551 |
| | | $\Psi_{9,8}^{T0,12}$ | 0.0472 | | $\Psi_{8,8}^{T0,10}$ | 0.2285 |

Ψ_0 = electronic ground state; Ψ_6^i = a→r singly excited state (S-type); Ψ_8^i = a→r and b→s doubly excited state (D-type); the indices a and b, and r and s label occupied and virtual or unoccupied spin orbitals, respectively, a bar or lack of a bar is to denote beta (β) and alpha (α) spin orbitals, respectively.

| Structure | T ₁ | | T ₀ | | |
|---------------------------|----------------|-----------|---------------------------|---------------|-----------|
| | Conf. | CI Coeff. | Structure | Conf. | CI Coeff. |
| ³E4-[5] | Ψ_8^{T0} | 0.9992 | ³G4-[5] | Ψ_9^{T0} | 0.9992 |
| | Ψ_9^{T0} | 0.0399 | | Ψ_8^{T0} | 0.0399 |

Ψ_0 = electronic ground state; Ψ_8^i = a→r singly excited state (S-type); Ψ_9^i = a→r and b→s doubly excited state (D-type); the indices a and b, and r and s label occupied and virtual or unoccupied spin orbitals, respectively, a bar or lack of a bar is to denote beta (β) and alpha (α) spin orbitals, respectively.

Table S6 Rate constants (k), enthalpies of activation (ΔH^\ddagger) and relative Gibbs free energies for formations of transition structures (ΔG^\ddagger) in the direct covalent bond dissociations in the S_0 state, obtained based on transition state theory and the potential energy curves. Energies, rate constants and temperatures are in kJ mol^{-1} , s^{-1} and K, respectively.

| | ΔE^\ddagger | ΔH^\ddagger | T_c | T | k^{Class} | k^{Qsb} | k^{Eckart} | ΔG^\ddagger |
|--------------------------------------|---------------------|---------------------|-------|------|------------------------|------------------------|------------------------|---------------------|
| $G1-[1] \rightarrow G1-[2]^\ddagger$ | 199 | 184 | 271 | 308 | 4.25×10^{-21} | 5.27×10^{-19} | 3.16×10^{-18} | 183 |
| | | | | 585 | 4.19×10^{-5} | 3.26×10^{-4} | 4.79×10^{-4} | 185 |
| | | | | 1200 | 5.78×10^4 | 1.11×10^5 | 1.21×10^5 | 192 |
| $G1-[1] \rightarrow G3-[2]^\ddagger$ | 42 | 45 | 11 | 308 | 8.48×10^4 | 2.70×10^5 | 2.70×10^5 | 44 |
| | | | | 585 | 8.04×10^6 | 1.17×10^7 | 1.17×10^7 | 45 |
| | | | | 1200 | 1.51×10^{11} | 1.65×10^{11} | 1.65×10^{11} | 50 |
| $G1-[1] \rightarrow G2-[2]^\ddagger$ | 135 | 142 | 33 | 308 | 9.83×10^{-14} | 1.08×10^{-11} | 1.10×10^{-11} | 140 |
| | | | | 585 | 4.48×10^{-1} | 2.86×10^0 | 2.88×10^0 | 141 |
| | | | | 1200 | 7.67×10^6 | 1.32×10^7 | 1.32×10^7 | 144 |

ΔE^\ddagger = energy barrier with respect to structure $G1-[1]$; T_c = crossover temperature; k^{Class} = transition structure, k^{Qsb} = rate constant obtained from classical transition state theory (TST); k^{Eckart} = rate constant obtained with quantized vibrations including the zero-point vibrational energy; k^{Eckart} = rate constant obtained with the Eckart correction of quantum mechanical tunneling; ΔH^\ddagger and ΔG^\ddagger = enthalpy of activation and relative Gibbs free energy for formation of transition structure with respect to structure $G1-[1]$; k

Table S7 Reaction enthalpies (ΔH^{rel}) and relative Gibbs free energies (ΔG^{rel}) for direct covalent bond dissociations in the S_1 state, obtained based on the transition state theory and barrierless potential energy curves ($\Delta E^\ddagger = 0 \text{ kJ mol}^{-1}$). Energies and temperatures are in kJ mol^{-1} and K, respectively.

| | ΔE^{rel} | ΔH^{rel} | T | ΔG^{rel} |
|---|-------------------------|-------------------------|------|-------------------------|
| $E1-[1]^\ddagger \rightarrow E1-[3]^\ddagger$ | -189 | -189 | 308 | -217 |
| | | | 585 | -241 |
| | | | 1200 | -298 |
| $E3-[2]^\ddagger \rightarrow E3-[3]^\ddagger$ | -227 | -165 | 308 | -168 |
| | | | 585 | -169 |
| | | | 1200 | -173 |

ΔE^{rel} = relative energy with respect to the vertically excited structure; ‡ = vertically excited structure; \ddagger = structure at the intersection of the S_0 and S_1 potential energy curves; ΔH^{rel} and ΔG^{rel} = reaction enthalpy and relative Gibbs free energy with respect to the dissociating structure.

Table S9 Rate constants (k), enthalpies (ΔH) and relative Gibbs free energies (ΔG) for unimolecular isomerization dissociations, obtained based on the transition state theory and potential energy curves. Energies, rate constants and temperatures are in kJ mol^{-1} , s^{-1} and K, respectively.

| | ΔE^{\ddagger} | ΔH^{\ddagger} | $\Delta E^{\ddagger, \text{rel}}$ | $\Delta H^{\ddagger, \text{rel}}$ | T_c | T | k^{Class} | $k^{\text{Q-ub}}$ | k^{Eckart} | ΔG^{\ddagger} | ΔG^{rel} |
|------------------------------------|-----------------------|-----------------------|-----------------------------------|-----------------------------------|-------|------|--------------------|--------------------|---------------------|-----------------------|-------------------------|
| E4-[D]¹ → E4-[4] | | | | | | 308 | | | | | -317 |
| | | | | | | 585 | | Barrierless | | | -347 |
| | | | | | | 1200 | | | | | -422 |
| E1-[4][‡] → E5-[2] | | | | | | 308 | 4.98×10^1 | 4.46×10^4 | 5.32×10^4 | 48 | - |
| | | | | | | 585 | 7.77×10^5 | 1.36×10^7 | 1.43×10^7 | 67 | - |
| | | | | | | 1200 | 1.94×10^8 | 4.67×10^8 | 4.74×10^8 | 109 | - |

ΔE^{\ddagger} and $\Delta E^{\ddagger, \text{rel}}$ = relative energies on the potential energy curve; T_c = crossover temperature; ‡ = transition structure; \ddagger = structure at the intersection of the S_0 and S_1 potential energy curves; k^{Class} = rate constant obtained from classical transition-state theory (TST); $k^{\text{Q-ub}}$ = rate constant obtained with quantized vibrations including the zero-point vibrational energy; k^{Eckart} = rate constant obtained with the Eckart correction of quantum mechanical tunneling; ΔH^{\ddagger} and ΔG^{\ddagger} = enthalpy of activation and relative Gibbs free energy for formation of transition structure with respect to structure E1-[4][‡]; $\Delta H^{\ddagger, \text{rel}}$ and $\Delta G^{\ddagger, \text{rel}}$ = reaction enthalpy and relative Gibbs free energies with respect to structure E4-[2][‡].

Table S8 Rate constants (k), enthalpies (ΔH) and relative Gibbs free energies (ΔG) for unimolecular isomerization dissociations, obtained based on the transition state theory and potential energy curves. Energies, rate constants and temperatures are in kJ mol^{-1} , s^{-1} and K, respectively.

| | ΔE^{\ddagger} | ΔH^{\ddagger} | $\Delta E^{\ddagger, \text{rel}}$ | $\Delta H^{\ddagger, \text{rel}}$ | T_c | T | k^{Class} | $k^{\text{Q-ub}}$ | k^{Eckart} | ΔG^{\ddagger} | ΔG^{rel} |
|--|-----------------------|-----------------------|-----------------------------------|-----------------------------------|-------|------|-----------------------|-----------------------|-----------------------|-----------------------|-------------------------|
| G1-[D]¹ → G4-[2]¹ | | | | | | 308 | 2.31×10^{-5} | 9.73×10^{-6} | 1.33×10^{-5} | 105 | - |
| | | | | | | 585 | 4.54×10^3 | 3.03×10^3 | 3.30×10^3 | 107 | - |
| | | | | | | 1200 | 2.49×10^8 | 2.16×10^8 | 2.21×10^8 | 116 | - |
| G1-[4][‡] → G5-[3] | | | | | | 308 | | | | -362 | - |
| | | | | | | 585 | | Barrierless | | -401 | - |
| | | | | | | 1200 | | | | -493 | - |

ΔE^{\ddagger} and $\Delta E^{\ddagger, \text{rel}}$ = relative energies on the potential energy curve; T_c = crossover temperature; ‡ = transition structure; \ddagger = structure at the intersection of the S_0 and S_1 potential energy curves; k^{Class} = rate constant obtained from classical transition-state theory (TST); $k^{\text{Q-ub}}$ = rate constant obtained with quantized vibrations including the zero-point vibrational energy; k^{Eckart} = rate constant obtained with the Eckart correction of quantum mechanical tunneling; ΔH^{\ddagger} and ΔG^{\ddagger} = enthalpy of activation and relative Gibbs free energy for formation of transition structure with respect to structure G1-[D]¹; $\Delta H^{\ddagger, \text{rel}}$ and $\Delta G^{\ddagger, \text{rel}}$ = reaction enthalpy and relative Gibbs free energies with respect to structure G1-[4][‡].

Table S10 Vertical excitation energies (E^{Ex}) and corresponding oscillator strengths normalized with respect to structure **G2-[2][†]**.

| Structure | E^{Ex} (eV) | Oscillator strength |
|---------------------------|-------------------------|---------------------|
| G1-[1][*] | 6.58 | 0.35 |
| G3-[2][†] | 6.31 | 0.51 |
| G2-[2][†] | 6.71 | 1.00 |

CURRICULUM VITAE

Ms. PANNIPA PANAJAPO

Date of Birth: January, 7, 1988

Place of Birth: Nakhon Ratchasima Province

Education Background:

2009-2012 B. Sc. (Natural Products Chemistry), Université du Québec à Chicoutimi, Canada.

2012-Present Ph.D. Student in Chemistry, Suranaree University of Technology, Thailand

Grant and Fellowship:

2007 - 2012 One Scholarship One District Project, Thailand

2010 – 2010 Professeurs de chimie fellowship, Université du Québec à Chicoutimi, Canada

2012 - 2017 Royal Golden Jubilee (RGJ) Ph. D. research scholarship from Thailand Research Fund (TRF)